UNIVERSITY OF
BIRMINGHAM

MICRO AND NANO SCALE THREE-DIMENSIONAL RECONSTRUCTION OF POLYMER ELECTROLYTE FUEL CELL POROUS LAYERS

By

Hossein Ostadi Valiabad

A thesis submitted to
The University of Birmingham
for the degree of

DOCTOR OF PHILOSOPHY

School of Mechanical Engineering
College of Engineering and Physical Sciences
The University of Birmingham
November 2011

ABSTRACT

This presented PhD project is a step change towards the fluid flow prediction within the polymer electrolyte fuel cells through micro/nano characterisation of porous layers of the fuel cell. X-ray micro/nano tomography has been developed to reveal a three dimensional digital image of gas diffusion layers at micro/nano scale and focused ion beam/scanning electron microscope nanotomography technique was developed to visualize the three dimensional porous structure of the microporous layer and catalyst layer. Tomography images then were used to obtain morphological parameters of the layers and combined with well-known analytical models and numerical simulations to anticipate the permeability, diffusivity and tortuousity of the layers. The project can be divided into two main sections. In the first section X-ray micro and nanotomography were used to characterise the uncompressed gas diffusion layers. It was found that a critical step in the tomography image characterisation is thresholding and a novel experimental approach to tune the threshold was proposed. In addition, the structural features of compressed gas diffusion layers were captured by using polydimethylsiloxane to encapsulate the compressed porous structure and by subsequently employing X-ray microtomography to reconstruct a digital three dimensional model. In the second section, focused ion beam/scanning electron microscope nanotomography was developed for the microporous layer and the catalyst layer. To characterise the focused ion beam milling yield of the porous materials, a scanning electron microscopy stereo imaging technique was employed. The nanotomography and the stereo imaging techniques were successfully applied to other materials such as glass micropipettes, various metals, silicon, urine catheters and diatomaceous frustules. The single phase single component Lattice Boltzmann numerical

modelling was combined with different tomography images to predict the permeability, diffusivity and tortuousity of the porous layers and the results were compared to the experiments. Finite element analysis was used to reveal the through plane stream line tortuousity of the catalyst layer.

Dedicated to my parents

ACKNOWLEDGEMENTS

First of all, I would like to express my sincere appreciation to my research supervisor, Professor Kyle Jiang, for his guidance, ideas and support during my PhD study. I would like to acknowledge the research funding body UK Technology Strategy Board (TSB Project No. TP/6/S/K3032H) and industrial and academic partners AVL List GmbH, Intelligent Energy Ltd., Johnson Matthey Fuel Cells Ltd., Saati Group Inc., Technical Fibre Products Ltd, Loughborough University and the University of Liverpool. I should also thank Dr. Pratap Rama from Intelligent Energy Ltd. for his great help. I would also like to thank members of the Microengineering and Nanotechnology group, for being supportive and kind and my colleagues Majid, Sam, Sean, Jason, Ali, Andy, Sahand, Mohammed and Hanny for sharing their knowledge and expertise and for their helpful suggestions and support throughout the completion of this work. Finally, I would like to thank my parents Shamsolzaman and Zabihollah for their support throughout my graduate study journey. They have always been there as a sounding board during my difficult times.

TABLE OF CONTENTS

LIST OF FIGURES

LIST OF TABLES

ABBREVIATIONS

3D	Three dimensional
µCT	Micro computed tomography
Avg.	Average
BET	Brunauer-Emmett-Teller
BPP	Bipolar plate
CCM	Catalyst coated membrane
CFD	Computational fluid dynamics
CL	Catalyst layer
DC	Direct current
DLA	Diffusion-limited aggregation
FEA	Finite element analysis
FEP	Fluorinated ethylene propylene
FIB	Focused ion beam
GDL	Gas diffusion layer
LB	Lattice Boltzmann
MEA	Membrane electrode assembly
MIL	Mean intercept length
MPL	Microporous layer
nCT	Nano computed tomography
PDMS	polydimethylsiloxane
PEFC	Polymer electrolyte fuel cell
PSD	Pore size distribution
PTFE	Polytetrafluoroethylene

SEM	Scanning electron microscope
TEM	Transmission electron microscopy

NOMENCLATURES

a	Sample cross sectional area through which flow passes
A	Constant
c	Gas concentration
c_T	The total concentration or molar density of all of the gas species
d_f	Fibre diameter
D_0	Free diffusion coefficient
D_{ij}	Effective binary interaction parameter between species *i* and *j*
D_{eff}	Local effective diffusivity
$D_{eff,k}$	Effective diffusion coefficient
D_p	Pore diameter
$D_{p,avg}$	Average pore diameter
$f_i(x,t)$	Particle distribution function
$f_i^{eq}(x,t)$	The equilibrium distribution function
$I(x,y)$	(x,y) Pixel intensity
J	Diffusive gas flux
$J_{i,n}$	Diffusive flux in the *i* direction at voxel *n*
k_G	Gas phase permeability
k_{hp}	Effective hydraulic permeability
k_K	Kozeny constant
k_r	Relative permeability
k_{sat}	Saturated permeability
K_{TS}	Tomadakis-Sotirchos effective diffusivity factor
l	Sample thickness

Li	Overall sample length in the direction i
M_m	Molar mass
M_{ij}	Image moment of order $i+j$
M_{ion}	Ion molecular weight
M_{target}	Target molecular weight
m_i	Mole fraction of species i
N_A	Avogadro constant
N_i, N_j	Flux density of species i and j (mol/cm^{2}s)
N_L	Superficial flux density
N_{tot}	Total number of the void voxels in the image
P_C	Capillary pressure
P_{diff}	Gas differential pressure
P_G	Gas phase pressure
P_L	Liquid phase pressure
q_i	Average velocity in the direction i
R	Gas constant
r_C	Capillary pore radius
$r_{p,mean}$	Mean pore radius
s	Saturation
S_n	Reduced nuclear cross section
S_s	Specific surface area
T	Temperature in Kelvin
U_s	Surface potential
v_G	Superficial velocity of phase gas
V_G	Volumetric flow rate
V_L	Molar volume of liquid
V_m	Single molecular layer volume of gas

V_M	Molar volume of gas
V_{PT}	Total pore volume

Greek letters

α	Fitted value
δt	Time step
ε_B	Bulk porosity
ε_G	Gas phase bulk porosity
ε_p	Percolation threshold porosity
γ	Surface tension
τ_i	Tortuousity along the direction *i*
τ_G	Tortuousity of the gas phase
τ_r	Dimensionless relaxation time parameter
λ	Relational parameter controls the rate at which $f_i(x,t)$ approaches $f_i^{eq}(x,t)$
μ	Viscosity
μ_G	Gas phase viscosity
Ω	Steady state test parameter
θ	Contact angle
ρ	Density of air
$\sigma_{molecule}$	Surface of an adsorbed molecule
ξ_i	Velocity of a moving particle in direction i

LIST OF PUBLICATIONS DURING PHD STUDIES

Journal papers:

[1] H. Ostadi, P. Rama, Y. Liu, R. Chen, X. X. Zhang, K. Jiang, 3D reconstruction of a gas diffusion layer and a microporous layer, Journal of Membrane Science, 351(1), 69-74, 2010.

[2] H. Ostadi, P. Rama, Y. Liu, R. Chen, X. X. Zhang, K. Jiang, The influence of threshold variation on determining the properties of a gas diffusion layer in X-ray nanotomography, Chemical Engineering Science, 65(6), 2213-2217, 2010.

[3] H. Ostadi, P. Rama, Y. Liu, R. Chen, X. Zhang, K. Jiang, Threshold fine-tuning and 3D characterisation of porous media using X-ray nanotomography, Current Nanosciences, 6(2), 226-231, 2010.

[4] H. Ostadi, P. Rama, Y. Liu, R. Chen, X. Zhang, K. Jiang, Nanotomography based study of gas diffusion layers, Microelectronic Engineering, 87 (5-8), 1640-1642, 2010.

[5] H. Ostadi, K. Jiang, D. W. L. Hukins, A comparison of surface roughness analysis methods applied to urinary catheters, Precision Engineering, 34 (4), 798-801, 2010.

[6] H. Ostadi, K. Jiang, P. D. Prewett, Characterization of FIB milling yield of metals by SEM stereo imaging technique, Microelectronic Engineering, No86, pp. 1021-1024, 2009.

[7] H. Ostadi, M. Malboubi, K. Jiang, P.D. Prewett, 3D reconstruction of a micro pipette tip, Microelectronic Engineering, N86,868-870, 2009.

[8] H. Ostadi, K. Jiang, P. D. Prewett, Micro/Nano X-ray tomography reconstruction fine-tuning using scanning electron microscope images, Micro & Nano Letters, V3, No.4, pp.106-109,2008.

[9] P. Rama, Y. Liu, R. Chen, H. Ostadi, K. Jiang, Gao Y, X. X. Zhang, Determination of anisotropic permeability of a carbon cloth GDL, International journal for numerical methods in fluids (In press).

[10] P. Rama, Y. Liu, R. Chen, H. Ostadi, K. Jiang, Gao Y, XX. Zhang, R. Fisher, M. Jeschke, Simulation of liquid water breakthrough in a nano-tomography reconstruction of a carbon paper gas diffusion layer, AIChE Journal (In press).

[11] P. Rama, Y. Liu, R. Chen, H. Ostadi, K. Jiang, Gao Y, XX. Zhang, D. Bivio, P. Grassini, A numerical study of structural change and anisotropic permeability in

compressed carbon cloth polymer electrolyte fuel cell gas diffusion layers, Fuel Cells, 11, 274-285, 2011.

[12] P. Rama, Y. Liu, R. Chen, H. Ostadi, K. Jiang, X. X. Zhang, Multi-Scale Modelling of Single-Phase Multi-Component Transport in the Cathode Gas Diffusion Layer of a Polymer Electrolyte Fuel Cell, ACS Energy & Fuels 24, 3130-3143, 2010.

[13] P. Rama, Y. Liu, R. Chen, H. Ostadi, K. Jiang, X. Zhang, R. Fisher, M. Jeschke, An X-ray tomography based Lattice Boltzmann simulation study on gas diffusion layers of polymer electrolyte fuel cells, ASME journal of fuel cell science and technology, 7(3), 031015, 1-12, 2010.

[14] X. Chen, H. Ostadi, K. Jiang, 3D surface reconstruction of diatomaceous frustules, Analytical biochemistry, 403(1-2), 63-66, 2010.

[15] M. Malboubi, H. Ostadi, S. Wang, Y. Gu, K. Jiang, Effects of pipette tip roughness on Giga-seal formation (Best paper award, IAENG, 2009 London) Engineering letters, 17(4), 2009.

[16] M. Imbaby, H. Ostadi, K. Jiang, Characterisation of stainless steel micro parts fabricated by soft moulding technique, Micro & Nano Letters, 4(2), 99-105, 2009.

[17] N. H. Saad, X. Wei, C. Anthony, H. Ostadi, R. Al-Dadah, M. C. L. Ward, Impact of manufacturing variation on the performance of coupled micro resonator array for mass detection sensor, Procedia Chemistry, 2009.

Conference papers:

[18] H. Ostadi, P. Rama, Y. Liu, R. Chen, K. Jiang, X. Zhang, Micro/Nano tomography for analysis of gas diffusion layers of microfuel cells, Power MEMS 2009 Workshop, Washington DC, USA, 1-4 Dec. 2009.

[19] H. Ostadi, P. Rama, Y. Liu, R. Chen, X. Zhang, K. Jiang, Nanoscale porosity characterisation using X-ray nanotomography, MNE Conference 2009,Ghent, Belgium.

[20] H. Ostadi, K. Jiang, D. W. L. Hukins, Surface characterisation of urinary catheters, MNE Conference, 2009, Ghent, Belgium.

[21] H. Ostadi, K. Jiang, P D Prewett, Characterization of FIB milling yield of metals by SEM stereo imaging technique, Micro and Nano Engineering Conference 2008

[22] H. Ostadi, K. Jiang, P. D. Prewett, Micro/Nano X-Ray Tomography Reconstruction Tuning Using SEM Images for PEMFC Gas Diffusion Layers, 8th IEEE Conference on Nanotechology, 18-21 Aug. 2008 428 - 431, Arlington, USA.

[23] H. Ostadi, K. Jiang, P. D. Prewett, Characterization of FIB milling yield of metals by SEM stereo imaging technique, Micro and Nano Engineering Conference 2008

[24] H. Ostadi, M. Malboubi, K. Jiang, P. D. Prewett, FIB/SEM nano-tomography of a micro pipette, Micro and Nano Engineering Conference 2008, Copenhagen, Denmark.

[25] Hassanin H., Ostadi H., Jiang K., Surface and geometry characterisation of soft lithography thick moulds for net shape ceramic manufacturing, Micro Nano Engineering Conference MNE10, Genova, Italy, 2010 (Poster presentation)

[26] P. Rama, Y. Liu, R. Chen, H. Ostadi, K. Jiang, X. X. Zhang, Multiscale simulation of transport in the polymer electrolyte fuel cell, ECS 217th Meeting, Characterisation of porous materials, poster presentation (2010).

1 CHAPTER 1: INTRODUCTION

1.1 INTRODUCTION

This PhD project was to set out to develop X-ray micro/nano computed tomography (X-ray μCT and nCT), focused ion beam/scanning electron microscopy (FIB/SEM) nanotomography and critical micro/nanostructural and fluid transportation characterisation of polymer electrolyte fuel cell (PEFC) porous layers towards the prediction of fluid flow within the fuel cell. The project was driven by the need to improve the fuel cell efficiency and fluid flow prediction within a cell as a part of the UK Technology Strategy Board project (TSB Project No. TP/6/S/K3032H). Academic and industrial partners including the University of Birmingham, Loughborough University, the University of Liverpool, Intelligent Energy Ltd. (UK), Johnson Matthey Fuel Cells Ltd. (UK), Technical Fibre Products Ltd. (UK) AVL List GmbH (Austria) and Saati Group Inc. (Italy) were involved in this project from August 2007 to May 2011. The role of the industrial partners was to provide improved woven and non-woven gas diffusion layer (GDL), microporous layer (MPL) and catalyst layer (CL) porous materials and to carry out various standard fuel cell electrical tests. While researchers at the universities were involved in modelling, fluid flow numerical simulations and characterisation of the developed fuel cells layers. In particular, 3D modelling and micro/nano characterisation of the porous layers were the main tasks undertaken at the University of Birmingham.

Existing models explaining the behaviour of GDL, MPL and CL layers in terms of fluid transportation and fuel cell performance at micro/nano scale are all commonly dependant on the use of key parameters such as porosity, mean pore radius, permeability, tortuousity

and effective diffusivity. These are all determined by the micro/nanostructural characteristics of the material. Such parameters cannot be rigorously determined without the real three dimensional (3D) structure. Furthermore, the sub-micron features of the MPL and CL require visualisation with sub-25 nm and sub-10 nm resolutions respectively. In addition, the soft nature of the layers poses many technical challenges. In order to reveal the internal structure of these layers 3D high resolution techniques are required.

The proposed approach used X-ray μCT and nCT to characterise the uncompressed and compressed GDL layers. In order to visualise the nanostructural features of the porous network of MPL and CL, FIB/SEM nanotomography was developed in this work. Both visualisation techniques have been combined with numerical simulations. Techniques have been successfully conducted for other applications including, glass micropipette, FIB milling yield of various materials, characterisation of urine catheters and diatomaceous frustules surface analysis.

1.2 AIMS AND OBJECTIVES

The aim of this PhD project is to improve PEFC efficiency through fluid flow prediction and characterisation of the fuel cell novel porous layers. The significance of this research is not limited to the layers 3D digital images, but also to calculate key morphological parameters and combine the digital models with analytical models, numerical lattice Boltzmann (LB) modelling and finite element analysis (FEA) to predict the fluid transportation phenomenon within the fuel cell. Woven and non-woven GDL materials with average fibre size of less than 10 μm are characterised through the X-ray μCT and nCT with pixel sizes of better than 2 μm and 970 nm respectively. MPL and CL with average agglomerate size of a few hundred nm are characterised using FIB/SEM nanotomography with a pixel size of higher than a few tens of nm.

The major challenges in the layers characterisation originate from the materials and image analysis and they fall into four main categories. First, binarisation of the grey scale images of the X-ray μCT and nCT images of the GDL are strongly influenced by the threshold value and subsequently obtained parameters are affected. Second, recognize a material which could be able to encapsulate the compressed GDL samples and fill the small pores during imaging with a distinct difference in density compared to the GDL. Third, very fine pores of the MPL and CL pose a technical challenge in taking ultra high resolution SEM images. Finally, the soft nature of the MPL and CL layers is compounded by difficulties associated with ultra thin layered slices when FIB milling is performed.

In order to achieve the research aims aforementioned, the project objectives are set out as follows:

- Develop X-ray μCT and nCT for the uncompressed GDL layers to obtain micro and nanostructural features.

- Find the influence of threshold variation on characterisation of the GDL layers and develop an experimental method to finely tune the threshold for X-ray μCT and nCT binarised images.

- Carry out experiments to compress GDL samples via polydimethylsiloxane (PDMS) and image the compressed GDL layers with X-ray μCT within various pressure conditions.

- Determine FIB milling yield of MPL and CL via the SEM stereo imaging technique.

- Develop the FIB/SEM nanotomography technique to reconstruct the 3D digital model of various MPL and CL and extend the technique to glass micropipette tip reconstruction.

- Prediction of permeability, toruousity and effective diffusivity of the layers via analytical approaches, Finite Element Analysis (FEA) and Lattice Boltzmann (LB) numerical simulation based on the models obtained from X-ray µCT, nCT and FIB/SEM nanotomography.

1.3 THESIS OUTLINE

This thesis consists of seven Chapters. Chapter 1 introduces the project research topic covered by this thesis. It includes the project aims, objectives and thesis outline.

Chapter 2 reviews the current models of the porous layers of the PEFC. It starts with the introduction of the main components of the PEFC, GDL, MPL and CL followed by the review of models, both analytical modelling and numerical simulations. Afterwards, a literature review of the current techniques for micro and nano characterisation of the PEFC porous layers is presented.

Chapter 3 introduces X-ray µCT/nCT images binarisation for characterisation of GDL. The imaging technique, back projection and resolution limits along with the structural parameters calculation including porosity, pore size distribution, characteristic lengths and structural tortuousity for fuel cell layers are explained. Also, the single-phase single-component lattice Boltzmann numerical modelling program developed by the University of Liverpool and Loughborough University is explained. Binarisation of X-ray µCT and nCT images, influence of threshold variation on determining the properties of GDL including porosity, average pore size, average fibre size, degree of anisotropy and permeability is investigated. A novel method to tune the threshold is discussed.

Chapter 4 then explains comprehensive characterisation of six woven and non-woven uncompressed GDL based on µCT and nCT images with 680 nm - 1.95 µm pixel sizes.

Then five woven samples are compressed under a range of compressions from 0.0 MPa to 100 MPa and encapsulated using PDMS material. X-ray μCT images are used to investigate the effect of compression on the porous GDL.

Chapter 5 presents a SEM stereo imaging method to quickly characterise the FIB milling yields of MPL and CL. The method is successfully extended to other applications such as FIB milling yield of metals, silicon, MPL & CL and surface characterisation of urinary catheters, diatomaceous frustules and micropipette tip.

Chapter 6 describes the application of FIB/SEM nanotomography on MPL, CL and other materials. It starts with a review of FIB/SEM nanotomography techniques applied to nanostructured materials followed by experimental details of imaging of both MPL and CL. Key structural features such as local porosity, pore size distribution, Knudsen diffusion coefficient and tortuousity are discussed. LB method was then subsequently applied to obtain permeability and tortuousity of the MPL and CL samples. FEA is developed to predict the 2D stream line tortuousity of the CL. Another application of the FIB/SEM nanotomography on the measurement of the roundness of micropipette tips is explained in detail.

Finally, in Chapter 7, the major findings from the study are summarised and possible future research trends are suggested.

2 CHAPTER 2: REVIEW OF PEFC MODELS AND TECHNOLOGY

2.1 INTRODUCTION

This Chapter presents a review of recent PEFC components, models, governing equations, parameters and the current characterisation techniques. PEFC porous layers are explained in Section 2.2. Existing fluid transport models including analytical and numerical models are discussed in Section 2.3. Common micro/nano characterisation PEFC porous layer techniques including air permeability test, mercury porosimetry, density measurement, Brunauer-Emmett-Teller surface analysis, 2D surface imaging through SEM/TEM and micro/nano tomography are reviewed in Section 2.4. Advantages and drawbacks of each method are reported. Finally, the literature review is summarised in Section 2.5.

2.2 PEFC AND ITS COMPONENTS

Owing to its zero-emission, high energy efficiency and low noise, PEFC is considered as a very promising alternative energy conversion device for a range of applications, most notably automotive and small stationary applications. A hydrogen PEFC directly converts the chemical energy of hydrogen into DC electrical energy. Hydrogen is forced to go through porous layers, to be in contact with the catalyst and become ionized at the anode, resulting in a production of electrons and protons. At the cathode side, water is produced through the reaction of oxygen with the protons and electrons [1],[2]. The chemical reactions in a PEFC can be described as follows:

at the anode:

$$H_2 \rightarrow 2H^+ + 2e^- \tag{2.1}$$

at the cathode:

$$\tfrac{1}{2}O_2 + 2H^+ + 2e^- \rightarrow H_2O \tag{2.2}$$

The anode and cathode of a modern single repeatable PEFC, as shown in Figure 2.1, are separated through a polymer proton-conductive membrane.

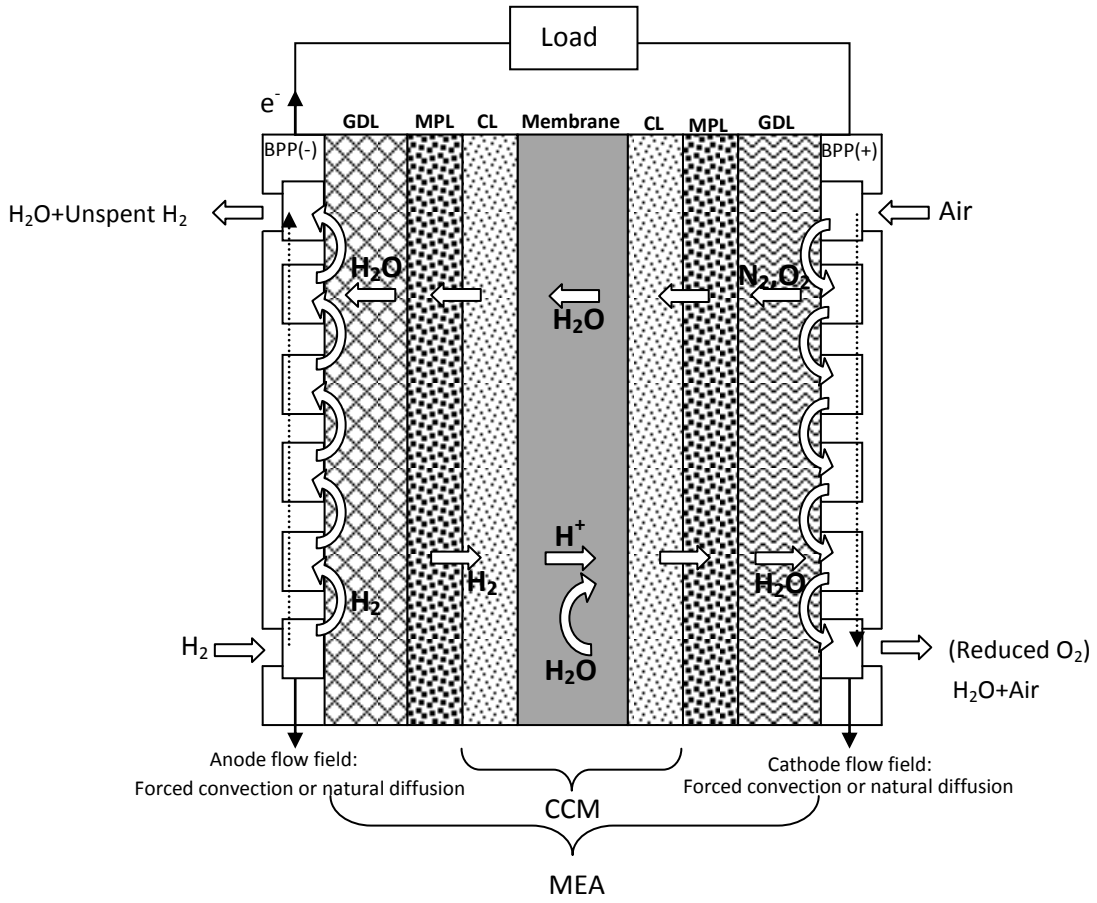

Figure 2.1. PEFC components and processes. Air is assumed to be composed of Nitrogen N_2 and Oxygen O_2.

Each side of the membrane is composed of CL, MPL, GDL and bipolar plate (BPP). The CL and membrane are often supplied as a single unit, namely a catalyst coated membrane or CCM. A CCM together with the anode GDL and cathode GDL is commonly termed

membrane electrode assembly (MEA) [1],[3],[4]. In other words, BPP and MEA are the two components that form a single cell of PEFC.

2.2.1 Bipolar plate

BPP provide reactant supply channels, facilitate water and thermal management and conduct current between cells as well as constitute the structural rigidity of the PEFC [5],[6]. The bipolar plates, either metallic or graphitic based plates, generally should meet the following requirements [7]:

- In plane conductivity of higher than 100 S cm^{-1}
- Area specific resistance of less than 30 mΩ cm^2
- Chemical stability for slightly acidic water with pH less than 4
- Corrosion resistance of less than 16 μA cm^{-2}
- No or very low surface degradation
- Thermal conductivity of higher than 10 $W(mK)^{-1}$
- Thermal stability at fuel cell operation temperature from -40 ^{o}C to 120 ^{o}C
- Tensile strength of higher than 41 MPa
- Zero gas permeability

The properties clearly show that the plate must be a non-porous rigid material with many channels and be impermeable to water, hydrogen and oxygen. New research is being conducted to develop multilayer BPP to reduce manufacturing costs yet to improve the reliability of the plates for the PEFCs [8].

The raised channelled area of the BPP, as shown in Figure 2.1, contacts the micro diffusion part of the membrane electrode assembly, the GDL.

2.2.2 Gas Diffusion Layer

The GDL essentially has three key roles in a PEFC; (i) to provide pathways for reactant gases from the gas channels of the BPP to be transported heterogeneously to the catalyst layers; (ii) to enable product water to be transported from the catalyst layer to the flow field channels and; (iii) to provide pathways to electronically connect the catalyst layer to the BPP. Therefore, the GDL is designed and manufactured to have the following functions:

- It is porous both in-plane and through-plane.
- It is electrically and thermally conductive both in-plane and through plane.
- It is hydrophobic to ease water transport.

The electrical and thermal conductivities are granted through material selection. As a result, they are mainly carbon based materials. GDL are available in the form of carbon cloth, carbon paper or carbon felt.

Carbon cloth is a textile consisting of woven bundles of 200-300 carbon fibrils per yarn; whereas carbon paper and felt consist of randomly dispersed carbon fibrils. In any case, the individual carbon fibrils are around 5-20 μm in diameter, while bundle diameter can be in the region of 400-500 μm as shown in Figure 2.2 and Figure 2.3 [1],[9],[10],[11]. The largest pore diameters in carbon paper and carbon cloth are around 40 μm and 250 μm respectively. The porosity of such materials depends upon the fibril content, the bundle dimensions and woven structure. However, the electrical and thermal conductivity can change in inverse proportion to the material porosity.

For hydrophobicity, GDL substrates are coated with hydrophobic materials like poly tetra flour ethylene (PTFE) or fluorinated ethylene propylene (FEP). Those materials can influence both the porous network connectivity and the electrical conductivity of the GDL depending on the coating and material loading process.

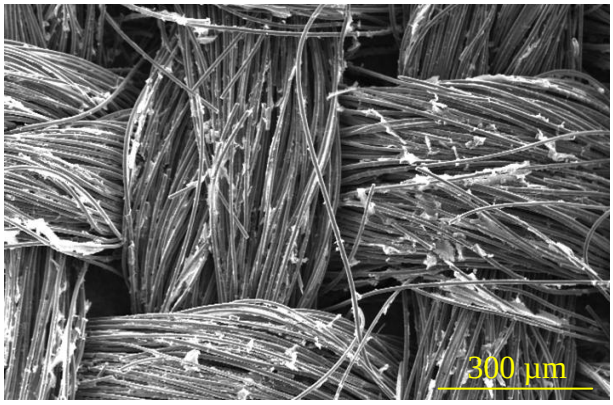

Figure 2.2. An SEM image of a woven carbon cloth gas diffusion layer with PTFE coating.

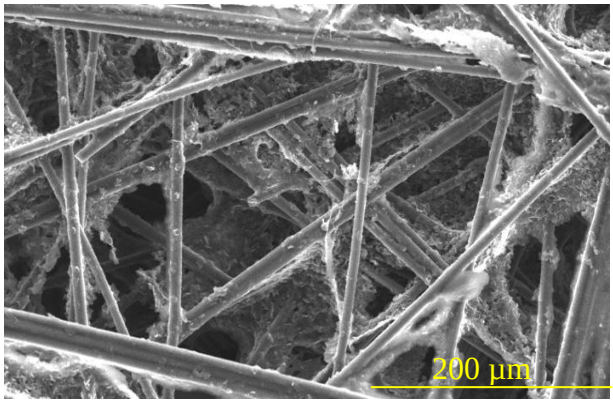

Figure 2.3. An SEM image of a nonwoven carbon paper gas diffusion layer with PTFE coating.

The side of the GDL adjoining the catalyst layer is commonly coated by microporous layer to enable better electrical conductivity and better water transport.

2.2.3 Microporous layer

The MPL is carbon or graphite mixed with PTFE binder. It is a porous medium with a high degree of hydrophobicity and plays a key role in transporting product water and reactant gases to and from the CL, as well as providing pathways for electron conduction. It is similar in nature to the GDL and serves a similar role but is much more hydrophobic and has lower porosity than the GDL. Typically the resulting pores are between 100 nm to 500 nm as shown in Figure 2.4 and Figure 2.5. In terms of water management, the function of the MPL is to push water away from the cathode GDL and move it through the anode. Better ohmic behaviour and catalyst utilization are the other possible features of the MPL [1],[3],[12],[13].

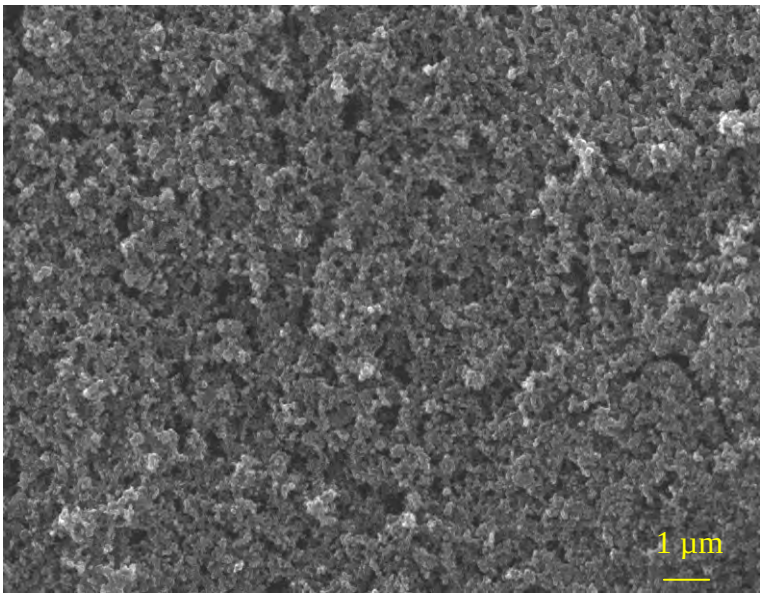

Figure 2.4. SEM image of the surface of a developmental MPL with pore sizes up to 500 nm.

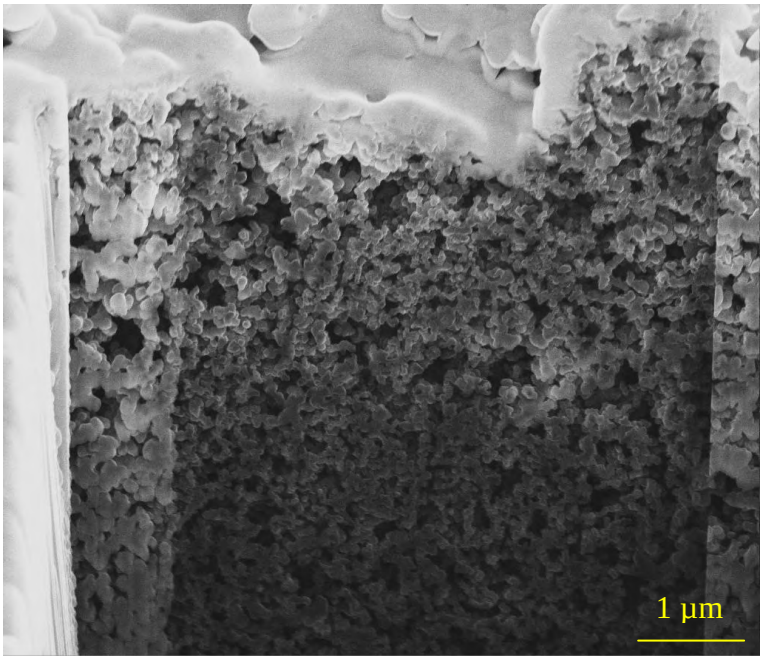

Figure 2.5. SEM image of an MPL cross section.

The catalyst layer, probably, the most important part of the fuel cell is adjacent to the MPL.

2.2.4 Catalyst Layer

The CL is the layer where electrochemical reactions take place on the surface of the catalyst. The most common catalyst in the PEFC is platinum. Since large catalyst surface area helps the reaction, it is desirable that dispersed Pt nanoparticles are evenly deposited on the surface of the layer [1],[3].

In reality, CL is a heterogeneous structure with a range of nano scale features. The CL can contain a multi-modal distinctive pore distribution centred around 50-100 nm. Carbon grains which are typically of 10 nm order that can agglomerate to 100 nm clusters, and catalytic deposits on the carbon grains that are typically of 1 nm order in magnitude. They are illustrated in Figure 2.6 and Figure 2.7 [2],[14],[15]. Other support materials such as

Vulcan XC72R by Cabot, carbon Black Pearls BP 2000, Ketjen Black Intl. and Chevron Shawinigan, have been used widely [3].

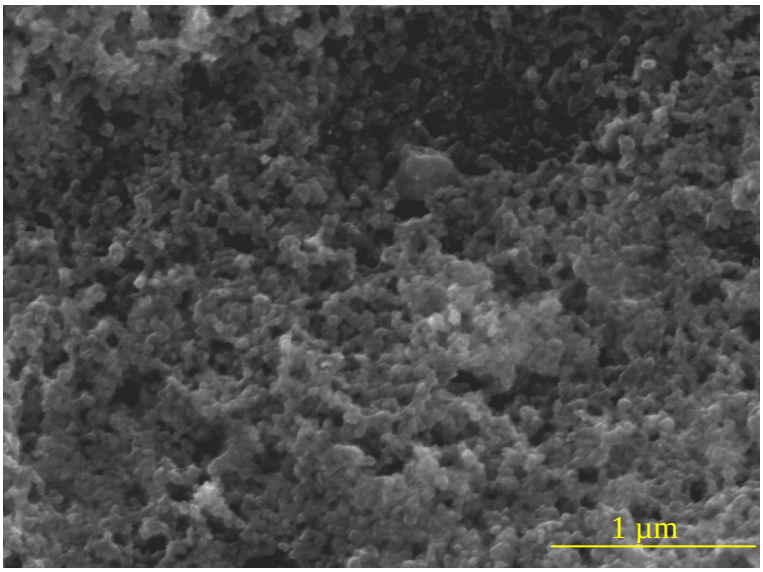

Figure 2.6. An SEM image of a cathode catalyst layer surface.

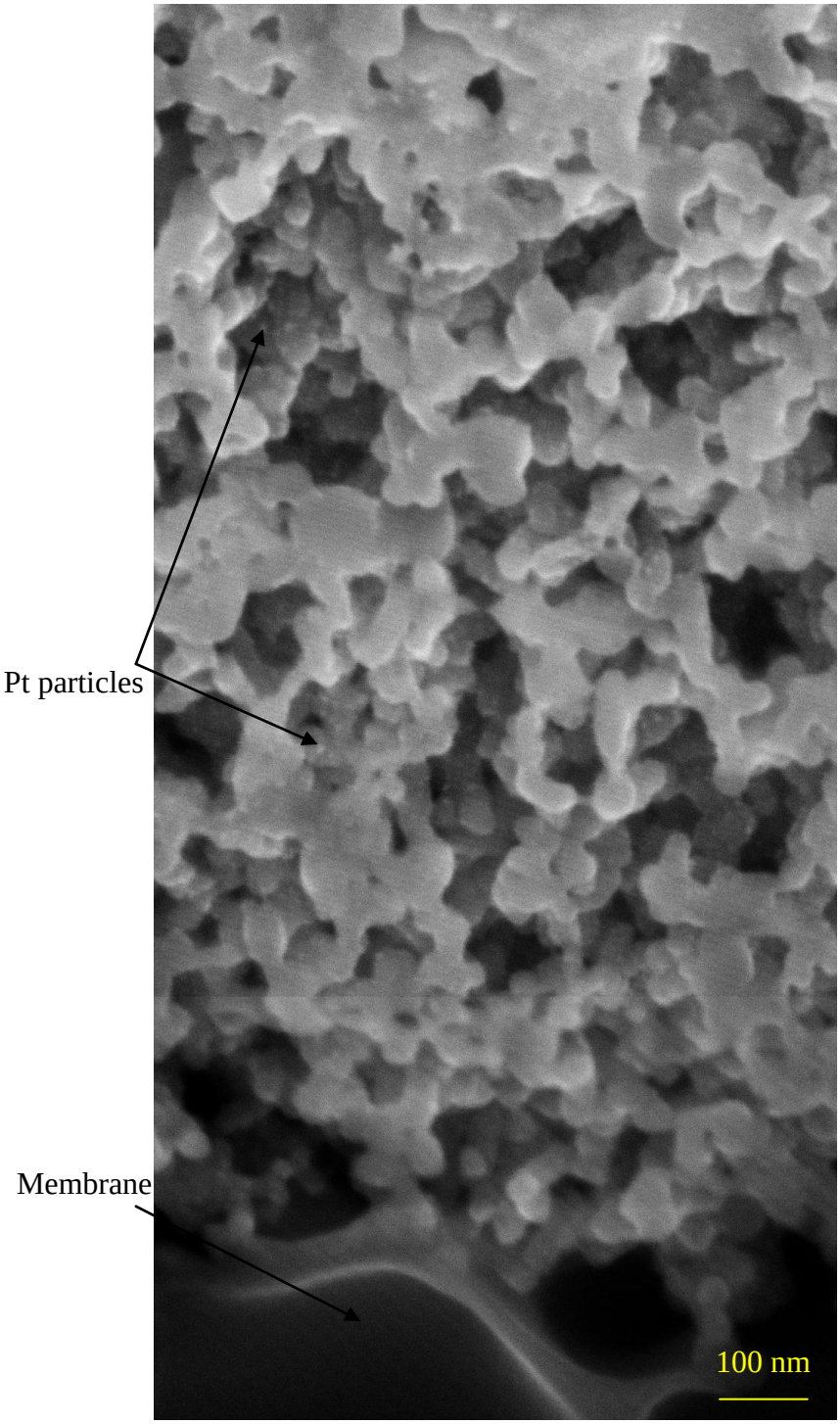

Figure 2.7 SEM image of a catalyst layer cross section. The bright spots as shown in the image are Pt particles with 2-5 nm diameter.

Research reports suggest Pt/C ratio should be above 40% by weight to minimize the cell potential losses [3]. Paganin et al [16], found that when the Pt/C ratio is varied from 10%

up to 40% with 0.4 mg/cm^2 Pt loading, the cell's performance remains unchanged. However, with Pt/C ratio higher than 40% the performance is declined. This shows that there is a negligible change in the catalyst active area when the Pt/C is between 10% to 40% and a significant deterioration in the active area beyond 40%. Therefore, the key to improve the PEFC performance is increasing the Pt usage in the CL [17]. Several studies show that the active area may be greatly increased if around 28% amount of ionomer of membrane is included in the catalyst layer [18],[19],[20]. Therefore, typically, the CL is deposited on the membrane.

2.2.5 Membrane

A PEFC membrane must exhibit an adequate barrier to mixing of gases and fuel and must have high proton conductivity. As shown in Figure 2.8 and Figure 2.9, membranes are porous, especially at the contact with the catalyst layer, but impermeable to gas.

Typically, the membranes for PEM fuel cells are made of perfluorocarbon-sulfonic acid ionomer. The most advanced membrane material is Nafion^{TM} from Dupont, which is composed of perfluoro-ulfonylfluoride ethyl-propyl-vinyl ether and has a proton conductivity of about 0.1 S/cm at room temperature [21],[22].

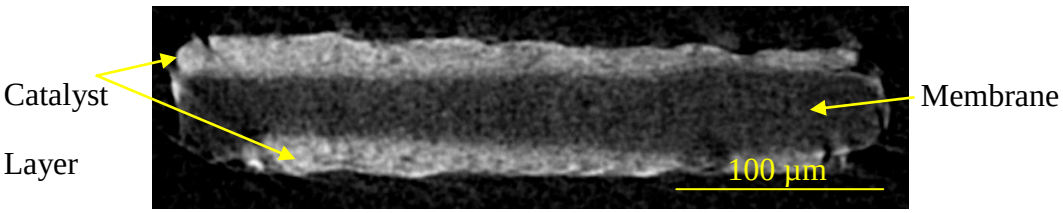

Figure 2.8. A cross section of a membrane coated with catalyst layer scanned with X-ray.

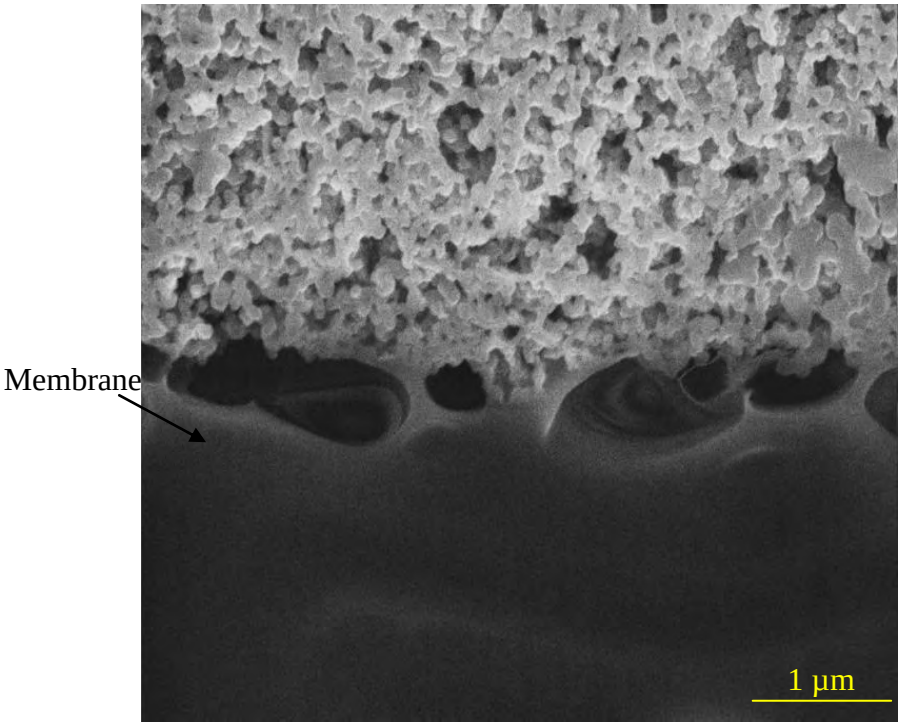

Figure 2.9. SEM cross section image of a membrane coated with catalyst layer.

The most important function of the membrane is proton conduction which relies on the excessive protons originated from the sulfonic groups and it takes place in the water domains of the membrane. Different transport mechanisms of water including diffusion, electro-osmotic drag and permeation need to be properly balanced to keep the fuel cell performance high. As the key function of the membrane is proton conduction, research is mainly concentrated on the material development, composition and solid structure of the membrane [22],[23],[24].

As previously mentioned, any of the primary components play an important role in fuel cells and participate in at least one of the three phenomenological processes at a fundamental level; (i) multi-component, multi-phase fluid transport; (ii) electrochemical reaction and; (iii) heat transfer. However, this research is mainly concentrated on the fluid transport phenomenon of the permeable porous layers of the PEFC including GDL, MPL

and CL. Therefore, gas and water transport models are discussed in the next section. A comprehensive review of other models including fuel cell modelling, thermodynamics, ion and proton transportation, and membrane models can be found elsewhere [25],[26],[27].

2.3 PEFC LAYERS FLUID TRANSPORT MODELS AND SIMULATIONS

Macroscopic and pore-scale modelling are the two general classifications of fluid transport models through PEFC layers. Macroscopic models are strongly based on homogenization along with microscopic details incorporated in them. In contrast to macroscopic models, pore-scale models pay specific attention to the geometric details of each layer. Below, both models are discussed to understand key structural and transportation parameters of the layers.

2.3.1 Diffusion media governing equations and macroscopic models

In macroscopic models, GDL and MPL are normally referred to as diffusion media since they are the porous backings between CL and the gas channels to provide a pathway for gases and liquid water to or from the catalyst layer. CL hosts electrochemical reaction as well as diffusion media for fluid transport through the thin catalyst layer.

Below, approaches for both types of transport, gas transport and water transport, are examined.

2.3.1.1 Gas phase transport

Stefan-Maxwell equations are used for every model dealt with gas phase transport in PEFC layers analysis:

$$\nabla m_i = \sum_{j \neq 1} \frac{m_i N_j - m_j N_i}{c_T D_{eff_{i,j}}} \tag{2.3}$$

where $N_{i,j}$, c_T, m_i, D_{ij} are flux density of species i and j (mol/cm^{2}s), the total concentration or molar density of all of the gas species, mole fraction of species i, and effective binary interaction parameter between species i and j respectively. The effective diffusion is defined as:

$$D_{eff_{i.j}} = \frac{\varepsilon_G}{\tau_G} D_{i,j} \tag{2.4}$$

where ε_G and τ_G are the bulk porosity and the tortuousity of the gas flow if the water is ignored otherwise another treatment is required as discussed in the next section. Typically, Bruggeman is used to model the tortuousity [28],[29],[30],[31]:

$$\tau_G = \frac{1}{\sqrt{\varepsilon_G}} \tag{2.5}$$

However, the expression above is based on the porosity of packed spherical particles and cannot predict tortuousity closely especially at low porosities. By contrast, Tomadakis et al, and Gostick et al [32],[33], proposed the following tortuousity model based on the Monte Carlo simulations for randomly oriented fibrous porous media:

$$\tau_G = \varepsilon_G \left(\frac{\varepsilon_G - \varepsilon_p}{1 - \varepsilon_p} \right)^{\alpha} \tag{2.6}$$

where ε_p and α are the suggested percolation threshold porosity ($\varepsilon_p = 0.11$) and fitted value ($\alpha = 0.521$ or $\alpha = 0.785$) obtained from the model. The percolation threshold porosity is the minimum porosity with an open pore space connectivity required for permeation through the porous material. Nam et al, clearly discussed the tortuousity appropriate function with different levels of porosities and models [34]. Other models including analytical fractal model and 3D stochastic reconstruction of the GDL paper predict average value of tortuousity for carbon paper GDL ranging from 1.14 to 2.2 [35],[36].

The gas diffusion model discussed above is in reference to Fick's diffusion [30] where the mean free path of a molecule is two orders of magnitude less than the pore radius. However, when the pore sizes are reduced, e.g. in MPL, another kind of diffusion dominates.

When the pore sizes are smaller, molecules collide more with the pore walls than with each other. The pore wall interaction is known as Knudsun diffusion [30]. In the models, Stefan-Maxwell diffusion and Knudsen diffusion are combined as mass transport in series [37]:

$$\nabla m_i = -\frac{N_i}{c_T D_{eff,k}} + \sum_{j \neq 1} \frac{m_i N_j - m_j N_i}{c_T D_{eff_{i,j}}} \tag{2.7}$$

where $D_{eff,k}$ is the effective diffusion coefficient.

When the mean-free path of a molecule is greater than 10 times the pore radius, Knudsen diffusion dictates. In other words, Knudsen diffusion dominates when the pore radius is less than ~500 nm. For reference, a microporous layer has pores between 20 nm and 1 μm [13],[38]. Consequently, while Knudsen diffusion may have to be neglected for GDL, it should be considered for MPL and CL.

Although most models are based on the pure diffusion, many models take the convection into account. One usual method, as with many CFD models, is to include Darcy's law for the gas phase as a separate momentum equation:

$$v_G = -\frac{k_G}{\mu_G} \nabla P_G \tag{2.8}$$

where v_G, k_G, μ_G, P_G, are superficial velocity of gas, gas phase permeability, viscosity and pressure [25],[39],[40]. Parameters including gas phase permeability strongly depend on the microscopic geometry of the layers.

Both diffusion and convection are discussed for the gas phase transport and the important structural parameters are recognized. Water transport is critical in PEFC and studied in the next section.

2.3.1.2 Liquid water transport

A simple way to treat water in the fuel cell is to assume it is a solid species that occupies a certain volume fraction. This means that the gas phase volume is limited and hence the effective diffusion coefficient equation (2.4) is decreased [41],[42].

The next series of models assume that water exists in the form of droplets along the gas stream. It is a component of gas and has a negligible effect on the gas field velocity. However, there is a volume fraction decrease due to the water [43].

The two group models above are inherently one phase. Two phase models are required since the liquid water and gas interact to a certain extent in GDL and MPL.

2.3.1.3 Two phase flow models

Similar to the gas pressure driven flow, Darcy's law for the flow of liquid water is as follows:

$$N_L = -\frac{k_{hp}}{V_L \mu} \nabla P_L \tag{2.9}$$

where N_L, k_{hp}, V_L, μ and P_L, are superficial flux density of species liquid water, effective hydraulic permeability, molar volume of water, viscosity and liquid phase pressure respectively. A lot of models use the above expression and essentially such model suggest

that there are liquid pores and isolated gas in the layer. This assumption is close to reality since the medium contains pores, hydrophobic and hydrophilic material [39],[44],[45],[46].

Phase mixture approach is another way to model two phase flow. In this model the two phases are considered as a single phase mixture. Therefore mixture parameters are used. As equation (2.7) suggests the mixture moves with a single velocity and does not have a separate driving force.

Although such simplifications help the computation time and numerical analysis, the real case requires the capillary equations for a close understanding of two phase flow.

The interaction between gas and liquid is influenced by capillary pressure P_C, surface tension γ, capillary pore radius r_C and contact angle θ that a water drop forms with the solid surface [25],[49]. The capillary pressure model is given by:

$$P_C = P_L - P_G = -\frac{2\gamma\cos\theta}{r_C} \tag{2.10}$$

The amount of pore volume that is filled with air as a function of water saturation s, is expressed by:

$$\varepsilon_G = \varepsilon_B(1-s) \tag{2.11}$$

where ε_B is the bulk porosity. This means that the saturation affects the gas phase diffusion greatly as predicted by Tomodakis and Sotirchos [50]:

$$D_{eff_{i,j}} = D_{i,j}\varepsilon_B\left(\frac{\varepsilon_B-\varepsilon_p}{1-\varepsilon_p}\right)^{\alpha}(1-s^2) \tag{2.12}$$

To relate capillary pressure to saturation, a new model has been developed by Weber & Newman [51] using a random cut-and-region bundle-of-capillaries to integrate the

hydrophilic/hydrophobic pore size distributions (PSD) of the diffusion layers to get the saturation through the idealized porous layer. However, for any of the models, the capillary pressure must be determined at every position. The gas and liquid pressure profiles must be known.

Although some models include gas phase pressure-driven flow in the diffusion media, the effect is not significant. Almost all of the models show that the pressure difference through the sandwiched layer is minimal, and the uniform gas pressure assumption is probably accurate for most conditions [25].

A typical way uses Darcy's law, equation (2.9), and combines it with equation (2.10) with the assumption of uniform gas pressure.

$$N_L = -\frac{k_{hp}}{V_L \mu}\nabla P_L = -\frac{k_{hp}}{V_L \mu}(\nabla P_C + \nabla P_G) = -\frac{k_{hp}}{V_L \mu}\nabla P_C \tag{2.13}$$

$$k_{hp} = k_r k_{sat} \tag{2.14}$$

where k_r, k_{sat} are relative permeability and saturated permeability respectively. k_{sat} only depends on the structure of the medium and has been either calculated using Carman-Kozeney equation [39] or assumed to be a fitting parameter. k_r is assumed to be linear or cubic function of saturation [25],[52],[53].

The importance of equations (2.13) and (2.14) is that both capillary pressure and hydraulic permeability are strongly dependent upon the structure detail geometry, i.e. equation (2.10) shows that capillary pressure is directly related to the pore size and PSD. The hydraulic permeability is again related to the porous medium geometry details.

The models above are macrohomogeneous models and are applicable to GDL, MPL and CL. The macroscopic models use a variety of averaged parameters including tortuousity, permeability, effective diffusivity, porosity and pore size distribution which are inherently

based on the detailed geometrical information of the layers at microscopic level. Microscopic or pore-level modelling, again applicable to all layers, is examined in the next section.

2.3.2 Pore-scale models and simulations

Pore-scale transport through porous media can be classified into three main categories: (i) pore network modelling; (ii) pore morphology modelling and (iii) Lattice Boltzmann modelling [54]. Other models including, molecular dynamics and CFD models are either computationally very expensive or still remains a challenge to simulate fluid flow in the complex PEFC porous layer. Information about the models could be found elsewhere [55],[56].

2.3.2.1 Pore network modelling

In the pore network based models, adequate physics of transportation are incorporated into the idealized pore network of the porous layers. Simulations based on all kinds of models are generally faster due to the simplified physical description and small systems of equations. One of the most famous models is the pore network modelling approach in which a fibrous medium is assumed to be a lattice of wide pores connected by narrow throats [57],[58],[59],[60],[61]. The morphology of a porous medium is characterised by pore and throat size distribution and their connectivity. Pores are typically nodes on a cubic lattice (or spherical) with cubic pore (or cylindrical) bodies connected by square cross-section (or circular) throats. The pore network can be constructed through mathematical Weibull cumulative distribution in which the distribution parameters can be adjusted to achieve a particular PSD and the throat sizes can be assumed to be equal to the smallest pore size nearby [62]. In the case of GDL, incompressible laminar flow in a throat is assumed. Only one fluid resides in a throat and the resistance of pore/flow is

assumed to be negligible [62]. A number of pore network models are currently applied to the PEFC layers.

Sinha et al, employed the pore network model to simulate liquid transport in a hydrophobic carbon paper GDL. The study shows the formation of irregular patterns of liquid movement in GDL/gas channels [63]. The extended model was used to model fluid transport in a mixed wettability GDL and found the saturation profile along the diffusion layer local thickness as a function of hydrophilic pores fraction [64].

Gostick at al. employed a two phase pore network model GDL to study capillary pressure-saturation relations for different GDL carbon papers [62],[65].

Bazylak et al, investigated the influence of the network size, structure on capillary pressure and relative permeability. The study suggests that the capillary pressure is highly affected by the structure heterogeneity while the relative permeability changes significantly with water saturation [66]. Similarly, Lee et al, recently suggested that saturation is lowered if the thickness of the GDL is reduced [67].

The pore network models are then strongly related to the basic parameters including PSD, local thickness and heterogeneity of the structure.

Another similar approach is pore morphology modelling that links the macroscopic details of the layer to an accurate representation of the porous layers via the input of morphological information.

2.3.2.2 Pore morphology modelling

The pore morphology approach uses the grain size distribution, pore radius, PSD and porosity of the porous medium to model the drainage process. It relies on a non-overlapping packing of a set of spheres and a digital representation of this. The key steps

are: (i) the entire pore network is saturated with liquid and the capillary pressure is set to zero. One end is connected to the non-wetting phase and the other end is connected to the liquid phase; (ii) the capillary pressure is increased in such a way that the pore network is eroded. The erosion has a spherical shape with radius r_C according to the capillary pressure equation (2.10); (iii) at a particular capillary pressure those pores that have not a continuous connection to the non wetting phase are removed. The rest are filled with non wetting phase. The step is repeated until equilibrium is reached and the corresponding occupied volume fraction of pore space by liquid is then worked out [68]. There are various research groups working on PEFC layers modelling using the pore morphology approach.

Schulz et al [69], modelled the quasi-static drainage in 3D stochastic reconstructed carbon paper GDL and show the liquid water distribution at various capillary pressures as a result of pore morphology modelling. The research indicates that liquid water penetrates into the gas saturated space in a random form based on the capillary force and PSD.

Mukherjee et al, studied the influence of compression on the capillary pressure-saturation characteristics and showed that increased compression resulted in a more tortuous pore structure which in turn leads to capillary pressure increase [54].

Recently, Becker and co-workers [70], employed X-ray μCT to reveal the non-woven GDL microstructure and combine it with the pore morphology approach to investigate the capillary pressure-saturation relation and emergence of water at the bubble point.

The above methods try to incorporate diluted physics on top of an idealized pore network. Such models are strongly related to the morphological parameters such as PSD, porosity, capillary and pore radiuses.

Unlike the aforementioned methods, there is another approach solving the Navier-Stokes governing equations either by CFD [55], molecular dynamics [56] or Lattice Boltzmann modelling. As mentioned in section 2.3.2, CFD and molecular dynamics are beyond the scope of this review. Therefore, in the next section LB modelling is examined.

2.3.2.3 Lattice Boltzmann modelling

The LB method is a numerical model based on kinetic theory to simulate fluid dynamics [71],[72]. The concept of the LB method was introduced by McNamara and Zanetti to develop its predecessor, the lattice gas algorithm [73],[74]. Unlike conventional computational fluid dynamics, the LB method tracks the streaming and collision of a collection of pseudo-particles in a lattice, which interact according to a velocity distribution function. The LB model used in this work will be described in detail in Chapter 3.

With the LB method, it is relatively facile to deal with complicated boundaries and various forces at microscopic scales and therefore it becomes more efficient to simulate flows in complex porous media at pore-scale. The LB incorporates phase segregation and surface tension in multiple flows analysis which are difficult to implement in traditional CFD methods. A number of research projects employed the LB method to simulate either single phase flow or multiple phase flow for the fuel cell layers.

Hao and Cheng [76], recently used the LB method to study the anisotropic permeability of a GDL. The carbon papers were reconstructed through stochastic method. The simulated permeability was compared to the measurements and an existing analytical model such as Kozeny-Carman equation.

Similarly, in the work reported by Van Doorrnaal and Pharoah [77], LB was used to simulate idealized PEFC porous layers. The results show that fibre arrangement plays a significant role in the permeability of the layers.

In the work presented by Kim & Pitsch [78], a stochastic method for the reconstruction of the CL was combined with the LB method to evaluate the effective diffusivity of the CL. The LB model was employed to consider the Knudsen number effects in the catalyst layer.

Mukherjee et al [79],[80], deployed the LB method to study two phase transport and flooding behaviour in the PEFC GDL and CL as well as the effect of liquid on the catalytic site coverage and pore blockage. The CL and GDL microstructure were obtained through stochastic reconstruction.

Finally, Ostadi et al & Rama et al [13],[81],[82],[83],[84],[85],[86], developed the LB modelling, both single phase and two phase, coupled with the micro/nano tomography images of GDL & MPL to anticipate the liquid water breakthrough, air permeability, anisotropic permeability, tortuousity and effective diffusivity of PEFC porous layers.

From the above review, it is obvious that detailed description of porous layers is an essential requirement for both pore-scale modelling and macroscopic modelling. Stochastic reconstruction, homogenized and idealized geometries are the common approaches for quick simulations and widely used for GDL and CL [54],[69],[87] that rely on the materials porosity characteristics. Therefore, after understanding the PEFC layers modelling requirements, the next section is designed for experimental characterisation methods to obtain fundamental parameters such as porosity, pore size distribution, permeability and specific surface area per unit volume.

2.4 CHARACTERISATION TECHNIQUES

As discussed in previous section, Both macroscopic and pore scale models are strongly related to a number of parameters. Among those parameters, porosity, pore size distribution, pore radius, permeability, tortuousity, effective diffusivity, surface characteristics and surface area per unit volume play key roles in the fluid transportation within the PEFC layers. Hereinafter, established methods including a direct method for porosity measurement, standard and mercury porosimetry, air permeability test, surface analysis through the Brunauer-Emmett-Teller method, surface imaging including SEM & TEM and finally the recent micro/nano tomography techniques and their application to the PEFC layers are discussed.

2.4.1 Porosity characterisation through direct method

This is probably the simplest way to measure the porosity. The pore volume of a material can be calculated using total volume of the porous sample (e.g. thickness times surface area) and the volume of the solid portion of the material based on the sample basis weight and the components density (e.g. GDL is made of carbon fibrils and PTFE with a known density given by the manufacturer). The pore volume simply is then worked out by the subtraction of volume of the skeletal material from the total volume. The method is widely used in porous biomaterials applications [88],[89] as well as in GDL [1]. Uncertainty of this method significantly depends on the density which is usually given by the manufacturer, the materials purity and the accuracy of the thickness and surface measurement. The uncertainty has been reported to be around ±2%.

In the case of PEFC layers, Ostadi et al [90], employed the direct method to obtain a reference value to tune the threshold for binarization of GDL X-ray μCT images. The

uncertainty of the method in this work was reported to be ±1%. However, the above method is not applicable to CL and MPL due to the thinness of the layers.

It is critical to know the porosity of the MPL and CL as well as pore size distribution in all layers. Therefore in the next section, PSD characterisation techniques are discussed.

2.4.2 Pore size distribution characterisation techniques

For PSD of PEFC layers, there are mainly three techniques; (i) Capillary flow porometry, (ii) Standard contact porosimetry; and (iii) Mercury porosimetry. Each method is briefly described and the application on PEFC layers is presented.

2.4.2.1 Capillary flow porometry

The principle of the method is based on a wetting liquid allowed to fill the pores in the sample spontaneously while a non-reacting gas is allowed to remove liquid from the pores. The differential gas pressure P_{diff} yielded pore diameter D_p after Laplace equation (2.15):

$$D_p = \frac{4\gamma \cos\theta}{P_{diff}} \tag{2.15}$$

where γ and θ are surface tension and contact angle of the wetting liquid respectively. From measured gas pressure and flow rate pore throat diameter, pore size distribution and gas permeability are calculated. The method was used for GDL, and materials with pores larger than 300 nm in diameter [91],[92].

2.4.2.2 Standard contact porosimetry

The method is based on the law of capillary equilibrium throughout the entire volume of a system of two or more bodies contacting with each other. According to the Laplace equation (2.15) capillary pressure exists for all these bodies. The method involves weighing the amount of measuring liquid in the pores of the sample under investigation

relative to its amount of the standard porous sample in contact with it. Octane is usually used as the measuring liquid since it ideally wets nearly all materials.

The method is used for all PEFC porous layers for investigation of both structural and wetting properties, and it offers the possibility of investigating pores sizes over a wide range of D_p from 1 nm to 600 μm [93],[94],[95] with 1% uncertainty.

The method required a long time for performing the experiment and it relied on the measurement of the structure of the standard sample, which is normally done by the mercury porosimetry. In the next section the mercury porosimetry is studied.

2.4.2.3 Mercury porosimetry

Probably the best known method for porous structure investigation is the mercury porosimetry that can be used in a wide range of pore sizes from 1 nm to 1mm [96]. The method is based on intrusion of mercury into the open pores of the sample under high pressure. With external pressure, pores with a radius larger than the capillary radius r_C are filled with mercury. As mentioned in equation (2.10), the capillary pressure, equal to the external pressure, is expressed by:

$$P_C = \frac{2\gamma \cos\theta}{r_C} \tag{2.16}$$

where γ is 4.67 μJ cm^{-2} for mercury. As pressure increases, the cumulative pore volume is increased. From the cumulative pore volume and the pressure, pore diameter for a known contact angle is calculated. The theory supposed that pores are cylindrical in shape, interconnected and open to the surface of the porous material. The method is widely used for characterisation of porous PEFC layers especially for the CL.

Reported by Xie et al [97], mercury porosimetry is employed for three differently deposited CL to measure the porosity. The study reveals that higher porosities in the CL may result in lower fuel cell performance.

Park et al [98], characterised different CL through mercury porosimetry. They found that PSD and porosity are modified by controlling the temperature during fabrication.

Xie et al [14], used the mercury porosimetry along with SEM/TEM imaging techniques to reveal the PSD and porosity of carbon supports, with and without catalyst loading, and the CL of the MEA made by thin film decal process.

Park et al [99], modified the conventional MPL decal fabrication method and characterised the new MPL in terms of porosity and pore size distribution. The modified method uses a carbon breaking layer that makes a higher catalyst transfer ratio during the process.

Recently, Park & Popov [100], used mercury porosimetry along with SEM micrographs and showed that hydrophobic agent changes the surface and bulk structure of the GDL.

Presented by Park et al [101], the effect of carbon loading in MPL on PEFC performance was investigated. The average pore diameter and total pore volume along with the PSD of the different MPL were revealed. The mercury porosimetry also shows that part of the MPL penetrates into carbon-fibre substrate during spray deposition of carbon ink.

Porosity and pore size distribution characterisation methods are not limited to the three methods above. Small angle X-ray scattering [102], and capillary condensation [103] are the methods only suitable for the range of pores radii which are between 1 nm to 50 nm.

Permeability is another key parameter which relates to the porosity of the material. Herein the next section considers air permeability tests.

2.4.3 Gas permeability characterisation

Gas permeability characterisation through pressure drop is straightforward and commonly used in a wide range of porous materials including soil, thin polymeric films and composites [104],[105],[106],[107]. According to Darcy's law, equation (2.8), the gas permeability $k_{G,}$ can be estimated by measuring pressure drop and observing the flow:

$$V_G = -\frac{k_G a}{\mu_G l}\nabla P_G \tag{2.17}$$

where V_G, a, l are the volumetric flow rate, cross sectional area through which flow passes and the thickness of the sample respectively. It is used to characterise PEFC layers as well.

Caston et al [108], used the method to investigate the effect of weave tightness and structure on the in-plane and through-plane permeability of a woven GDL. The research also shows that the percentage of macro pores in the weave is the key factor in determining the through-plane permeability.

Finally, Pozio et al [109], and Chun et al [110], investigated the effects of different fabrication methods and composition of GDL-MPL on the gas permeability and morphology of the layers.

Porosity, pore size distribution and permeability characterisation techniques were reviewed. The morphology of the PEFC layers also requires pore surface analysis. The next section tries to summarize the current methods in pore surface analysis and their application in PEFC layers.

2.4.4 Specific surface area analysis

The external surface specific area is insignificant compared to the internal surface including the pores walls which are assumed to be cylindrical with an average diameter of $D_{p,avg}$. As an initial approximation and can be given by the following equation [111]:

$$S_S = \frac{4V_{PT}}{D_{p,avg}} \tag{2.18}$$

where S_s and V_{PT} are the specific surface area and specific total pore volume. Application of this formula requires prior knowledge of pore volume and pore diameters which can be determined through the porosimetry methods presented in the previous sections.

Practically, the popular method used in catalysis is the Brunauer-Emmett-Teller (BET) method based on the adsorption of a gas at constant temperature. The principle of measurement relies on determining the point when a single molecular layer of gas forms on the surface of the catalyst. If the single layer volume is V_m, for a gas with molar volume of V_M the specific surface will be written as:

$$S_S = \sigma_{molecule} \frac{V_m}{V_M} \cdot N_A \tag{2.19}$$

where $\sigma_{molecule}$ and N_A are the surface of an adsorbed molecule and Avogadro constant.

Various researchers signify the importance of surface area in the GDL and used either the mercury porosimetry data or BET method for surface area calculation [112],[113],[114]. The method is more common for CL characterisation [115],[116],[117].

Porosity, pore size distribution and pore surface area characterisation techniques rely on accessibility through open pores and do not provide information about tortuousity, shape, position or interconnectivity of the pores. Imaging techniques such as SEM/TEM provide more details about the porous layers.

2.4.5 Two dimensional surface imaging analysis through SEM and TEM

A scanning electron microscope scans a sample through a high energy beam of electrons in a rectangular pattern. The electrons interact with the atoms of the sample surface and produce signals that contain information about the surface geometrical shape and composition. The most common imaging mode of the SEM is secondary electrons which collects secondary electrons ejecting from the k-orbits of the sample atoms by inelastic scattering interactions with the electrons beam. The spatial resolution can fall less than around 1-3 nm [118]. Higher resolutions are possible through TEM.

In TEM, a beam of electrons is transmitted through a very thin sample, typically 100 nm, interacting with the atoms as it passes through the sample and forms the image. The theoretical resolution of the method is reported to be around 42 pm. However, in practice this value is around 50-100 pm [119]. Both SEM and TEM imaging are widely used in fuel cell layers characterisation and modelling [120].

Cheng et al [121], operated single-cell PEFC for different lengths of time. Both SEM and TEM imaging were used to investigate structural and morphological changes in surface and cross section of the fuel cell CL. Additionally, an agglomeration in catalyst nano particles was observed through TEM images.

Reported by Mukherjee & Wang [87], a 2D image of the surface of a CL taken by TEM were used to reconstruct the 3D representative image of a CL via stochastic reconstruction and coupled it with numerical simulations to obtain a pore-scale description of concentration and potential fields. The method signifies the influence of inhomogenity of the CL on the fuel cell performance.

Similarly, Thiedmann et al [122], used GDL surface SEM images and detected a thin section from the images to model the GDL 3D structure through stochastic reconstruction. The quality of the structural model was compared to the synchrotron tomography images of the GDL in terms of the distribution of spherical contact distance to fibres seen from an arbitrary chosen point of the pore space.

Tang et al [123], investigated porosity graded MPL microstructure through SEM images. They show that fuel cells with graded porosity are beneficial for the electrode process cell reactions, probably due to the easier water transportation via larger pores while gas diffuses through smaller pores.

Finally, Ostadi et al [90],[126], utilized the SEM image of the GDL surface to finely tune the threshold for binarisation of grey scale X-ray μCT/nCT images of the same GDL. The finely tuned binary images were then used for pore characterisation.

Although, 2D SEM and TEM images give a good understanding of PEFC layers in many characterisations and modellings [34],[36],[124],[125], they are limited to the surface. For a thorough understanding of PEFC porous layers, 3D imaging analysis is required.

2.4.6 Three dimenstional reconstruction through micro/nanotomography

Three dimensional reconstruction involves assembling thin slices of an object to create the 3D digital structure either destructively or non-destructively.

Non-destructive methods such as PET (Positron Emission Tomography), SPET (Single Photon Emission Tomography), MRI (Magnetic Resonance Imaging) ,TEM tomography, electron beam tomography, X-ray μCT and X-ray nCT involve reconstructing 2D projections of an object viewed from different angles derived from Radon function. Radon function computes the line integrals from multiple sources along parallel beams, or paths,

in a certain direction assuming that projection of a 2D image (function) is a set of lines (line integrals). Therefore, with a sufficient number of projections, an inverse Radon transform should result in reconstruction of the object. In practice, less computationally expensive methods such as backprojection methods are used. Backprojection methods project each recorded image back into the object space at the angle at which the original image was recorded [127],[128]. Although, the principle in non-destructive 3D reconstruction methods is similar, resolution of each method is different.

High resolution PET and SPET are limited by detector performance, and the resolutions are currently not better than 500 µm [129]. X-ray µCT and a conventional MRI microscope have a typical resolution of 5µm. The recent nuclear MRI technique can provide a resolution up to 90 nm [130]. The resolution of the imaging systems is either limited by imperfection in the lenses or misalignment, or by diffraction, which is determined by wavelength [131]. The most recent X-ray synchrotron facilities enables characterisation of various materials with a spatial resolution down to 22 nm [132],[133]. X-ray transmission microscopy and electron tomography resolutions are reported to be around 1 nm, although the sample thickness is limited to a few hundred nm [134],[135]. For MPL and CL characterisation, thick samples around 5 µm and resolution of better than 20 nm is required. The FIB/SEM nanotomography destructive technique would be a solution.

It is called destructive since the method is based on milling (polishing) away a thin slice from the sample surface through ion beam, e.g. heavy Ga^+ ions, and recording an SEM image of the new surface. Repeating the milling-recording process generates a stack of SEM images which enable reconstruction of the structure through assembling the slices [136].

The polishing-imaging method was used to reconstruct high manganese steel through metallographic polishing and SEM imaging to investigate grain disorientation in 3D [137].

Recently, there have been examples of FIB/SEM nanotomography as well as X-ray μCT/nCT, applied to fuel cell characterisation.

Wilson et al [138], used the FIB/SEM nanotomography technique to reconstruct the solid oxide fuel cell anode. The 3D reconstructed image with 50 nm resolution enabled them to measure porosity, surface area of each phase and connectivity of the material at pore level. Moreover, the image was coupled with FEA to predict the tortuousity of the porous structure.

Similarly, Gostovic et al [139], employed the FIB/SEM nanotomography for three dimensional reconstruction of solid oxide fuel cell cathode at 20 nm resolution to measure porosity, closed porosity, graded porosity, surface area, tortuousity and PSD.

Very recently, Zils et al [140] and Ziegler et al [141], employed FIB/SEM nanotomography techniques to investigate morphological parameters of the CL and PEFC electrode with resolutions of 30 nm and 14.5 nm.

Ostadi et al [13], developed the FIB/SEM nanotomography to reveal the internal structure of the MPL with 14 nm pixel size and combine the tomography image with LB modelling to investigate the permeability and tortuousity of the thin MPL layer.

Recently, X-ray microtomography has been used to quantify liquid water saturation distribution in a porous GDL and determine the two-phase material parameters with sub 10 μm resolution [70],[142]. The latest report suggests that nanotomography (Nano XCT, California, US: Xradia Corp.) can be used to reconstruct the porous catalyst layer (CL) of

fuel cells at sub-micron resolution, in order to study changes in the membranes after transient operation [143].

The methods are not limited to the fuel cell layers characterisation. Ostadi et al [144], extended the FIB/SEM nanotomography method to measure the roundness of a micropipette tip with 60 nm pixel size. The micropipette roundness has a great effect in seal formation when used for cell grabbing experiments known as patch clamping. X-ray nCT has been successfully employed to scan porous human dentin tubules at 295 nm resolution and to reconstruct the 3D cylindrical structure of the porous tubules which are between 1 to 3 μm in diameter using the SkyScan 2011 desktop nanotomography system (Kartuizersweg, Belgium: SkyScan) [145].

2.5 SUMMARY

Main components of a modern PEFC including BPP, GDL, MPL, CL and the electrolyte membrane have been reviewed in section 2.2. The three permeable porous layers including GDL, MPL and CL were particularly chosen due to their noteworthy role in fluid transportation.

Fluid transportation governing equations including gas, liquid and two phase transport were studied. It was understood that there are mainly two methods for PEFC porous layers modelling: (i) macroscopic or macrohomogeneous models and; (ii) microscopic or pore scale models.

It was realized that macrohomogeneous models applicable to the GDL, MPL and CL use a variety of averaged parameters including tortuousity, permeability, effective diffusivity and porosity which are inherently based on the detailed geometrical information of the layers at pore scale. Pore scale models and simulations including pore network modelling,

pore morphology modelling, stochastic reconstruction, homogenized and idealized geometries and numerical LB modelling that rely on the pore network characteristics were reported.

Characterisation methods including a direct method for porosity characterisation, capillary flow porometry, standard contact porosimetry and mercury porosimetry for PSD characterisation, air permeability, specific surface area analysis through the BET method and 2D surface imaging through SEM/TEM were investigated.

It was recognized that although 2D SEM/TEM imaging provide important information of the surface, 3D imaging techniques including X-ray micro/nanotomography and FIB/SEM naotomography could greatly assist the real 3D characterisation. Therefore, a review on those current characterisation methods applied to fuel cell layers is given.

Reported work in this Chapter has a considerable influence on the direction of this research. The characterisation methods including X-ray μCT/nCT and FIB/SEM nanotomography for characterisation of the GDL and MPL/CL were selected respectively. The LB numerical modelling and simple analytical models to predict key parameters of the porous layers were identified for simulation and calculations. Therefore, in Chapter 3 the 3D characterisation and key parameter calculation through X-ray μCT/nCT combined with the LB model are reported.

3 CHAPTER 3: X-RAY TOMOGRAPHY AND STUDY OF THE THRESHOLD

3.1 INTRODUCTION

This Chapter explains the X-ray μCT/nCT imaging principles, parameters calculation method and fine tuning of the threshold for binarisation of tomography grey scale images. The Chapter is organised as follows: a study of the X-ray μCT/nCT imaging is given in section 3.2 and optimized X-ray imaging conditions including source voltage, source current and rotation step are recognized. Then, in sections 3.3, analytical methods and LB approach for calculation of structural and fluid transport parameters are discussed. In the process determination of the threshold for binarisation of X-ray grey scale images is critical. Therefore, in section 3.4 current thresholding techniques for binarisation of X-ray μCT/nCT images and their advantages and disadvantages are explained. In section 3.5, the influence of small threshold variation on determining the properties of a non-woven GDL is investigated. Then, a novel experimental method to accurately identify the threshold value for the GDL is reported. Similarly, in section 3.6 the influence of the threshold on the properties of a woven GDL is discussed and a similar novel experimental method for the fine tuning of the threshold is presented. Finally, this Chapter is summarised in section 3.7.

3.2 X-RAY μCT/NCT PRINCIPLES

X-ray μCT/nCT reconstructs an object by assembling the projected images of it, viewed from different directions as shown in Figure 3.1. Images are produced based on the level of X-ray attenuation which reflects the density of the sample. These grey scale projections are then used to make 2D slices corresponding to what would be seen if the sample was cut through the scanning plane. The slices are then assembled to reconstruct a 3D image [146]. X-ray images can be generated using high resolution μCT with 2-5 μm resolution and nCT with 20-50 nm resolution through desktop or synchrotron scanners. Synchrotron scanners provide parallel X-ray beams and therefore result in higher resolution and better image contrasts [127], while in desktop tomography, X-ray sources are not able to generate parallel beams. Instead, they use a point source which produces a small angle cone X-ray beam in the object area as seen in Figure 3.1. In this work, desktop tomography was employed.

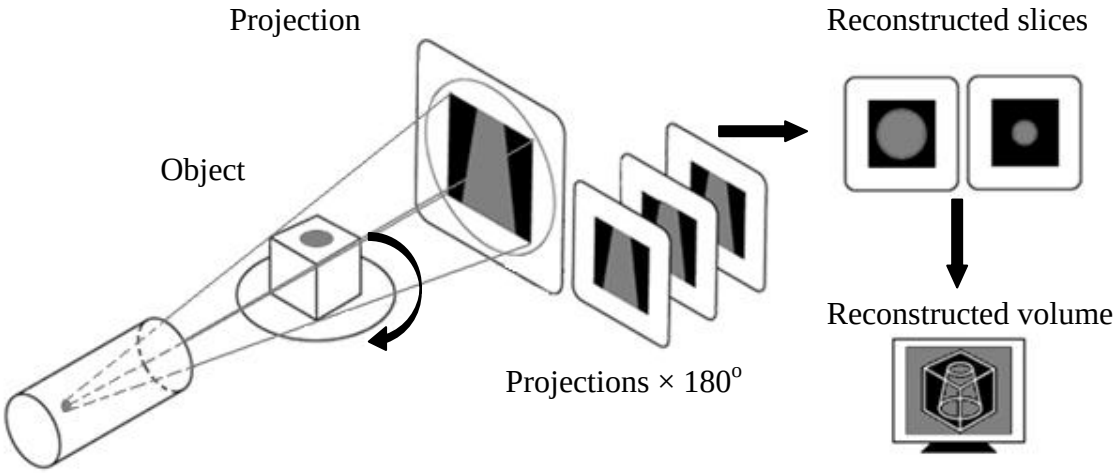

Figure 3.1. Schematic of Micro/nanotomography system.

In the process of desktop X-ray tomography there are generally three key steps: (i) image acquisition; (ii) backprojection and 2D slice reconstruction and; (iii) 3D reconstruction. The steps are explained further as follows:

3.2.1 Image acquisition

The principle of the desktop X-ray μCT (SkyScan 1072, SkyScan Ltd. Belgium) and X-ray nCT (SkyScan 2011, SkyScan Ltd., Belgium) , is shown in Figure 3.1. A sample is placed in front of an X-ray source and rotated step-by-step. Grey scale projections are then generated using an X-ray detector array. SkyScan 1072 system is equipped with an X-ray source of 100 kV (max) and 100 μA (max) and a minimum rotation step of 0.23 deg resulting in a maximum pixel size of 1.76 μm. SkyScan 2011 uses an X-ray source of 80 kV (max) and 200 μA (max) and a rotation step of 0.23 deg which gives a maximum pixel size of 200 nm. Although increasing the rotation steps would increase the accuracy of reconstruction, the cost of computational time is very expensive. Also, increasing the X-ray energy by current would result in a better image contrast therefore images are taken at the maximum current. However, increasing the X-ray voltage causes X-ray over-transmission, meaning that projections become over-bright especially when the X-ray passes through soft materials. Therefore, parameters recommended by many researchers and the machine manufacturer are: X-ray low voltage of 40-50 kV at 100 μA with rotation step of 0.9 deg for the μCT and 25-40 kV at 200 μA with rotation step of 0.5 deg for the nCT systems [147],[148],[149],[150],[151].

The X-ray detector used for both devices is a Hamamatsu X-ray camera, which contains a scintillator and a charge coupled CCD chip. The X-rays are converted to flashes of light by a scintillator screen (gadolinium oxide). The CCD chip is smaller in size than the scintillator and can be damaged by long exposure to X-rays. To lessen potential damage, a

tapered fibre-optic bundle is used, which is glued to the scintillator screen at one end and the CCD chip at the other. The bundle maintains an exact 1:1 translation of the position from the scintillator to the CCD chip. The camera employed in the SkyScan system has a 1024×1024 pixels CCD chip with a 12 bit depth. The minimum pixel size of a system is defined by the object diameter of the camera and the number of pixels across it. For instance, in the SkyScan 1072, the object diameter is around 1.8 mm. The maximum pixel size is therefore worked out as 1.8 mm divided by 1024 pixels, which gives 1.76 μm.

The 2D gray scale shadow images are then used to reconstruct 2D cross-sectional image slices, which correspond to what would be seen if the sample is cut through the scanning plane. The slice reconstruction is based on the backprojection method which is discussed in the next section.

3.2.2 Backprojection and 2D slice reconstruction

A simple example of a parallel beam backprojection method is shown in Figure 3.2. It is a grey point with high level of X-ray absorption in an unknown position within an object. In a projection image, a decrease in intensity of absorption within the object area will be seen.

An empty array of pixels corresponding to all possible object displacement can be initialized in the computer memory. Since the position of the projection from the absorption points are known, one can mark all possible positions of absorption points as lines in the computer memory.

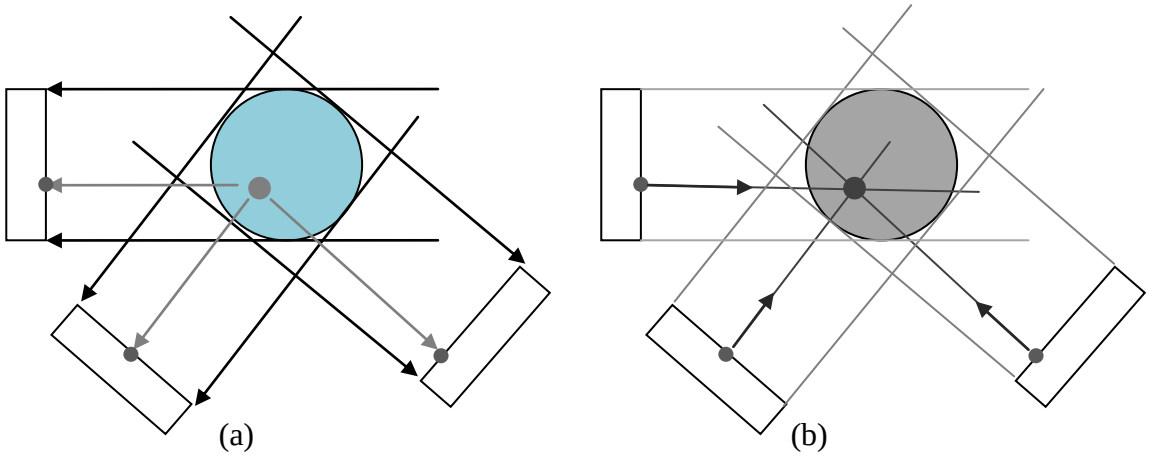

Figure 3.2. Projection and reconstruction of a single point in an object; a) Three different projections of a single point in an object and; b) The corresponding reconstruction from the projected data.

In each rotation step, the lines of possible positions of the point will be added to the area of reconstruction. After many rotation steps, the position of the absorption point in the reconstructed area will be localized. Increasing the number of projection by rotation steps, the localization becomes more defined, as illustrated in Figure 3.3 [147],[148],[152].

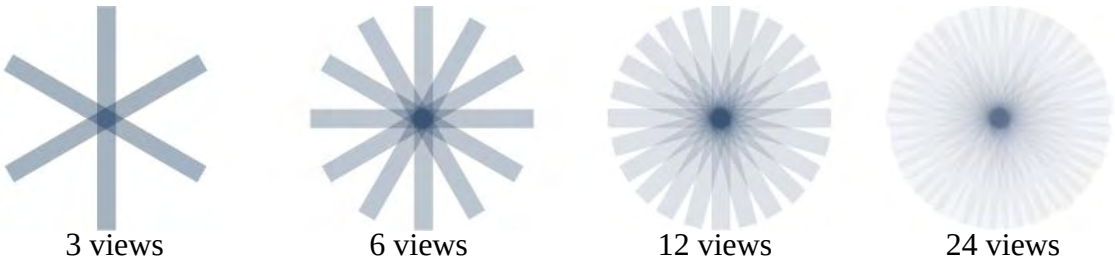

Figure 3.3. Reconstruction of a single point using different amount of rotations

By the backprojection method, thin grey scale slices of the sample correspond to what would be seen if the sample was cut through the scanning plane, were produced. The

thickness of each slice is equal to the pixel size of the projections, e.g., in an image with 1.76 μm pixel size in the projection images, the thickness of a slice is 1.76 μm.

It is now possible to reconstruct the 3D image from the 2D slices.

3.2.3 Three dimensional digital reconstruction

The 3D reconstruction is a standard process and the 3D image could be achieved either in grey scale or binary image by assembling the slices together. However, a binary 3D reconstruction process based on binary slices is much less time consuming than grey scale image processing. Therefore, in this work we only use the 3D binary images. There are two well-known algorithms that can be employed to carry this out: 'marching cubes 33' and 'double time cubes'. 'Marching cubes', which was developed by Lorensen and Cline [153], is a surface building process based upon an explicit hexahedral voxel model. 'Double time cubes' is smoother since the number of facet triangles is half the number of the 'marching cubes' method and is developed by Bouvier [154]. The SkyScan reconstruction software namely, CTAN, uses mainly the 'double time cubes' method [155].

As previously discussed, for pore analysis and 3D reconstruction, representative binary slices are required. Therefore, it is necessary to threshold the greyscale slices acquired from X-ray tomography in order to produce binary images [156],[157],[158]. A thorough understanding of threshold and a novel method for fine tuning is presented later in sections 3.5 and 3.6.

For a general binary image, structural and transport parameters including porosity, surface area, pore size distribution, porosity, characteristic lengths, structural degree of anisotropy, permeability, tortuousity and effective diffusivity could be obtained through 3D digital images as discussed in the next section.

3.3 KEY FLUID TRANSPORT AND STRUCTURAL PARAMETERS

Two approaches analytical and numerical are investigated in this section.

3.3.1 Analytical approach

In this section, key structural and fluid transport parameters discussed in Chapter 2, are calculated for an X-ray tomography binary image. CTAN, MATLAB and Visual C++ software were used for calculations. The Visual C++ code was developed at the University of Liverpool for LB modelling and used for calculation of permeability and tortuousity. CTAN and MATLAB along with analytical approaches were used for calculation of all other parameters.

3.3.1.1 Solid volume, pore volume and porosity

From a binary image, the solid (or pore) volume is the number of voxels of solid objects (or pore) times the voxel volume. Then, the porosity is simply the ratio between the pore volume and the total volume where the total volume is the sum of the pore volume and solid volume.

3.3.1.2 Solid and pore surface

The surface measurement is based on the surface of the double time cubes, i.e. the total number of facets times the surface of each facet.

3.3.1.3 Pore size distribution, mean pore radius and characteristic length

In the analysis of the 3D binary images, a 3D spherical local radius can be measured. Local radius for a point in pore is defined as the radius of a sphere which meets two requirements: (i) the sphere surrounds the point; (ii) the sphere is entirely bounded within the solid/pore surfaces. The distribution of the spheres' size is the pore size distribution, and the mean radius of the spheres is regarded as the mean pore radius [161],[162]. Also

the mean pore-pore distance or characteristic length [163] can be calculated by averaging over distances between spheres.

3.3.1.4 Degree of anisotropy

Isotropy (or anisotropy) is a measure of 3D symmetry or the presence (or absence) of preferential alignment of structures along a particular directional axis. A GDL volume contains two phases (void and solid) and has a complex architecture. If the volume is isotropic, then a line passing through the volume at any direction makes a similar number of intercepts through the solid phase. GDL could be anisotropic, since lines going along the direction of the fibres would make few intercepts along the fibres' rods while lines crossing at right-angles through the flow direction would make many intercepts. Mean intercept length (MIL) analysis is used to measure isotropy. It sends a line through the volume and divides the length of the line through the analyzed volume by the number intercepts. A huge number of the MIL lines are drawn passing through one point. In 3D, this creates a dense "pin-cushion" like effect with lines in all directions at different lengths. Anisotropy tensor analysis based on eigen analysis is needed to extract some summary numerical parameters defining the orientation and isotropy (or anisotropy) of the MIL distribution. The end result of the anisotropy tensor analysis is the eigen analysis and eigen meaning characteristic. The three eigen values are each an index of the relative length of solid intercepts in each of the three axes described by the eigenvectors. Finally, one can derive from the tensor eigen analysis a single parameter measuring anisotropy and is calculated as the minimum eigen value divided by the maximum eigen value. Degrees of anisotropy calculated in this way vary from 0 (fully isotropic) to 1 (fully anisotropic) [164].

3.3.1.5 Centroid and tortuousity

The tortuousity of a material reflects the convolution of the pathways within it relative to the movement of an infiltrating gas in free space. It is usually defined by the ratio of the length of the mean effective path through the pore space and the material thickness [165],[166],[167], As such, the tortuousity can be quantified by tracking the centroid of each pore (which is the mass centre of single phase flow) as it goes from one side of the layer to the other side. Then, tortuousity is the total length of this path divided by the thickness of the layer [139]. As the flow moves from the surface of the layer, the centroid of each pore can be corresponded to the centroid of each 2D slice image. The calculation of the centroid of the binary image is as follows:

Similar to the concept of moment of inertia, moment of a 2D binary image, *M*, of order (*i*+*j*) can be calculated as:

$$M_{ij} = \sum_x \sum_y x^i y^j I(x, y) \tag{3.1}$$

Where *x,y* are the horizontal and vertical position of a pixel with respect to a fixed origin and *I(x,y)* is the intensity of the pixel. In the case of a binary image, the intensity equals to 0 for the pores and 1 for the solid. The centroid of each binary slice could be obtained by the first order of moment given by equation (3.2):

$$Centroid: \{\bar{x}, \bar{y}\} = \{M_{10}/M_{00}, M_{01}/M_{00}\} \tag{3.2}$$

Then, tortuousity is the total length of the path of the centroid track divided by the thickness of the layer.

3.3.1.6 Effective diffusion coefficients and permeability

As discussed in section 2.3 of Chapter 2, the effective diffusion is obtained by:

$$D_{eff_{i,j}} = \frac{\varepsilon_G}{\tau_G} D_{i,j} \tag{3.3}$$

where effective diffusion coefficient ε_G/τ_G can be calculated by porosity and tortuousity obtained from tomography images.

Similarly, Knudsen diffusion dominates when the pores are small i.e. in the case of MPL and CL. The knudsen diffusion coefficient, D_K, is given by following equation:

$$D_K = \frac{2}{3} r_{p,mean} \sqrt{\frac{8RT}{\pi M_m}} \tag{3.4}$$

where $r_{p,mean}$, R, T and M_m are mean pore radius, gas constant, temperature in Kelvin and molar mass of air.

As discussed in Chapter 2, gas phase permeability, k_G, can be calculated through two analytical approaches: (i) Kozeny-Carman relation as equation (3.5) [168] and; (ii) Tomadakis-Sotirchos as equation (3.6) [169]:

$$k_G = \frac{{\varepsilon_B}^3 d_f^2}{16 k_K (1-\varepsilon_B)^2} \tag{3.5}$$

$$k_G = \frac{\varepsilon_B (\varepsilon_B - \varepsilon_p)^{(\alpha+2)} d_f^2}{32(\ln \varepsilon_B)^2 (1-\varepsilon_p)^{\alpha} [(\alpha+1)\varepsilon_B - \varepsilon_p]^2} \tag{3.6}$$

where k_K is the Kozeny constant and depends upon porosity. The literature reveals a wide range in the value of the Kozeny constant for carbon fibre materials in general ranging from 1.45 to 26.50, but in the region of 4.06 to 4.54 for typical commercial materials based on carbon fibre [170].

Equation (3.6) is independent to the fitting parameters compared to the Kozeny-Carman relation; therefore it is more convenient for fuel cell permeable material modelling.

3.3.2 Calculation of permeability and tortuousity through LB approach

The LB method is a numerical model based on kinetic theory to simulate fluid dynamics [71],[72]. The concept of the LB method was introduced by McNamara and Zanetti to develop its predecessor, the lattice gas algorithm [73],[74]. Unlike conventional CFD, the LB method tracks the streaming and collision of a collection of pseudo-particles in a lattice which interact according to a velocity distribution function. As an example, the single-time relaxation LB model [75] is based on the movement of a fictitious particle described in terms of the particle distribution function, $f_i(x,t)$, (mass of a particle at location x at time t) and moving with velocity, ξ_i, in the direction i:

$$\frac{\partial f_i(x,t)}{\partial t} + \xi_i \cdot \nabla f_i(x,t) = \frac{1}{\lambda}\left[f_i^{eq}(x,t) - f_i(x,t) \right] \tag{3.7}$$

where $f_i^{eq}(x,t)$ is the equilibrium distribution function which is the value of $f_i(x,t)$ under an equilibrium state and λ is a relational parameter which controls the rate at which $f_i(x,t)$ approaches $f_i^{eq}(x,t)$. Solving equation (3.7) by the finite difference method gives:

$$f_i(x+\xi_i\delta t, t+\delta t) = f_i(x,t) + \frac{1}{\tau_r}\left[f_i^{eq}(x,t) - f_i(x,t) \right] \tag{3.8}$$

where δt is the time step and $\tau_r = \delta t/\lambda$ is a dimensionless relaxation time parameter. Therefore, a particle with velocity ξ_i at location x and time t will redistribute to $x+\xi_i\delta t$ at time $t+\delta t$ after colliding with other particles at location x moving with dissimilar velocities. The number of dissimilar velocities in the LB model depends upon the 3D scheme employed.

The LB model considers the particle distribution functions at each voxel in turn and determines a set of nineteen velocities in the 3D spatial domain for the node of each voxel as shown in Figure 3.4. The nineteen velocities considered are as follows: stagnation at the origin *(0,0,0)/ δt*; two velocities in the *x* direction *(± δx,0,0)/ δt*; two in the y direction *(0,± δx,0)/ δt*; four in the *x-y* plane *(± δx,± δx,0)/ δt*; four in the *y-z* plane *(±δx,0,±δx)/ δt* and four in the *y-z* plane *(0,± δx,± δx)/ δt*. This scheme is commonly known as the D3Q19 scheme.

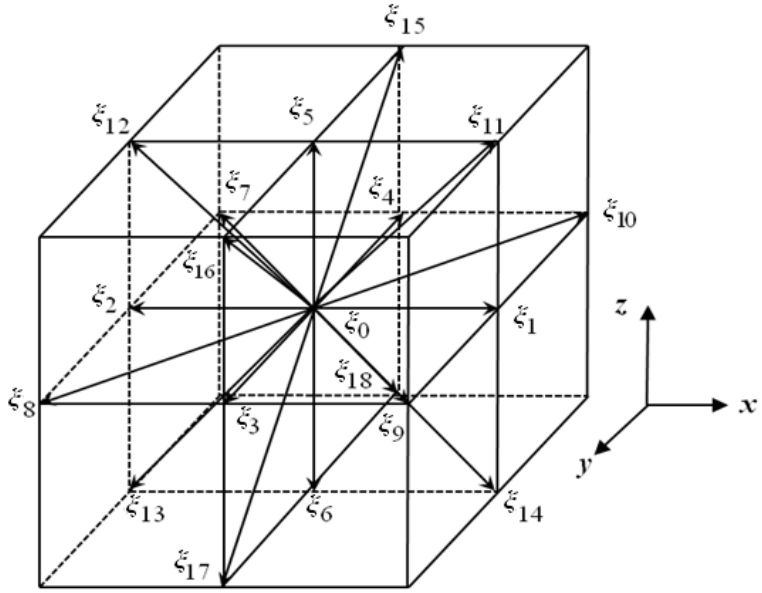

Figure 3.4. The 19 directions along which the particles in each void voxel move

The single phase model assumes that the pores are infiltrated by air. Using the detailed velocity field, it is possible to calculate the three components of the permeability tensor for the imaged sample using Darcy's law:

$$k_{xx} = \frac{\rho\mu q_x}{(\Delta P / L_x)}; k_{xy} = \frac{\rho\mu q_y}{(\Delta P / L_x)}; k_{xz} = \frac{\rho\mu q_z}{(\Delta P / L_x)} \tag{3.9}$$

where ρ *i*s the density of air, μ is the kinetic viscosity of air, q_i is the average velocity in the direction i, ΔP is the pressure applied in the principal flow direction and L_i is the overall sample length in the direction i. The average velocity q_i is directly related to the velocity field and are obtained by:

$$q_x = \frac{\sum_i u_x(x_i)}{L_x L_y L_z}; q_y = \frac{\sum_i u_y(x_i)}{L_x L_y L_z}; q_z = \frac{\sum_i u_z(x_i)}{L_x L_y L_z} \tag{3.10}$$

where $u_x(x_i); u_y(x_i); u_z(x_i)$ are the three simulated velocity components for each element of the image. Once the absolute permeability is known, the permeability for each specific gas with density ρ_j and kinetic viscosity μ_j can be calculated from

$$k_j = \frac{k}{\rho_j \mu_j} \tag{3.11}$$

All the variables in equations (3.10) and (3.11) are measured in a spatial unit δx and a temporal unit δt. Applying the pressure difference to other two directions allows the other components of the permeability tensor to be calculated.

In the LB model, a pressure difference is applied to two opposite sides of the image along the through-plane direction to drive gas flow. The other four sides at in-plane directions are treated as non-mirrored periodic boundaries, in which two opposite sides are neighboured such that particles moving out of the domain from one side re-enter the domain through its opposite side. All the simulations start from a zero velocity field and the pressure field is linearly distributed in the direction along which the pressure difference is imposed. Steady state conditions are judged using the parameter Ω where

$$\Omega = \frac{\sum_i \left| u_j(x_i, t+100) - u_j(x_j, t) \right|}{\sum_i \left| u_j(x_i, t) \right|} \tag{3.12}$$

Flow is assumed to have reached steady state when the tolerance Ω less than 10^{-5} is satisfied.

The LB technique can be applied to determine the tortuousity. It is fundamentally the same as that applied to calculate permeability described above but simplified to consider seven velocities in three dimensions (D3Q7). In addition, the equilibrium distribution function $f_i(x,t)$ for fictitious particles moving with through the lattice can be defined as:

$$f_i^{eq}(x,t) = c/7 \tag{3.13}$$

where 7 represents the number of directions (including the stagnant particles) along which the particles move and c is the gas concentration, calculated by:

$$c = \sum_{i=0}^{6} f_i(x,t) \tag{3.14}$$

where $i=0$ represents the stagnant particles and $i=1\text{-}6$ represents the mobile particles. The free diffusion coefficient of gas movement in the void space is given by:.

$$D_0 = 2\delta x^2(\tau_r - 0.5)/7\delta t \tag{3.15}$$

where τ_r is a dimensionless parameter that controls the rate of $f_i(x,t)$ approaching $f_i^{eq}(x,t)$. The diffusive gas flux J, in each void voxel is calculated by:

$$J = (1 - 1/2\tau_r)\sum_{i=1}^{6} \xi_i f_i \tag{3.16}$$

Two different gas concentrations can be applied to the two opposing faces of the structure, which in return drives a diffusive flow through the simulated structure. The remaining four faces of the 3D image can be treated as periodic boundaries, in an identical manner to that described for the permeability analysis [171]. The void-solid interface is assumed to be impermeable to the gas. After the gas flow is deemed to have reached steady state, the

effective diffusion coefficients of the gas in direction *i* along which the gas concentration gradient was applied can be estimated as:

$$D_{ii} = \frac{L}{N_{tot}\Delta c}\sum_{n=1}^{N} J_{i,n} \tag{3.17}$$

where N_{tot} is the total number of the void voxels in the image, Δc is the concentration difference applied to the two opposite faces, L is the distance between the two faces, and $J_{i,n}$ is the flux in the i direction at voxel n when the concentration gradient is applied in the i direction. With the effective diffusion coefficient of gas flow in the structure and the free diffusion coefficient known, the tortuousity of the porous network along the direction i is calculated by

$$\tau_i = D_0 / D_{ii} \tag{3.18}$$

Hence, by combining the full 3D morphological reconstruction of the structure with LB numerical flow simulation, the resulting calculation of tortuousity based on diffusion will directly reveal the convolution of pathways within the porous structure in all three dimensions.

In section 3.2 it was recognized that thresholding is a crucial step in producing accurate 3D binary images. Therefore in the next sections current techniques for binarisation of tomography images are described and then novel methods to finely tune the threshold are presented.

3.4 THRESHOLDING TECHNIQUES FOR BINARISATION OF X-RAY μCT/NCT IMAGES

One of the crucial steps in the X-ray tomography based digital reconstruction process is thresholding, in which structures are evaluated in voxels with gray level values and segmented to distinguish solids from pores using a threshold value.

At present, a threshold is often determined visually or by the common Otsu algorithm [155],[159]. The Otsu algorithm steps are as follows: (i) every possible threshold for the image is applied and the pixels are subdivided into two categories of object pixels and background pixels in each thresholded image; (ii) the spread of the pixel levels on both sides of the threshold are calculated. The optimum threshold is the one in which the sum of the object and background pixel spreads is minimum (Figure 3.5). However, it has been shown that the Otsu algorithm cannot be always reliable and it is computationally expensive when dealing with hundreds of images [160]. On the other hand, selection of threshold can have a significant effect on the volume fractions, pore sizes, average object/pore size, morphological parameters and mechanical properties of various structures [122],[126],[172],[173]. As such, further research is needed to improve the understanding of how optimal threshold levels can be determined to enhance the accuracy and practical applicability of X-ray tomography based structural modelling and porous flow simulation.

In the following two sections, new threshold methods are proposed for woven and non-woven GDL for binarisation.

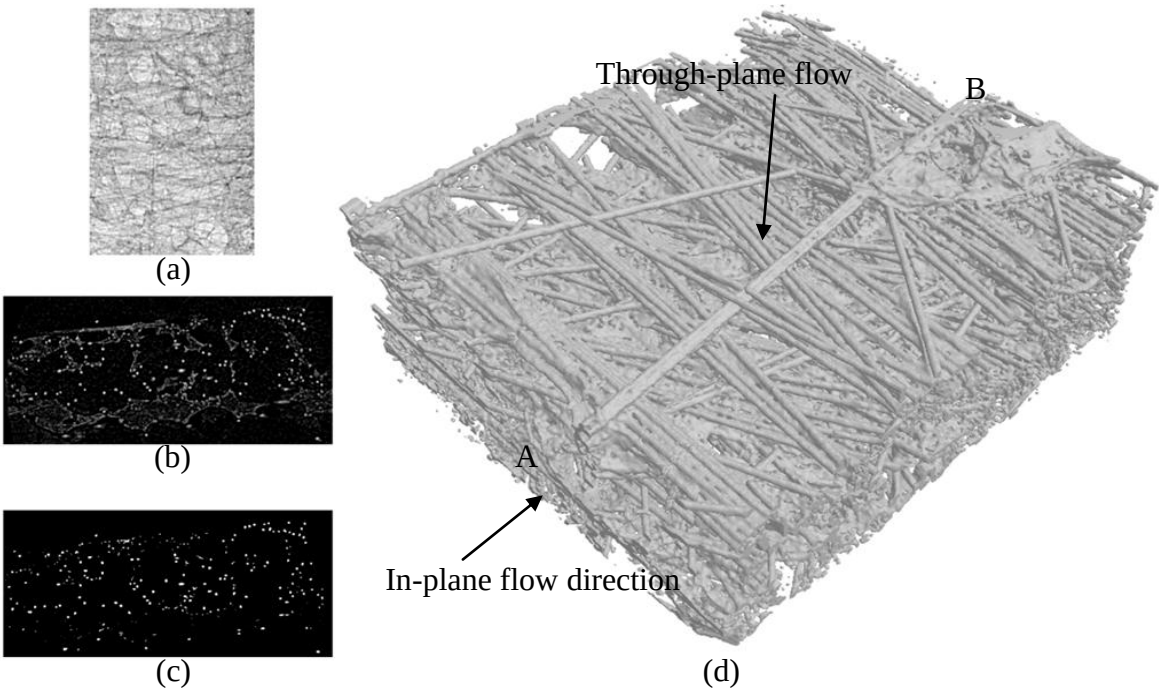

Figure 3.5. 2D and 3D images of a GDL carbon paper sample. The images have been taken through SkyScan 2011 nCT scanner and thresholded through the Otsu method.; (a) A shadow x-ray tomography image; (b) A 2D reconstructed greyscale slice image ; (c) A binary image of the cross section shown in figure 1b based on Otsu's algorithm. A simple Matlab code was developed and a few slices were randomly chosen and thresholded based on the Otsu algorithm. The threshold value was then applied to the whole stack of slices for 3D reconstruction using CTAN and ; (d) An isometric view of the reconstructed image of a GDL sample with a 680 nm pixel size using CTAN.

3.5 THRESHOLD METHOD FOR NON-WOVEN GDL IMAGES

In this section a new method for fine-tuning the threshold of tomography images for a non-woven GDL. First, the influence of small threshold variations on determining the properties of the GDL is discussed. Then porosity and average fibre diameter of the GDL, obtained from a series of thresholded X-ray images were compared to reference values of porosity and average fibre diameter achieved from a density experiment and SEM images respectively. Between the thresholded images, the optimal threshold was chosen, in which

the porosity and average fibre diameter of the resultant digital model are closest to the reference values.

3.5.1 Influence of threshold variation on properties of non-woven GDL

In this investigation, a 1×1×0.3 mm^3 carbon paper GDL HP_30_35 sample supplied from Technical Fibre Products is scanned in front of an X-ray source of SkyScan 2011 with 25 kV, 200 µA without filter, 2 sec exposure time, 3 frames in average and a rotation step of 0.5 degrees. 371 shadow images with 680 nm pixel size are acquired within 40 minutes. The shadow images are then processed using modified Feldkamp filtered back projection method to reconstruct the 2D greyscale slices.

For the investigation of threshold variation, a threshold value (obtained from Otsu's algorithm applied to a randomly chosen slice) is selected for processing greyscale images and creating binary images. This threshold value is taken as a reference for a starting point. Then, 12 more threshold values in increments of 1 greyscale, i.e. 0.4% of the total greyscale value, are used as test threshold values and the binary images are generated. The variation of porosity, degree of anisotropy, average pore radius, diffusion, and permeability parameters over threshold variation are studied.

The first important parameter that can be calculated directly from a reconstructed model is porosity as described in section 3.3.1.1. Figure 3.6 shows that the porosity of the full area of the tomography image changes linearly over the threshold values of the thirteen samples.

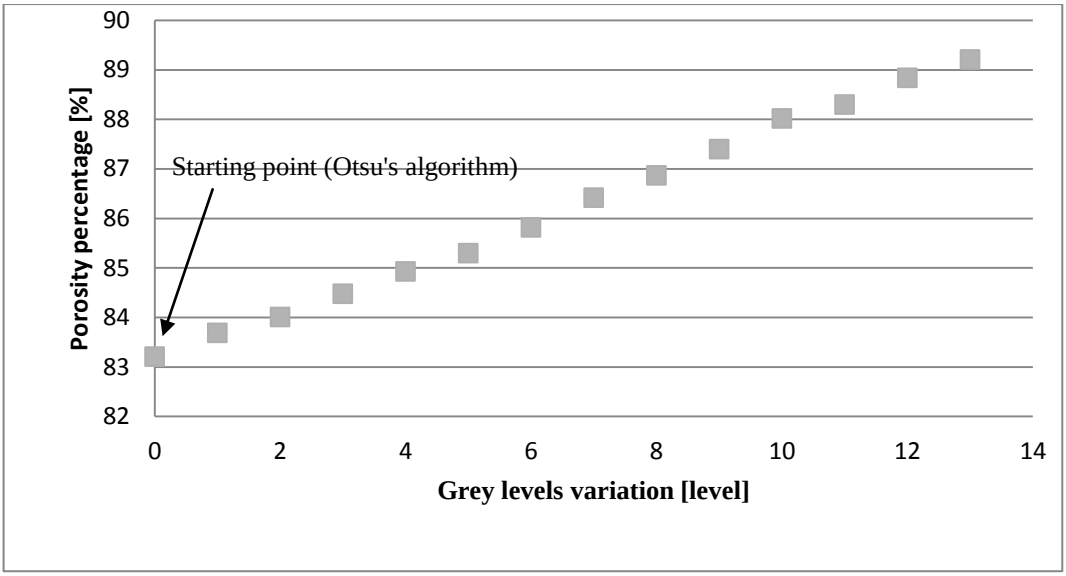

Figure 3.6. Influence of threshold variation on porosity of the non-woven GDL sample.

As discussed in section 3.3, degree of anisotropy is a key parameter in the GDL material characterization. Since the calculation of the degree of anisotropy is time consuming, a cubic sample of 300 µm on each side, which is equal to the thickness of the carbon paper, was selected for calculations. Dimensionless degrees of anisotropy of the sample over the threshold variation is summarised in Figure 3.7 for both pore and solid networks. It can be seen that threshold variation has a negligible effect on the degree of anisotropy for both solid and pore network in the GDL. A 5% variation in threshold results in a 2% change in the degree of anisotropy.

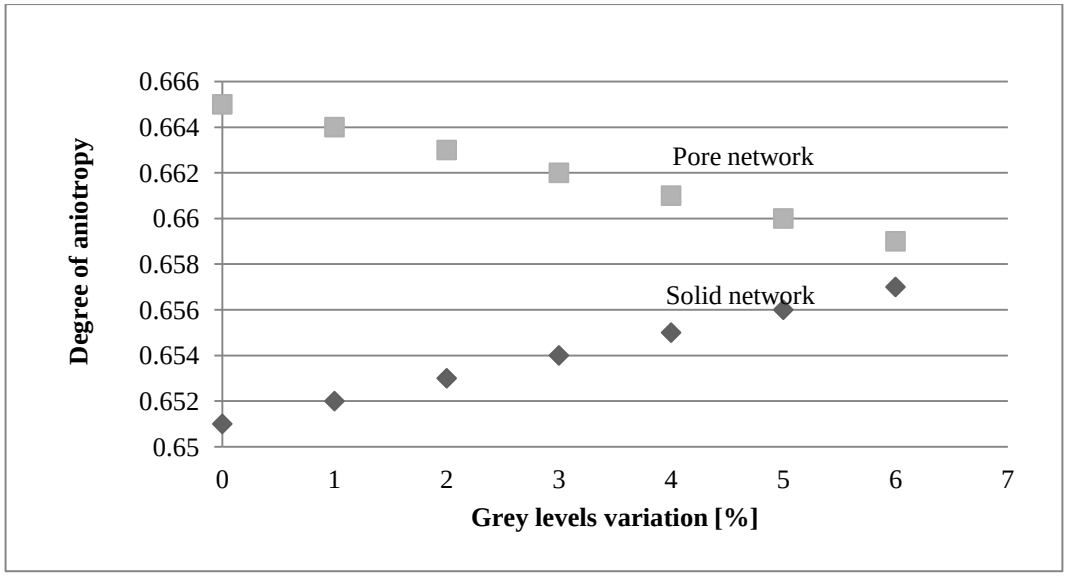

Figure 3.7. Degrees of anisotropy of both pore and solid network over threshold values

The average pore size of the samples measuring the full reconstructed area was calculated and was found to change with the threshold value by 0.5 and the average pore radius changed from 13.5 µm to 16 µm over a 5% threshold variation span linearly as shown in Figure 3.8. This means that Knudsen diffusion changes about 20% over only 5% of threshold variation.

The variation in threshold results in 10% fluctuation in the fibre diameter of the nCT image of the GDL sample. This could be because the fibres which are packed very closely together could be separated by only a slight variation in threshold, which can change the average diameter accordingly as shown in Figure 3.9.

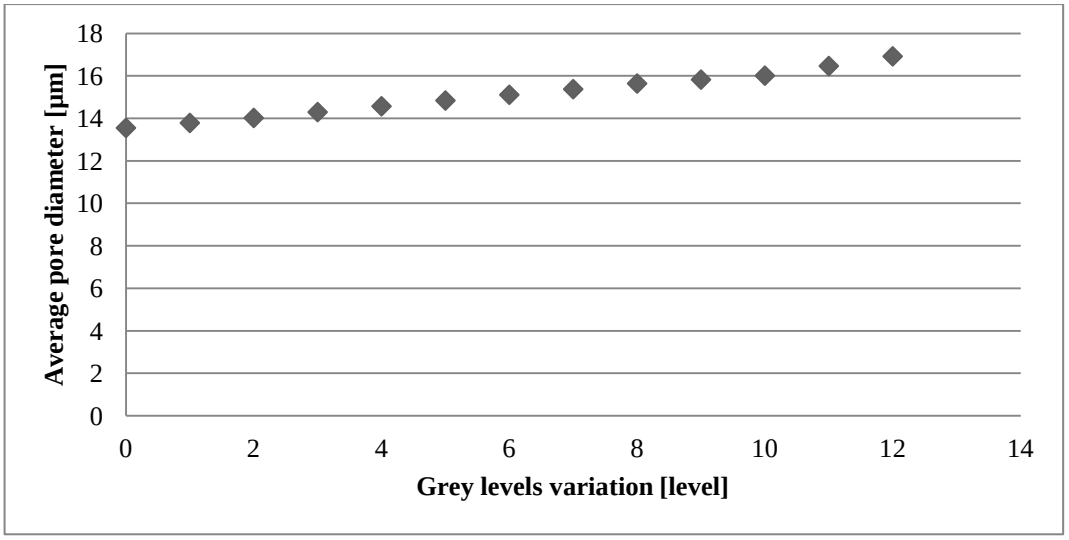

Figure 3.8. The relationship between average pore radius of the GDL and threshold value.

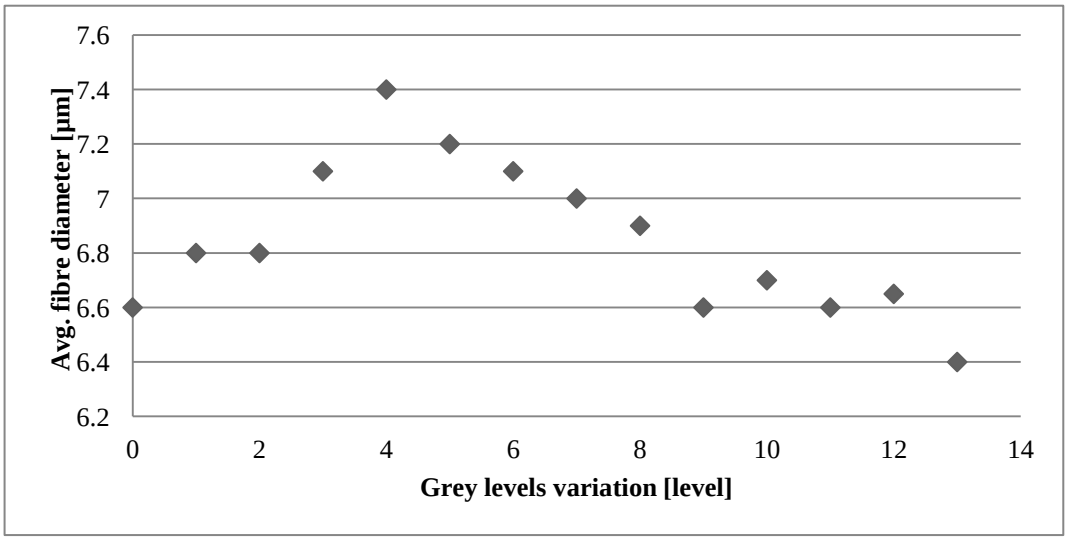

Figure 3.9. Variation of fibre diameter and porosity over 5% threshold alteration. 13 grey levels represent 5% of threshold variation. Average fibre diameter over threshold is fluctuating for GDL.

For permeability, the 3D reconstructed model of the GDL is stored in a 3D binary array and uploaded to the LB model described in section 3.3 for flow simulation. In general modelling terms, the spatial resolution of the LB model has to match the pixel size of the 3D image. In the current study the GDL has a porosity of greater than 80% which thereby eases the computational demand of the LB flow simulation. This therefore allows each voxel of the 3D binary image to be used directly as the lattices of the LB model. In this case, the spatial resolution of the LB model is set equal to the pixel size of the X-ray images. The LB solver is applied to differently thresholded samples of 100×300×100 μm^3 flowing along 300 μm length direction to simulate the detailed gas velocity field in the void space of the GDL, with the assumption that the void spaces are filled with air. The simulated velocity is then used to obtain the absolute permeability for the region. As the absolute permeability represents the linear dependence of gas flow rate on pressure gradient, it must be ensured that the flow rate in the simulations is also in this linear range. As such, the pressure difference applied to each region is set to 20 Pa.

The simulation was carried out on a dual-core 2.01 GHz workstation with 3.25 GB of RAM. A single-phase simulation for the region takes 500 minutes. Figure 3.10 demonstrates that the through plane permeability is a strong function of threshold variation.

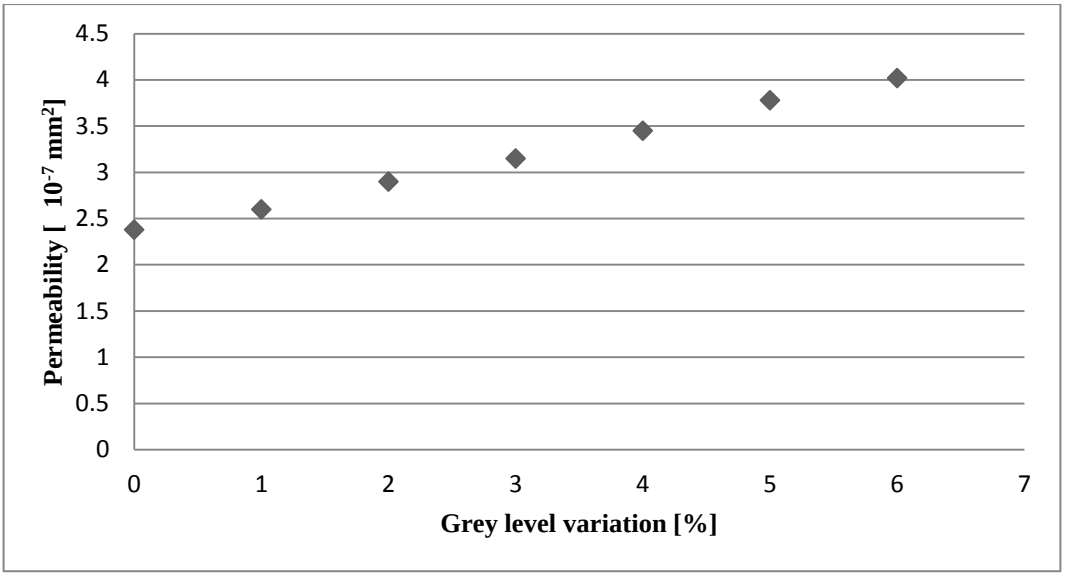

Figure 3.10. Through plane permeability sensitivity over threshold variation. With only ~5% variation of threshold the permeability is almost doubled from 2.38×10^{-7} mm^2 to 4.02×10^{-7} mm^2.

In this section, the influence of a small threshold variation on mechanical and fluidic flow properties of a non-woven GDL layer was studied. The results show that porosity increases linearly with a lower threshold. The linearity implies that the GDL structure is quite homogeneous in terms of material density distribution. The sensitivity of the degree of anisotropy for the solid/pore network to a 5% threshold variation is only about 2%. The analysis on average pore diameter finds that it changed from 13.5 µm to 16.9 µm and has an influence of 20% on Knudsen diffusion of the GDL. Hence, diffusion is a parameter sensitive to threshold. The variation in threshold results in 10% fluctuation in the fibre diameter of the nCT image of the GDL sample. Permeability is found very sensitive to the threshold and changes about 80% with only 5% threshold variation, since increasing the porosity helps fluidic flow in the pore network.

The next section is focused on precisely identifying the correct threshold level.

3.5.2 Fine tuning of threshold

This section proposes a method for fine-tuning the threshold of nanotomography images for porous media. Porosity and average fibre diameter of a GDL obtained from a series of thresholded images as shown in Figure 3.6 and Figure 3.9 were compared to reference values.

Reference values were considered to be porosity and average fibre diameter which can be achieved easily and accurately from density experiments and SEM images respectively. Therefore, between the thresholded images, the optimal threshold was chosen in which the porosity and average fibre diameter of the resultant digital model are closest to the reference values.

SEM can provide high-contrast and high-resolution greyscale images of the surface of the imaged sample and therefore allows the features of the carbon fibrils of the GDL to be determined. Four SEM images from the corners of a 5×5 mm^2 GDL and another from the centre were taken. The average fibre diameter in each binary SEM image was calculated using CTAN software. The average diameter obtained was 7.00±0.05 μm. Figure 3.11 shows an SEM image of the sample centre.

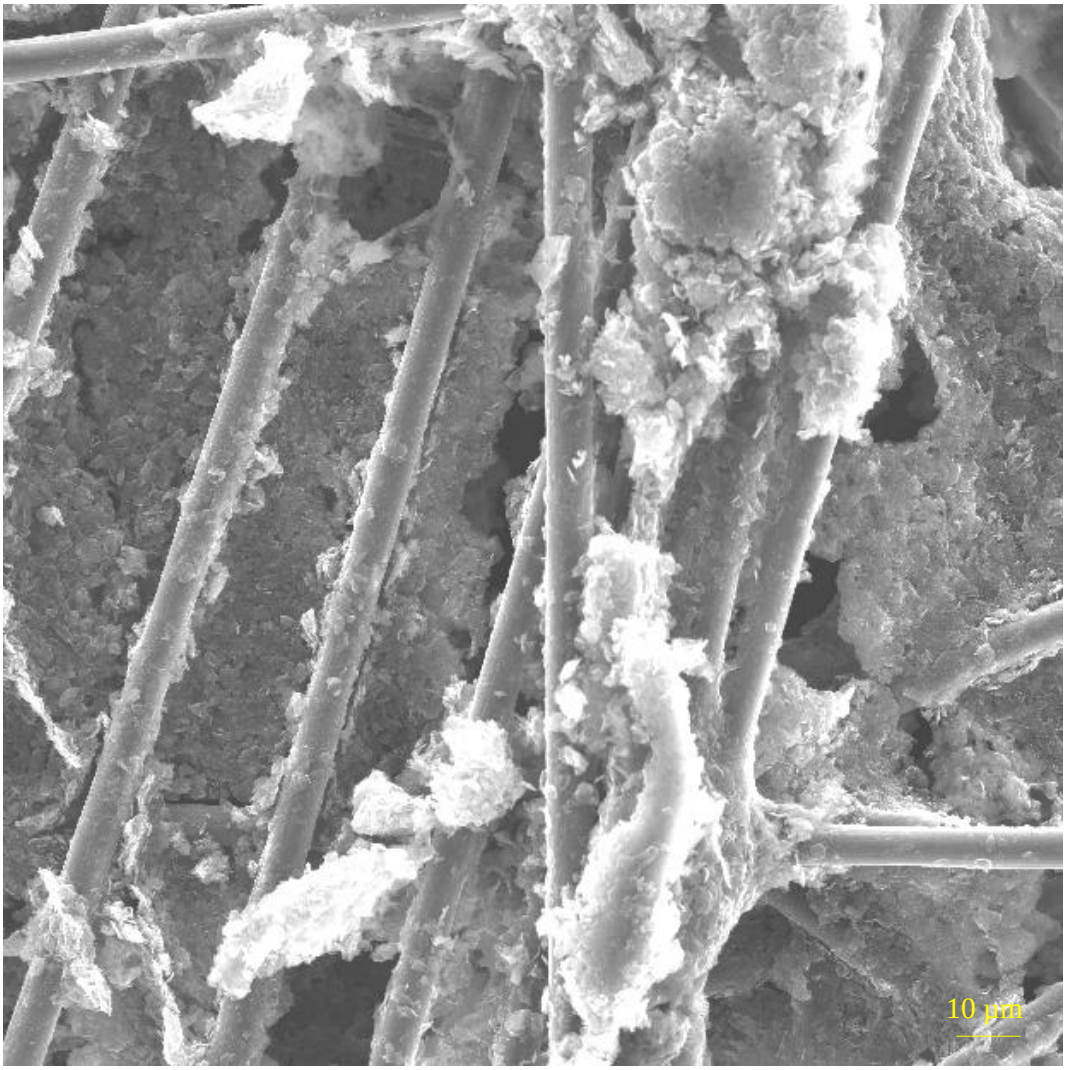

Figure 3.11. SEM image of the surface of the GDL sample.

The porosity of a material can be calculated using grammage (basis weight) and the thickness of the GDL. The solid fraction of the material was worked out based on the density of the GDL and then porosities were determined as 84±1%. Therefore those threshold values which give porosities out of 84±1% and 81±1% can be withdrawn. The average fibre diameter of the remaining threshold levels from the nanotomography images are given in Table 3.1.

Table 3.1 Average fibre diameter of the remaining threshold values, reference value of fibre diameter, porosity results from nanotomography and reference value of porosity for the GDL carbon paper.

Number	Average fibre diameter (μm)	Reference value of fibre diameter (μm)	Porosity (%)	Reference value of porosity
1	7.2	7.00±0.05	83.0%	84±1%
2	7.4	7.00±0.05	83.3%	84±1%
3	7.2	7.00±0.05	84.4%	84±1%
4	7.1	7.00±0.05	84.9%	84±1%

The tomography threshold cannot be tuned with regard to porosity only. In this experiment, there are several values of porosities close to the reference values of 84±1% & 81±1% summarised in Table 3.1. Each of the calculations represents different threshold levels.

In Table 3.1, number 2 can easily be removed because the calculated fibre diameter is higher than the others. Between 1, 3 and 4 the priority of choosing the optimal threshold is given to the fibre diameter since the experiment of fibre diameter average measurement was based on high resolution SEM images and therefore it is more accurate than the density experiment. This leaves number 4 as the optimal threshold.

The fine-tuning process established above, based on the conservation of fibre diameter and porosity, therefore results in 84.9% of porosity and 7.1 μm in average fibre diameter for carbon paper. The 3D binary image of carbon paper using optimal threshold values is shown Figure 3.12.

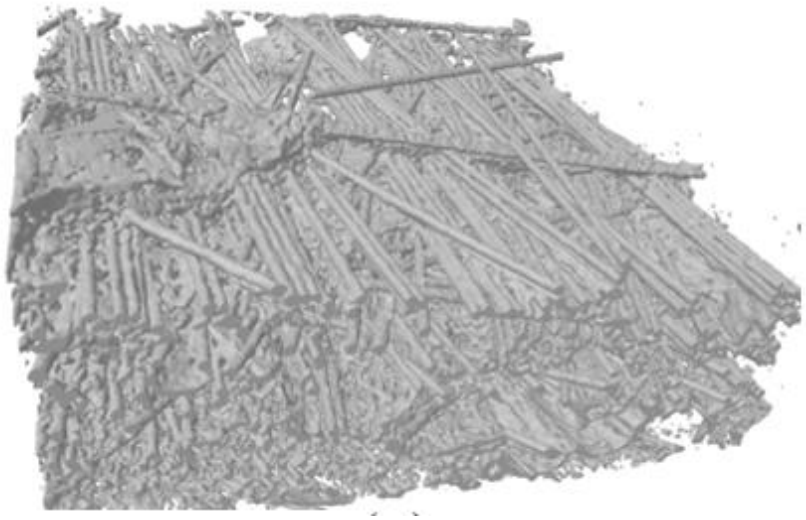

Figure 3.12. An isometric view of the reconstructed image of GDL carbon paper sample with 680 nm pixel size using CTAN.

The method discussed above is not applicable for a woven material. It is not reliable to measure the porosity of the sample through the thickness of the sample since the surface of the sample is not flat and the thickness varies from point to point. Therefore, in the next section, the porosity is not taken as a reference. Instead, continuity in the material is investigated.

3.6 THRESHOLD METHOD FOR A WOVEN GDL

This section investigates the effect of threshold variation on the properties of a reconstructed woven GDL layer and provides a method to find an optimized threshold value.

To understand the effect of threshold variation on the properties of reconstructed porous woven material, GDL samples of 5-10 µm filament size have been scanned in SkyScan 1072 with a different pixel size of 1.76 µm.

A GDL SCCG-5N sample was scanned in front of an X-ray source of SkyScan 1072 with 50 kV, 100 µA without filter, 2 sec exposure time, 3 frames in average and a rotation step of 0.9 degrees. 207 shadow images with 1.76 µm pixel size were acquired within 55 minutes.

A set of 2D greyscale image slices were produced in 256 grey scales and Otsu's thresholding algorithm was applied to a randomly chosen 2D slice. Then, the obtained value from Otsu method was applied to the whole set of 2D image slices and taken to be the starting point for threshold variation. Next, the set of 2D greyscale slices were thresholded again in 12 grey levels with a step of 0.4% variation around the starting point, such that each step associates to 1 grey level (5% threshold variation in total). This process results in thirteen sets of thresolded 2D image slices.

A typical shadow woven GDL image from an X-ray scanning is shown in Figure 3.13a, while a typical reconstructed slice is shown in Figure 3.13b. Figure 3.14 shows the effect of a 5% change in the threshold on the discontinuity of fibres from an X-ray µCT. For instance, the small blue circles in Figure 3.14a and b show the effect of a 5% threshold variation in continuity of the material. Threshold values lower than Otsu's starting point obviously resulted in more discontinuity in this case, therefore for investigation of threshold variation, the 5% threshold towards the higher threshold were applied.

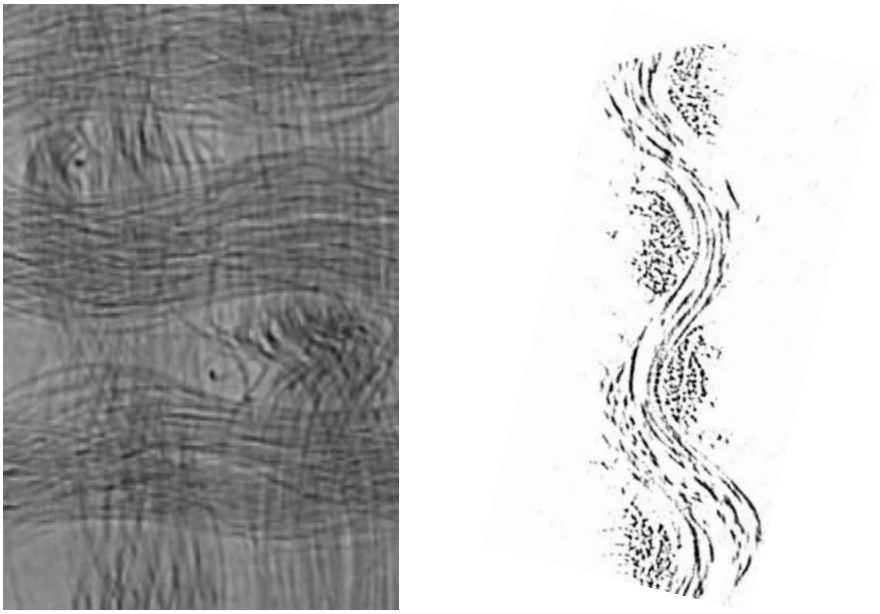

(a) (b)

Figure 3.13. a) A typical shadow image of X-ray µCT; b) A reconstructed cross section image using CTAN software with µCT.

(a) (b)

Figure 3.14. Threshold variation as small as 5% makes a significant effect on fibre's continuity. The blue circles are examples of discontinuity; a) low threshold based on Otsu's method and; b) is high threshold.

In comparing the two images in Figure 3.14, one should pay attention to the average fibre diameters. Many measurements were carried out using CTAN, for identifying the relationship between the 5% thresholds variation and average fibre diameter. Figure 3.15 shows that by increasing the threshold value, how average fibre size increases.

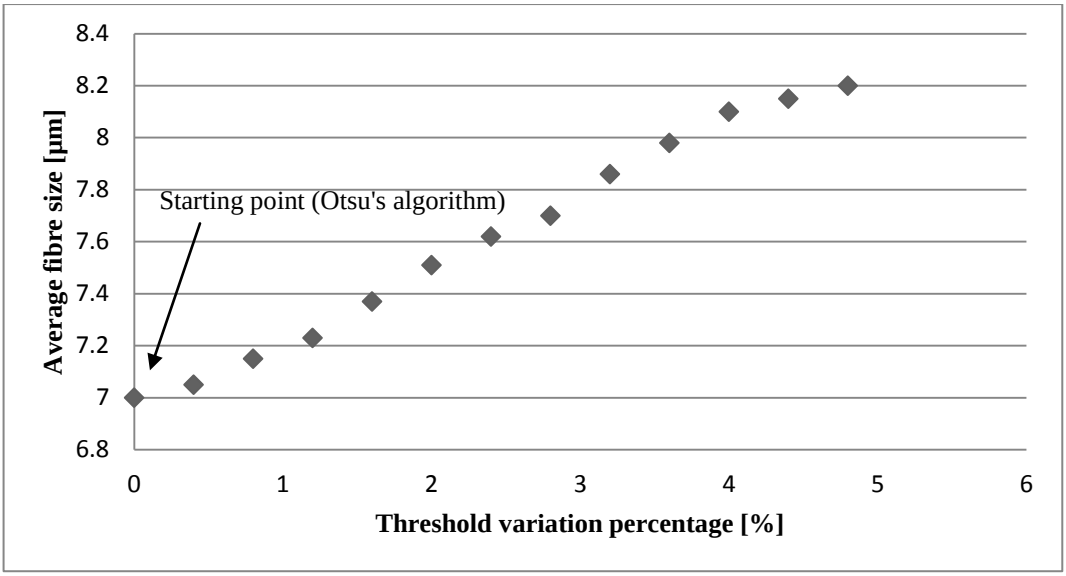

Figure 3.15. Average fibre diameter in µm over threshold variation obtained from X-ray µCT.

Figure 3.15 illustrates that there is a linear relationship between fibre diameter and threshold variation. Higher threshold increases the continuity of the sample as well as the fibres' diameters. Also, the effect of 5% threshold on the porosity, analytical permeability, equation (3.6), tortuousity, equation (2.5), and effective diffusivity, equation (3.3), of the sample based on µCT results were found to be around 10%, 10%, 3% and 2% respectively.

Now the key is to identify the correct threshold. In the next section an SEM image of the surface of the same GDL sample will help to find an optimum threshold value.

3.6.1 Fine tuning of threshold

A projected image of the surface of the 3D reconstructed model is like an SEM image of that of surface. Comparison between a µCT image and SEM images in continuity and fibre diameter is helpful for threshold estimation. A binary SEM image should be taken as a reference in order to have a meaningful comparison. Figure 3.16 shows a grey scale SEM image of a fabric and its binary image. Generating a binary image from an SEM result

requires a threshold. In doing so, the binary image can be compared with the grey scale image in terms of continuity and fibre diameter.

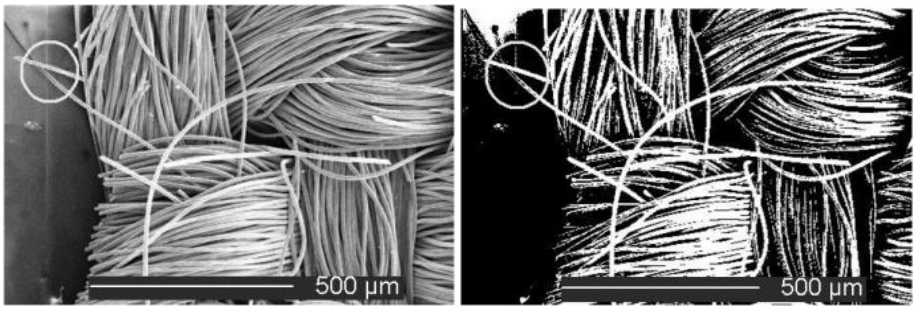

(a) (b)

Figure 3.16. An SEM image of woven GDL sample. The region of interest is shown inside a white circle; b) A binary image of Figure 3.16a.

SEM images are of high resolution and high contrast and a 5% threshold variation does not make a significant difference. As it is clear in the region of interest in Figure 3.16, the continuity of the fibres are the same which confirms that the Otsu's recommended threshold is fine for this region. The average fibre diameter at the region of interest in Figure 3.16 and the whole image was found to be 8.05±0.1 µm and 7.80±0.1 µm respectively.

An X-ray µCT scan of the same part of the GDL layer was carried out and a 3D model was reconstructed. It should be mentioned that, threshold variation in this case is discontinuous. The minimum step of the variation is 0.4% which corresponds to 1 grey level. By using Figure 3.15, the average fibre size with threshold variation can be predicted. A series of reconstructions for various thresholds (between 0% and 5% with step of 0.4%) was carried out and the continuity of the featured shape was examined. In this experiment, only the highest threshold showed continuity in the material. Figure 3.17. shows the two thresholds (highest and lowest) and reconstruction of the area in the circle in Figure 3.16a. There are

two featured fibres with a cross (×) shape highlighted with yellow colour. This could be seen in the both images of Figure 3.17 and the SEM image in Figure 3.16.

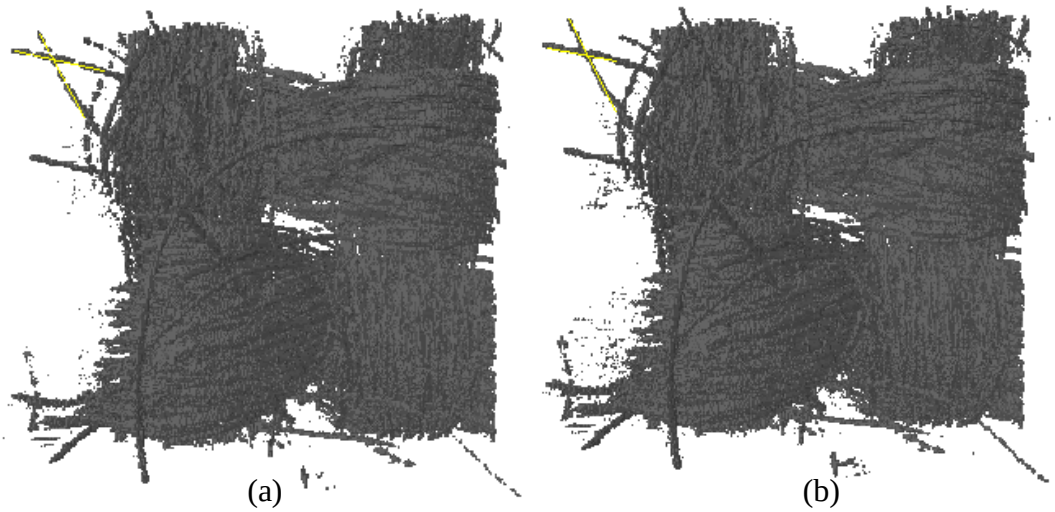

Figure 3.17. A reconstructed image from the X-ray µCT with two estimated thresholds. Average fibre size in (b) is higher than (a) and closer to the reality.

The resulting average fibre diameter from the µCT when the highest threshold value is applied is 8.2 µm and the cross (×) shape average fibre diameter is 8.3 µm, which are 5% and 3% less than the values of 7.80 µm and 8.05 µm obtained from the SEM image.

The influence of threshold variation on the woven material properties based on µCT was discussed and a method to tune the threshold based on continuity of the material was described. In the next section, this Chapter is summarised.

3.7 SUMMARY

This Chapter explains the process of X-ray µCT/nCT. Particular interest is placed in proposing a novel thresholding method, which enables us to determine the key parameters of the GDL samples more accurately. For this purpose, the X-ray µCT/nCT methods were well understood and fundamental parameters of X-ray for optimum image conditions were recognized. The X-ray energy for µCT and nCT was set to be 50 kV/100 µA and 25 kV/200 µA respectively. Also, it was revealed that how the key parameters can be calculated through X-ray µCT/nCT images. Parameters including porosity, pore size distribution, characteristic lengths, mean pore radius and degree of anisotropy were explained and calculated. Effective diffusion coefficient, Knudsen diffusion, tortuousity and permeability were analytically calculated based on the parameters obtained from the 3D images. LB modelling to calculate permeability and tortuousity was also explained.

It has been proven that when a study is carried out using X-ray µCT/nCT data for porous non-woven GDL, the key structural parameters are affected by small variations in threshold. It is found that a variation of more than 5% in threshold makes a significant visual difference to the resultant binary images. While a variation of less than 5% is difficult to be recognized visually, it can have a significant effect on the overall structural properties of 3D binary image. Therefore, having some easily measurable references will greatly assist in finely tuning the threshold for the 3D binary representative image. Reference values were considered to be porosity and average fibre diameter which can be achieved from density experiments and SEM images respectively. Therefore, between the thresholded images, the optimal threshold was chosen in which the porosity and average fibre diameter of the resultant digital model are closest to the reference values.

For the woven GDL, a small range of 5% in threshold variation shows an influence of about 10% in fibres size. In order to overcome such modelling problems two parameters have been identified: (i) average fibre diameter and; (ii) continuity of the fibres. A high resolution binary SEM image of a particular feature was used to compare the average fibre diameter and continuity. Then by using the 3D reconstructed surface from μCT and comparing the continuity and average fibre diameter with the SEM image, finely tuned threshold value was found. This method is relatively fast and more trustable, rather than the common visual threshold tuning or Otsu's algorithm without any pre-knowledge in the micro/nanostructure.

In the following Chapter, a number of samples including woven, non-woven and compressed GDL samples are characterised and the threshold method is used wherever is applicable.

4 CHAPTER 4: X-RAY µCT/NCT FOR CHARACTERISATION OF UNCOMPRESSED AND COMPRESSED GDL

4.1 INTRODUCTION

X-ray µCT and nCT are applied to characterisation of a number of uncompressed and compressed GDL in this Chapter. In section 4.2, a brief review of previous work on GDL characterisation using X-ray tomography data and the effect of compression on the porous layer structure are presented. Then in section 4.3, several woven and non-woven samples are imaged through X-ray µCT/nCT and their key parameters are obtained. Key parameters including porosity, average fibre diameter, pore size distribution, degree of anisotropy and tortuousity, are calculated directly from the 3D digital images. Effective diffusion coefficient and permeability are analytically obtained. For permeability, LB simulation and analytical results are validated against experimental permeability tests. In section 4.4, the structural features of compressed GDL samples under different compressions are captured by using a novel technique. PDMS material is used to encapsulate the compressed porous structure and subsequently X-ray µCT is employed to reconstruct digital three dimensional models and the effect of compression on the structure of the porous material is revealed. Finally this Chapter is summarised in section 4.5.

4.2 A BRIEF REVIEW OF GDL CHARACTERISATION AND EFFECT OF COMPRESSION

This section briefly explains previous work carried out for uncompressed GDL characterisation through tomography techniques. Then the effects of compression on the GDL are studied.

4.2.1 GDL characterisation through X-ray µCT/nCT

Recently, X-ray micro-tomography [146] has been used to quantify liquid water saturation in the GDL and in determining two-phase material parameters with 10 µm resolution. However, the results suggest that the technique requires much more development and better resolution for application to fuel cells [142].

Fishman et al [169], applied the Tomadakis and Sotirchos transport model to heterogeneous porosity distributions obtained from GDL tomography images with a resolution of 2.4 µm. The corresponding distribution of tortuousity, diffusivity and single phase permeability were calculated.

Pfrang et al [174], calculated the thermal conductivity of the GDL by solving the energy equation considering a pure conduction problem based on X-ray tomography data with resolution of 700-800 nm. Results shows there is a clear dependence of thermal conductivity on the porosity and the orientation of the fibres.

Finally, X-ray nano-tomography with a spatial resolution of 700 nm has been successfully employed to determine the permeability and diffusivity of the GDL layer as a function of the saturation of the layer [70].

Along with the key information obtained from uncompressed GDL characterisation, it is crucial to characterise compressed GDL. In order to minimise reactant leaks from the edge

of a cell and to reduce the interfacial contact resistance between surfaces, it is necessary to compress a PEFC stack under high compressive loads. The compression can change the compactness of carbon fibres in the GDL and can therefore affect the connectivity of pathways for gas transport. Another purpose of this Chapter is to capture the physical effect of compression on the porous structure of GDL and to determine the impact on gas transport parameters.

4.2.2 Effect of compression on GDL

The effects of GDL compression on the performance of the PEFC have been investigated in the literature. Lee et al, investigated the effect of bolt torque on cell performance for a range of commercially available GDL from 203 to 508 µm in thickness [175]. Their results showed that the internal pressure increased with GDL thickness for a given bolt torque. Cells configured with the thinnest GDL and thickest GDL experienced internal pressures between 1.6-2.1 MPa and between 8.4-9.7 MPa respectively.

Ge et al, identified the existence of a threshold level of compression which results in optimal cell performance for woven and non-woven GDL [176]. Lin et al, used different gasket thicknesses to control compression and concluded similarly that a compression ratio of 59-64 % for two woven GDL of 320 µm and 460 µm thickness resulted in optimal cell performance [177]. Lee et al, investigated inhomogeneous compression across the footprint area of a single cell using a 500 µm thick GDL and measured average pressures of 13.2-47.7 MPa [178].

Chi et al, carried out a numerical investigation which calculated the effect of GDL compression ratios in the range of 36.0-60.5% on three dimensional temperature, saturation and oxygen distribution across the footprint of the GDL by accounting for its compressed porosity [179]. Their results concluded that high compression ratios could increase

saturation, reduce current densities and invoke greater temperature differences. The study of Zhou et al, conducted a similar study based on the FEA and demonstrated that GDL compression can reduce contact resistance and hinder the transport of reactants and liquid water [180].

The ex-situ investigation of Bazylak et al, employed fluorescence microscopy to visualise the breakthrough of water fronts through to the surface of the compressed GDL [181]. Their results suggest that highly compressed regions of the GDL will experience the most aggressive morphological change and result in a loss of hydrophobicity.

Although the literature contributes an insight into the effect of compression on cell performance through in-situ performance characterisation, macro-homogeneous modelling or ex-situ visualisation, a basic understanding of the nature of the relationship between the compressed structure of the GDL and its transport properties has not been demonstrated to date; as characterising pore-level transport is formidable from an experimental point of view. Therefore a novel approach is needed in order to truly understand the effect of compression on pore-scale structure and transport.

The following sections provide detailed X-ray µCT/nCT characterisation of both uncompressed GDL and compressed GDL.

4.3 MICRO/NANO CHARACTERISATION OF UNCOMPRESSED GDL

The following sections provide a detailed characterisation of a number of GDL through X-ray µCT and nCT.

4.3.1 Experimental

Four non woven (FP_27_15, IP_46_38_80, IP_48_40_100, IP_48_40_160) and a woven GDL sample (SCCG_5N) were imaged using a SkyScan 1072 µCT, with a source voltage of 50 kV and a current of 100 µA without filtering of the X-rays. On average, 2 frames of 2 sec exposure time were acquired at each 0.9° rotation step. This generated 207 shadow images (Figure 4.1a,b) with a voxel size of 1.95 µm for non woven samples and 1.76 µm for the woven material in around 50 minutes for each sample.

Nano characterisation of another two woven (HP_28_35, HP_30_35) and a woven GDL (SCCG_5N) samples was carried out using SkyScan 2011, with a source voltage of 25 kV and a current of 200 µA without filtering of the X-rays. On average, 2 frames of 2 sec exposure time were acquired at each 0.5° rotation step. This generated 371 shadow images (Figure 4.1a,b) with a voxel size of 680 nm for the non woven samples and 970 nm for the woven material in around 45 minutes for each sample.

It is noteworthy to say that the sample names refer to the date of manufacture and the chronological trial numbers in a sequence of events produced by TFP (Technical Fibre Products Ltd.)

4.3.2 Image processing and key parameters calculations

The shadow images were then processed using the modified Feldkamp filtered back projection method to reconstruct the 2D greyscale slices similar to Figure 4.1c,d as discussed in Chapter 3. Then the slices were thresholded. The optimal threshold was

chosen in which the porosity, average fibre diameter and continuity of the resultant digital model are most close to the references. References including average fibre diameter, porosity and continuity in the material were obtained from SEM images of the surface of the GDL and manufacturer data as summarised in Table 4.1.

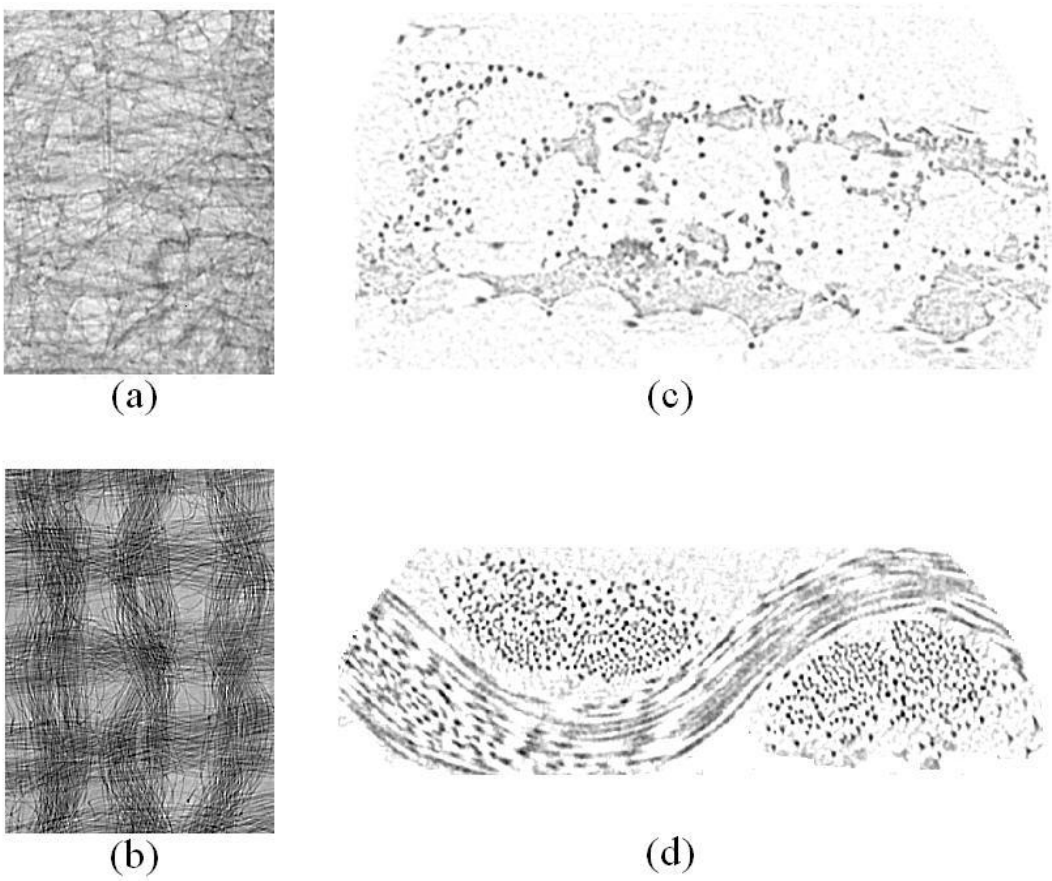

Figure 4.1. X-ray tomography images of GDL samples; (a) Shadow x-ray tomography image of carbon paper sample; (b) Shadow x-ray tomography image of carbon cloth sample; (c) A reconstructed 2D slice image of the carbon paper using CTAN software; (d) A reconstructed 2D slice image of the carbon cloth.

Table 4.1. Average fibre diameter of the GDL thresholded samples, reference value of fibre diameter based on SEM images, porosity results from X-ray µCT and reference value of porosity for the non-woven GDL carbon papers. The sample names refer to the date of manufacture and the chronological trial numbers in a sequence of events produced by TFP (Technical Fibre Products Ltd.)

GDL code	Tomography method	Average fibre diameter (µm)	Reference value of fibre diameter (µm)	Porosity (%)	Reference value of porosity (%)
FP_27_15	X-ray µCT	7.9	7.90±0.05	82.3	82±1
IP_46_38_80	X-ray µCT	8.8	9.00±0.05	89.4	90±1
IP_48_40_100	X-ray µCT	6.8	6.70±0.05	84.2	84±1
IP_48_40_160	X-ray µCT	7.2	7.00±0.05	76.0	75±1
HP_28_35	X-ray nCT	7.3	7.10±0.05	83.4	85±1
HP_30_35	X-ray nCT	7.1	7.00±0.05	84.9	84±1
SCCG_5N	X-ray µCT	8.2	7.80±0.1	82.1	N/A
SCCG_5N	X-ray nCT	8.7	7.80±0.1	81.8	N/A

The 3D reconstructed image of each sample was carried out using CTAN software (please refer to Chapter 3) and the results are shown in Figure 4.2 and Figure 4.3. Pore size distribution is given in Figure 4.4 and Figure 4.5. Other parameters including porosity, mean pore radius, degree of anisotropy, centroid tracking tortuousity, effective diffusion coefficient, and Tomodakis-Sotirchos permeability are all summarised in Table 4.2. The tortuous path of centroid tracking of each sample is shown in Figure 4.6.

Table 4.2. Key micro/nanostructural parameters of various GDL samples obtained directly from 3D digital images. The grey region represent the non-woven samples while the woven material parameters are given in the white region.

Sample code / **Parameter**	**IP_48 40_160**	**IP_48 40_100**	**FP 27_15**	**HP 28_35**	**HP 30_35**	**IP_46 38_80**	**SCCG 5N µCT**	**SCCG 5N nCT**
Porosity [%]	76.0	84.2	82.3	83.4	84.9	89.4	82.1	81.8
Fibre diameter [µm]	7.2	6.8	7.9	7.3	7.1	8.8	8.2	8.7
Pore average radius [µm]	22.5	20.3	34.5	15.6	18.6	41.5	20.13	17.01
Degree of anisotropy	0.89	0.83	0.89	0.97	0.66	0.94	0.86	0.81
Centroid tracking tortuousity	1.25	1.19	1.20	1.09	1.13	1.10	1.19	1.11
Effective diffusion coefficient	0.608	0.707	0.65	0.785	0.74	0.81	0.69	0.69
Tomadakis-Sotirchos permeability [$\times 10^{-6}$ mm^2]	3.4	9.74	9.78	9.88	11.9	43.4	10.2	11.0
LB air Permeability [$\times 10^{-6}$ mm^2]	--	--	--	2.1	--	--	9.87	--
Air permeability test [$\times 10^{-6}$ mm^2]	0.10	0.90	1.83	1.87	18.6	25.5	13.0	13.0

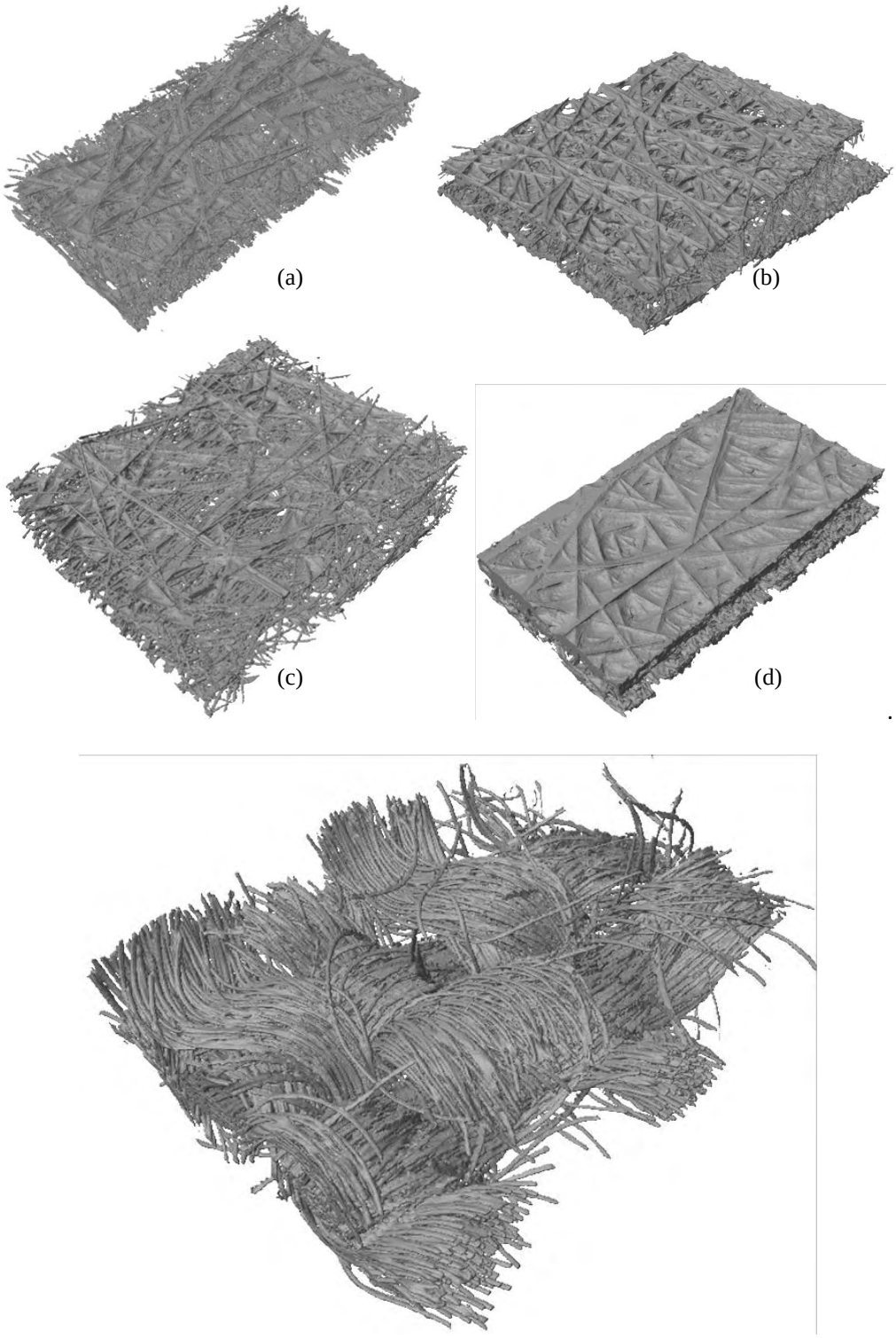

Figure 4.2. 3D reconstructed image of various non woven GDL samples with a voxel size of 1.95 µm for: a) GDL FP_27_15; b)IP_46_38_80; c)IP_48_40_115; d)IP_48_40_160 and voxel size of 1.76 µm for: e) woven SCCG_5N GDL sample.

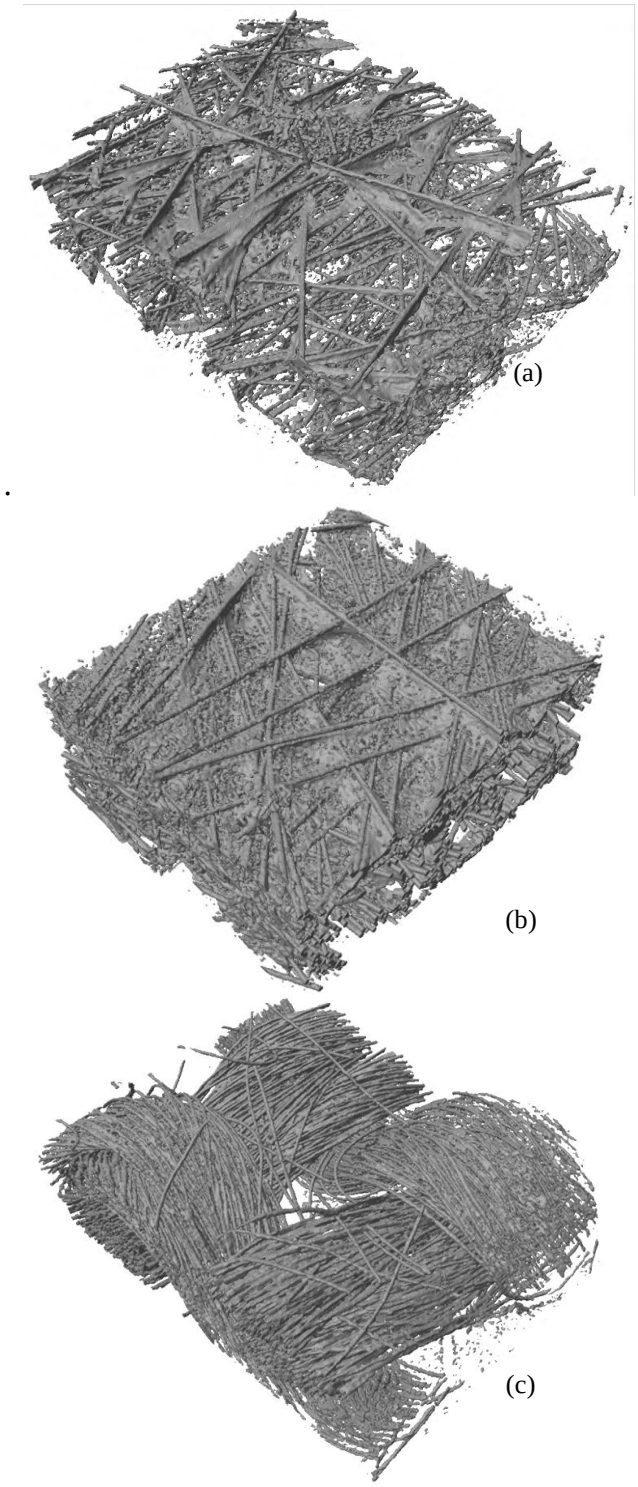

Figure 4.3. 3D reconstructed image of two non woven GDL samples with a voxel size of 680 nm; a) GDL HP_28_35; b) GDL HP_30_35 and; c) Reconstructed image of woven SCCG_5N sample with voxel size of 970 nm.

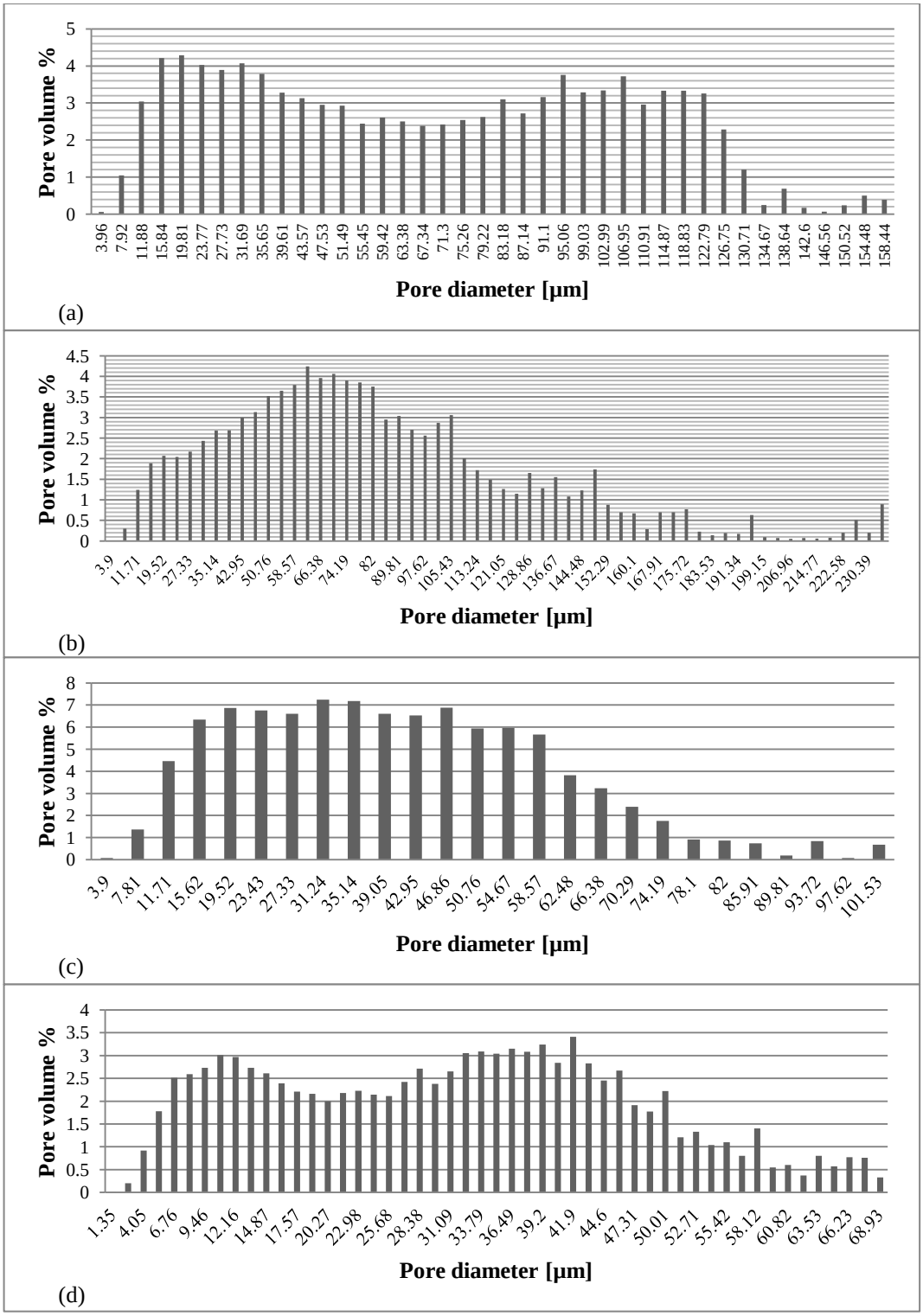

Figure 4.4. 3D Pore size distribution of different uncompressed GDL samples; a) FP_27_15; b) IP_46_38_80; c) IP_48_40_100; and d)IP_48_40_160

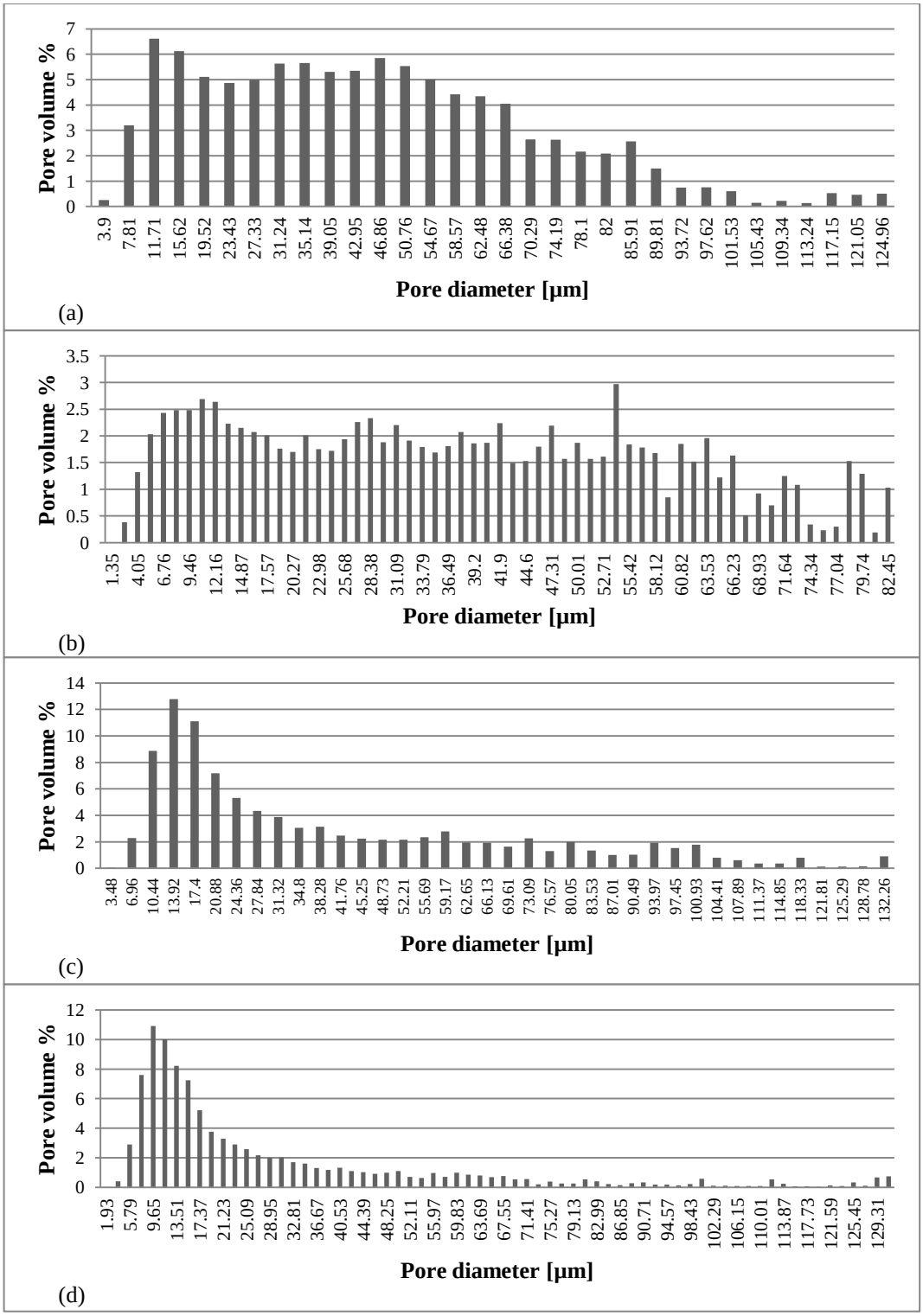

Figure 4.5. 3D Pore size distribution of different uncompressed GDL samples; a)HP_28_35; b)IP_30_35; c)SCCG_5N based on X-ray µCT images; and d)SCCG_5N based on X-ray nCT images.

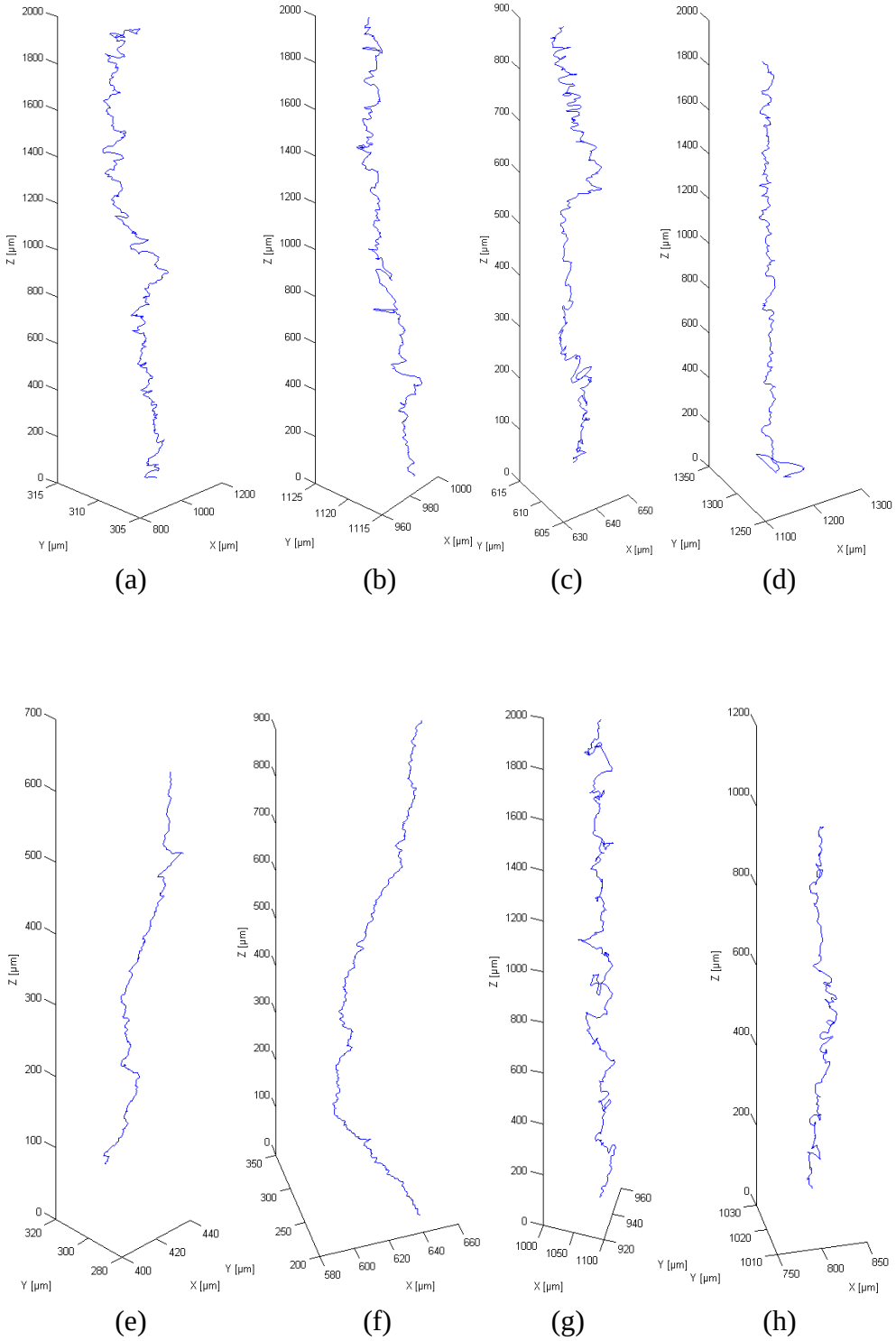

Figure 4.6. Tortuos path of the centroid tracking of GDL samples; a) FP_27_15; b) IP_46_38_80; c) IP_48_40_100; d)IP_48_40_160; e)HP_28_35; f)IP_30_35; g)SCCG_5N based on X-ray µCT; and h)SCCG_5N based on X-ray nCT.

The local effective diffusivity of a gas D_{eff} is a function of the porosity and level of liquid water saturation in the GDL. Its value can be estimated using the Tomadakis and Sotirchos approach [50]:

$$D_{eff} = 1.09 D_{gas} \varepsilon_B (\varepsilon_B - 0.11)^{0.785} (1-s)^2 \quad (4.1)$$

where the multiple of D_{gas} on the right hand side can be referred to as the Tomadakis-Sotirchos effective diffusivity factor, K_{TS} ($K_{TS} = 1.09\ \varepsilon_B\ (\varepsilon_B\text{-}0.11)^{0.785}(1\text{-}s)^2$). Figure 4.7 shows the dependence of K_{TS} on liquid saturation using the porosities of the GDL HP_28_35 of 84.9%. The gas diffusivities [26] of hydrogen, oxygen and water vapour can be determined as 114.0 mm^2/s, 34.5 mm^2/s and 30.3 mm^2/s respectively. Therefore, with 50% saturation, the effective diffusivity of the gases reduces to 20.0 mm^2/s, 6.21 mm^2/s and 5.45 mm^2/s in GDL HP_28_35.

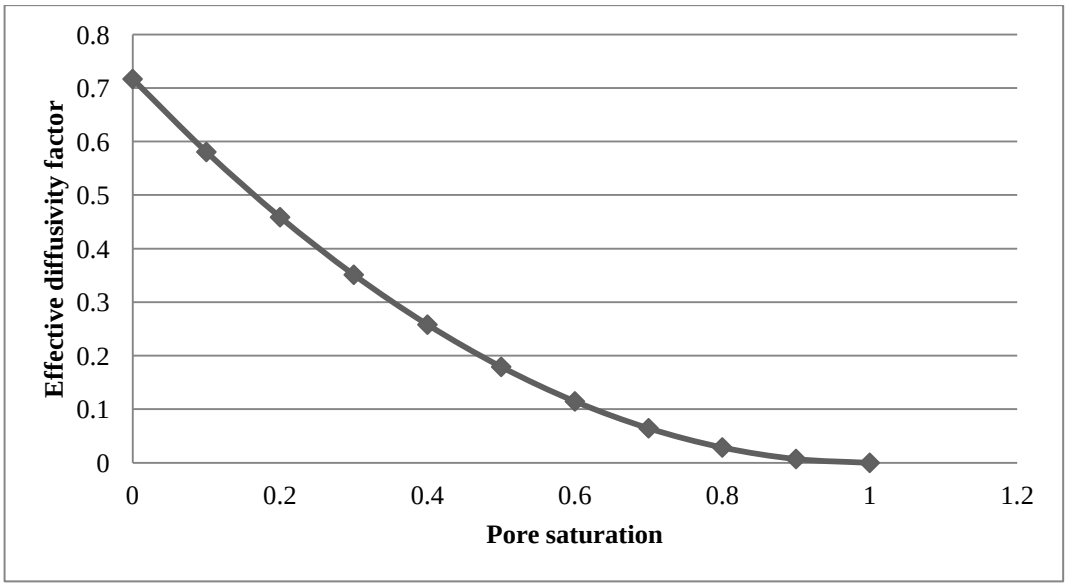

Figure 4.7. Calculated Tomodakis Sotirchos effective diffusivity factor as a function of liquid saturation for the reconstructed models of GDL hp_28_33. GDL porosity is 84.9%.

4.3.3 Discussion

Permeability is the key parameter for comparisons. The permeability obtained from the Tomadakis-Sotirchos approach predicts that IP_48_40_160 and IP_46_38_80 have the highest and the lowest permeability between the non-woven samples, as shown in the grey region of. Although the absolute value obtained from analytical calculation cannot predict the real permeability closely, the trend in increasing in permeability from left to right in the grey region of Table 4.2 is agreed by both the analytical approach and the experimental. However, LB air permeability results show that the method estimates the permeability in non-woven materials much more accurately than analytical calculations.

For the woven SCCG 5N sample, permeability from analytical calculations based on the X-ray nCT images is more accurate and closer to the experiment than that of X-ray µCT. This might be due to the higher resolution of the nCT images. The LB method also accurately determines the permeability in the non-woven material based on SCCG 5N X-ray µCT images.

A detailed characterisation of an uncompressed GDL based on X-ray µCT/nCT images was provided. As discussed in section 4.2, it is necessary to compress a PEFC stack under high compressive loads. The purpose of the next section is to capture the effect of compression on the porous structure of a SCCG 5N woven GDL.

4.4 COMPRESSED GDL CHARACTERISATION

The specific objectives of this section are to apply a polymer-based curing technique to capture the compressed structure of a GDL under a range of compressive loads to characterise the effect on thickness, porosity, average pore size and pore size distribution.

In this section, the sample preparation and X-ray µCT characterisation are discussed.

4.4.1 Compressed GDL X-ray µCT experimental

The GDL sample is saturated with polydimethylsiloxane (PDMS) and then heat-treated while under compression to set it in its compressed state. PDMS is a silicone-based organic polymer which has a specific density of 1.03 at room temperature and cures to form a flexible elastomer [182]. As an encapsulant, it is inherently suitable for the purposes of the current work.

The PDMS-saturated GDL is compressed with a given weight in an oven at 333 ^{o}K for 30 minutes. Both sides of the sample are covered with protective thin aluminium sheets before being flat-pressed to ensure that the samples can be easily removed after curing. The weight is preselected in order to achieve a given uniform compression pressure which is representative of those experienced in operational fuel cell stacks.

As the current study focuses on a range of compressive loads, a number of PDMS-set samples are generated for digital reconstruction. Figure 4.8 shows a flat-pressed 1×1 cm^2 GDL sample cured under a weight of 10 kg.

Figure 4.8. Compressed woven GDL SCCG_5N sample [183].

For the current study, a 3D model of the woven sample is generated by progressively rotating the sample through 0.9 degrees and taking one X-ray µCT image after each step rotation. To visualise the entire sample it is rotated around 180^{o} which results in 207 shadow images. The X-ray imaging is carried out in a SkyScan 1072 system which contains an X-ray source of 50 kV at 100 µA. Images are acquired using a Hamamatsu X-ray camera that has a 1024 by 1024 pixel size with a 12-bit depth with pixel size of 1.76 µm. Then the shadow images are compiled into a stack of 2D greyscale slices using CTAN software.

4.4.2 Image processing and 3D reconstruction

In order to distinguish between fibrils, PDMS material and void space on the greyscale, a threshold process through the CTAN software based on Otsu's algorithm, is applied to a randomly chosen slice and then applied to the whole stack of slices. The thresholded 2D images are subsequently compiled to generate a complete 3D digital model of the GDL. Figure 4.9a-e shows the digital structural models of the GDL samples acquired from a range of compressive pressures. Figure 4.10a-e reveals the binary 2D cross sections. Also the thickness, porosity and average pore size are summarised in Table 4.3. PSD results are given in Figure 4.11.

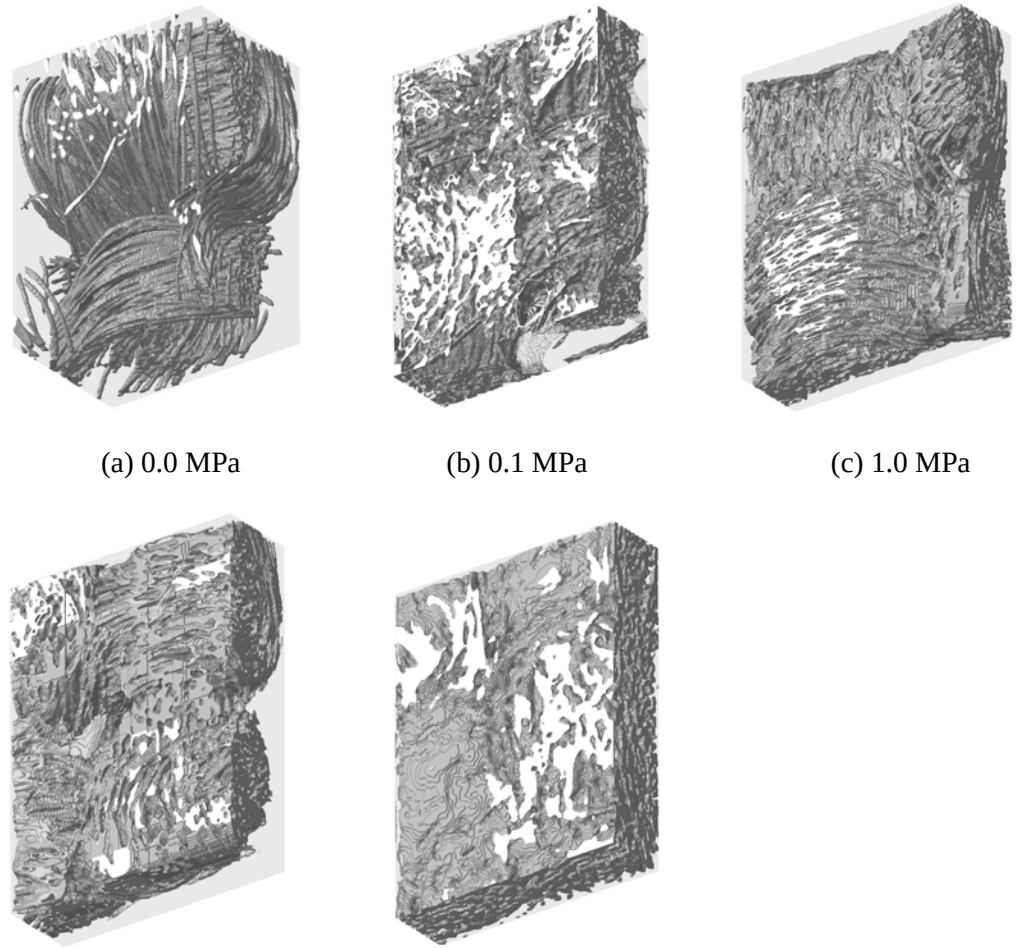

(a) 0.0 MPa (b) 0.1 MPa (c) 1.0 MPa

(d) 10 MPa (e) 100 MPa

Figure 4.9. 3D reconstructed structural models of the woven GDL under a range of compressions; (a) 0.0 MPa; (b) 0.1 MPa; (c) 1.0 MPa; (d) 10.0 MPa; (e) 100.0 MPa [183].

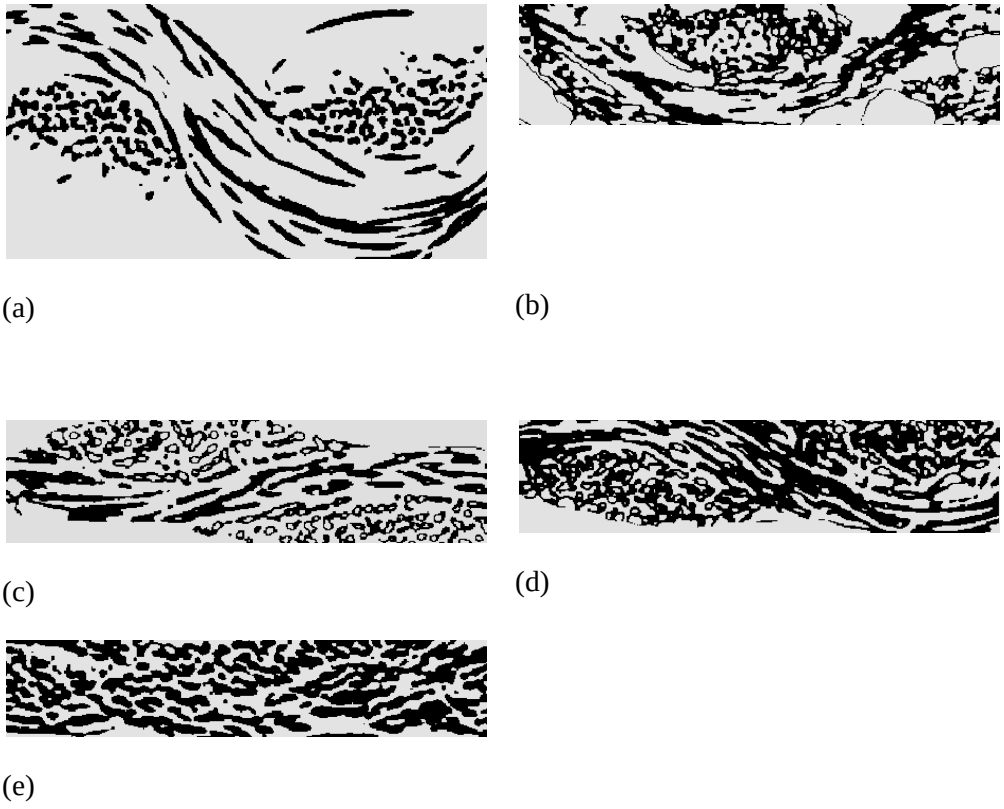

Figure 4.10. Binary cross section images of carbon cloth GDL to show the deformation of cross sections with compression pressure; (a) 0 MPa; (b) 0.1 MPa; (c)1 MPa; (d) 10 MPa; (e) 100 MPa [183].

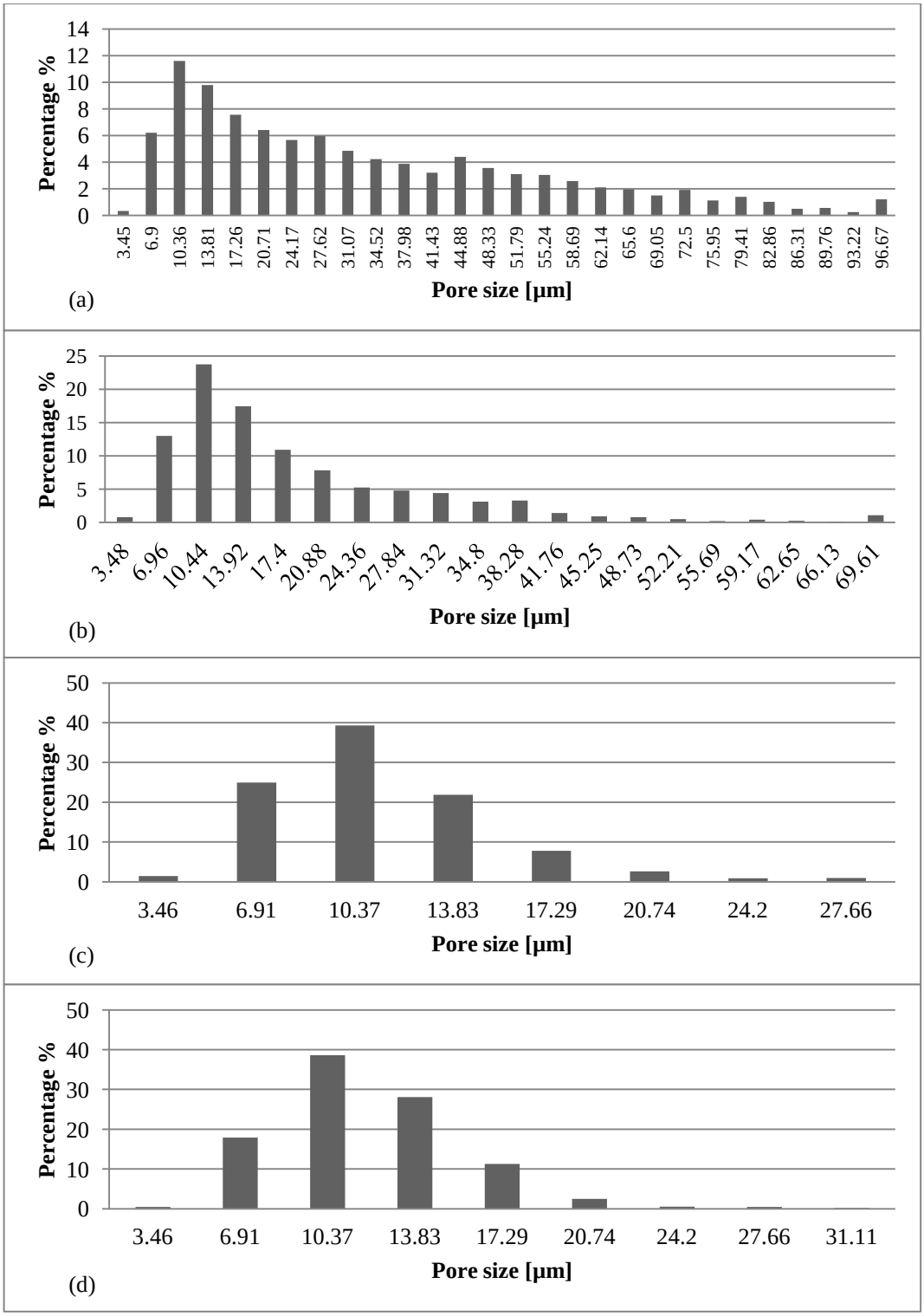

Figure 4.11. Pore size distributions for the structural models of the carbon cloth GDL under a range of compressive loads; (a) 0.1 MPa; (b) 1 MPa (c) 10 MPa; (d) 100 MPa.

Table 4.3. Key micro structural parameters of compressed woven SCCG_5N GDL samples obtained directly from 3D digital images.

Compression / Parameter	0.0 MPa	0.1 MPa	1.0 MPa	10 MPa	100 MPa
Sample thickness [µm]	370	172	168	160	147
Pore average size [µm]	44	33	18	11	11
Porosity [%]	76.0	66.0	53.0	40	45

4.4.3 Discussion

It is obvious from Table 4.3 that the thickness of the samples is decreased from 372 µm to 147 µm (measured from tomography images) which confirms that the compression is well maintained during the imaging by the PDMS material. There is a small change in the thickness from 0.1 MPa to 1 MPa compression which means that the structure can resist in this range of compression. In fact the arrangement of fibrils is quite similar in Figure 4.10b-c. However, increasing the pressure up to 100 MPa changes the structure significantly and possibly breaks the fibrils and packed them together as shown in Figure 4.10e. The fibrils arrangement is totally different compared to Figure 4.10a-d.

Figure 4.11a-d shows that the peak pore size does not significantly change with compression and typically lies in the 10-14 µm band. Actually this band comprises 21% of the total pore volume at 0.1 MPa compression and increases to 67% with 100.0 MPa compression. Average pore sizes in Table 4.3 shows that the mean pore diameter decreases from 44 µm to 11 µm.

Finally the porosity decreases from 76.0% to 40% for the corresponding compressions ranging from 0.0 MPa to 10 MPa but a 5% percent increase is seen for a higher compression of 100 MPa which could be due to the break and deformation of fibrils and a significant change of the structure when higher pressure is applied.

4.5 SUMMARY

Detailed characterisation of a number of uncompressed GDL samples are given in Section 4.3. Five nonwoven and a woven GDL were reconstructed through X-ray µCT with 1.95 µm and 1.76 µm pixel sizes. Other woven and nonwoven samples were imaged using X-ray nCT with 970 nm and 680 nm pixel sizes respectively.

Greyscale images of both µCT and nCT were finely thresholded through the technique explained in Chapter 3. Then the 3D reconstruction of the samples was given. Based on the 3D model, then the porous material key micro/nanostructural information including porosity, pore size distribution, average fibre size, average pore size, centroid tracking tortuousity, degree of anisotropy, effective diffusivity and permeability were obtained.

Permeability was measured through an air permeability tester for all samples. The permeability obtained from an analytical approach and LB simulation were compared to the experiments. It shows that the analytical method predicts the highest and lowest permeability of the samples similar to the air permeability tester results although the analytical values have more than 50% error in most cases. However, permeability obtained from the LB simulation showed minimal error.

The local effective diffusivities of a nonwoven GDL were calculated through Tomadakis-Sotirchos approach based on porosity and liquid water saturation. It shows that local effective diffusivities of different gasses are decreased since diffusivity factor is decreased.

Characterisation of compressed woven GDL samples was presented. It has been demonstrated that the image processing technique developed for the current work can capture the 3D compressed microstructure of a woven GDL over the range of 0 – 100 MPa. The sample is immersed with PDMS and pressed under compression to capture its

compressed fibre structure. Then 3D X-ray tomography, image thresholding and digital reconstruction were applied respectively and resulted in a 3D digital model of the compressed GDL structure. The results demonstrate that this process has been successfully applied to a batch of carbon cloth GDL for five compression pressures representing the 0 – 100 MPa range.

Results also suggested that the thickness and porosity of the samples is generally decreased which confirms that the compression is maintained during the imaging by the PDMS material. There was a small change in the thickness from 0.1 MPa to 1 MPa compression which showed that the structure can resist in this range of compression. However, increasing the pressure up to 100 MPa changes the structure significantly and possibly breaks the fibrils and packs them together.

Finally, average pore sizes showed that the mean pore diameter decreases simultaneously from 44 µm to 11 µm. However, the peak pore size does not significantly change with compression and typically lies in the 10-14 µm band.

The characterisation of uncompressed GDL and compressed GDL were presented in this Chapter. However, the X-ray µCT/nCT resolution is not high enough to capture the detailed geometry of the MPL and CL. The following two Chapters are dedicated to SEM stereo imaging for FIB milling characterisation and FIB/SEM nanotomography of MPL and CL.

5 CHAPTER 5: FIB MILLING CHARACTERISATION AND SEM STEREO IMAGING TECHNIQUE

5.1 INTRODUCTION

FIB based nanotomography provides the possibility to visualise even smaller porous features with higher resolution. The FIB nanotomography involves milling away thin sections. The required time for milling off the thin sections is related to the milling rate of the material. The milling rate of porous MPL and CL are not known and cannot be easily calculated through common theories and simulations. On the other hand, current experimental methods are either time consuming or inaccurate. This Chapter presents the application of a SEM stereo imaging technique to reconstruct the surface of the samples to obtain the volume of the removed material. The volume is then used to calculate the milling rate. On this basis, the FIB technique is developed and explained in the next Chapter. This Chapter starts with a brief description of the FIB milling yield of a material and ion-matter interaction in section 5.2. The SEM stereo imaging for 3D reconstruction of the surface is then explained in section 5.3. For validation, the technique is then applied to characterise the milling yield of a number of common metals and silicon. The results are compared to the previous research in section 5.4. In section 5.5, the validated technique is used to characterise the FIB milling of MPL and CL. In section 5.6, the SEM stereo imaging technique is extended to characterise the surface of urinary catheters, micropipette tip and diatomaceous frustules. Finally, section 5.7 summarises this Chapter.

5.2 FIB MILLING/SPUTTERING YIELD AND ION-MATTER INTERACTION

FIB patterning is applied for three dimensional milling or deposition at micro and nano scale. Focused ions incident on a solid collide with constituent atoms and remove them from the substrate surface. The average number of atoms removed from a solid surface per incident particle is defined as sputtering yield (Y). The sputtering yield depends on various parameters: incident ion (energy, mass, ion dose rate, angle of incidence and clustering), incident material (masses and atomic fractions, crystal orientation, surface bonding energy, conductivity and surface curvature) etc. For normally incident ions the threshold energy is 20-40 eV and the yield generally increases with ion energy having a wide energy region of 5-50 keV [184],[185].

According to the linear collision cascade theory developed by Sigmund, the sputtering yield can be calculated by the following equation:

$$Y_{tot}(E_0) = \frac{4.2 \times 10^4 a S_n}{U_s}, a = 0.15 + 0.13 \frac{M_{t\,\mathrm{arg}\,et}}{M_{ion}} \tag{5.1}$$

Where U_s , S_n are the surface potential and the reduced nuclear cross section and M is the molecular weight.

This theory cannot predict the yield of heavy targets. It describes closely the mass and binding effects at the incident energy higher than 1 keV but fails to deal with the density effect [186].

On the other side, various codes have been reported on the basis of the linear collision cascade theory for crystaline targets and called "static" Monte Carlo codes such as MARLOWE, COSIPO, ACOCT, crystal TRIM and for amorphous targets such as TRIM, ACAT, SASAMAL and "dynamic" codes like TRIDYN, ACTA-DIFFUSE, dynamic SASMAL and etc. These simulations have good predictions but still there are several

factors which influence the sputtering yield, such as different binding energies of different atoms, segregation of elements at the surface and diffusion in the implanted layers of the solid [187],[188].

There are mainly three non-linear parameters which affect the sputtering volume: the first one is the angle of incidence. The sputter yield increases monotonically with up to a maximum of near 60-80^{o}. A dependence of the angle of incidence is expected by $Y(\varphi)/Y(0)=1/\cos^{\beta}(\varphi)$, where φ is measured from the surface normal. The second effect is re-deposition which is very dependent on the milling strategy. It has a negative effect on the yield as far as some particles will be milled more than once. The last parameter is ion channelling which occurs in the crystalline materials where ions can penetrate deep into low index directions that affect the sputtering yield [184],[186],[189].

For practical reasons the yield can be expressed as μm^3/nC [volume per nano Coulomb]. The relationship between atomic sputter efficiency and the unit is calculated by:

$$Y_{\mu m^3/nC} = \frac{Y_{atom/ion} \times M}{96\rho} \tag{5.2}$$

Where M is molecular weight and ρ is the density of the target material in g/cm^3 [190].

If the ion beam current and the milling time are known then the applied dose (nC) could be easily obtained. Then the actual depth of the milled hole is required to calculate the volume of removed material (μm^3). Milling time and beam current are easy to record and adjust but the actual volume or height of the milled hole is a difficult task. Here, a method to reveal the 3D structure of the hole is presented.

5.3 SEM STEREO IMAGING TECHNIQUE

This method is based on the computing 3D points from 2D matched points into two images, one tilted with respect to the other. These images are taken by SEM with a normal tilting angle between 5^o to 10^o.

Recently, it has been successfully employed for surface characterization of surfaces [191][192][193]. Figure 2 shows the effect of tilt angle (α) on the coordinates of point *P1*, projected on to the *XY* plane; *P2* is the corresponding point in the tilted image. In this figure, *X* lies in the plane of the untilted image, *Y* is perpendicular to *X* and *Z* lies in the direction of the electron beam.

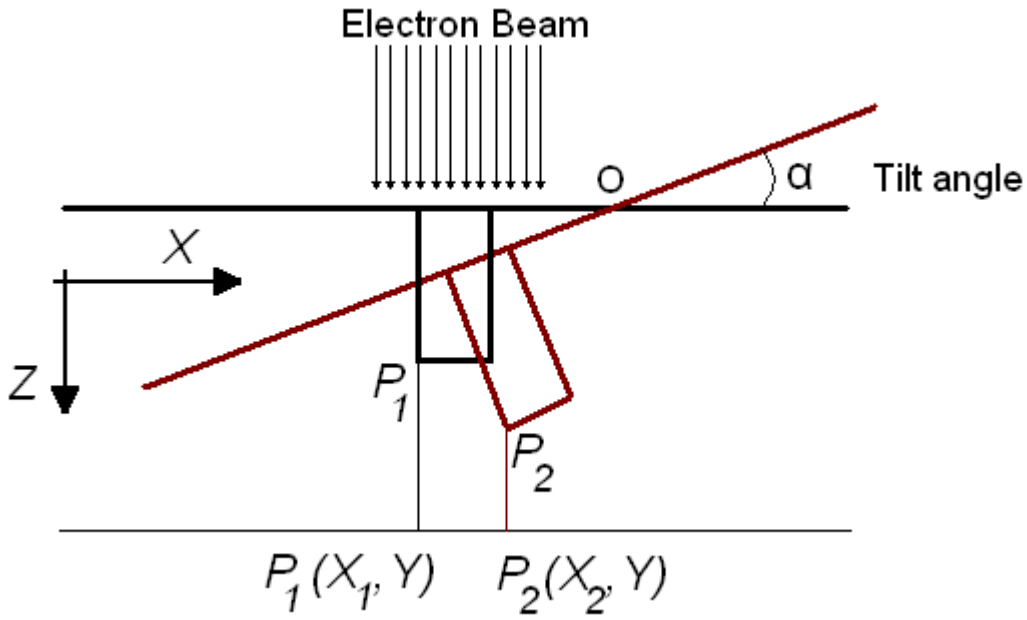

Figure 5.1. Stereo images of an object before (black) and after (red) tilting. Tilting about O transforms P1 to P2.

The Z-coordinate of P1 can be calculated from [191][192]:

$$Z = \frac{X_1 - X_2}{\sin\alpha} = \frac{X_1(1-\cos\alpha)}{\sin\alpha} \tag{5.3}$$

This process can be done for all of the other points of both images and finds the shape of the structure.

In order to get the best performance of the method, reduce the image noises and obtain the maximum volume of 3D reconstruction, several parameters should be considered as below [192],[193],[194],[195]:

- The reconstructed feature should be visible and perfectly show sharp edges even at high magnifications.

- The images should be "eucentrically" tilted about one axis which means that a particular feature should be seen at the centre of both stereo pair images.

- A large height change in relation to the image diagonal provides better results; the minimum ratio of height to diagonal is 1:70. This issue depends on tilting angle. The higher the tilt angle, the higher the change in the height, but by increasing the tilt angle, this can bring surface regions out of volume. Thus, there is always a trade off.

- The structures should only have a transition in X direction and not any transition in Y axis.

- The image pair should have contrast without blurring, the same scale, enough textures on the surface and the images should not have a recurrent structure.

In other words, the main parameters are tilting angle and proper magnification to reconstruct a texture correctly. In this case the image reconstruction error will be less than 3-5% [194],[195].

5.4 CHARACTERISATION OF FIB MILLING YIELD OF METALS

Materials such as copper, aluminium, steel, nickel, nickel alumina and silicon are commonly used in the electronic industry and micro system devices, hence it will help plan the FIB processes on these materials if the sputtering yields are identified accurately beforehand. This section reports the experimental work on finding the FIB milling/sputtering yields on these common materials based on the stereo imaging technique. Then the results are compared to simulations and analytical calculation from other research for validation.

5.4.1 Experimental

Experiments were carried out on a FEI dual beam FIB (Strata DB235) with a full motorized stage at "eucentric" height. Samples of copper, aluminium, steel, nickel, nickel aluminium alloy and silicon were milled with an area of 10×10 μm^2. The Ga^+ 30 kV ion current adopted was 1 nano amp for silicon and pure aluminium, and 5 nano amps for other samples. The area was milled for 250 seconds.

Figure 5.2 shows a pair of stereo images of the milled area on copper. The images were taken with $\pm 10^o$ angles respectively. In order to optimize the magnification and tilting angle, the magnification increased till the whole image remains to the field of view. Then the motorized stage is tilted for 45^o and the height of the left corner of the milled structure is measured. This value divided by 0.707 ($sin\ 45^o$) gives the height of the feature. This reference value will be used later for tilt angle optimization.

The milled patterns are scanned at 15,000 magnification with a stereo pair angle ranging from 5-10 with intervals of 1^o. The height of the reconstructed left corner using Mex software (MeXTM, Graz, Austria: Alicona Imaging GmbH.) was compared to the reference value. The results show that tilting angle of 10^o gives close value to the reference. Also the minimum ratio of height to diagonal (1:70) was happened at the angles more than 8^o for the copper sample.

In order to have relative height change in all sides of the milled square in the stereo pair images, the stage is rotated for 45^o otherwise two parallel sides of the square wouldn't have any relative height change in the stereo pair images.

The ion channelling effect is clear in both images. The 3D surface structure can be calculated based on the two SEM images by finding the height of every point afterwards. Commercial software Mex (Alicona) is used for the calculation. Figure 5.3 shows the 3D reconstructed image of the milled part of the copper.

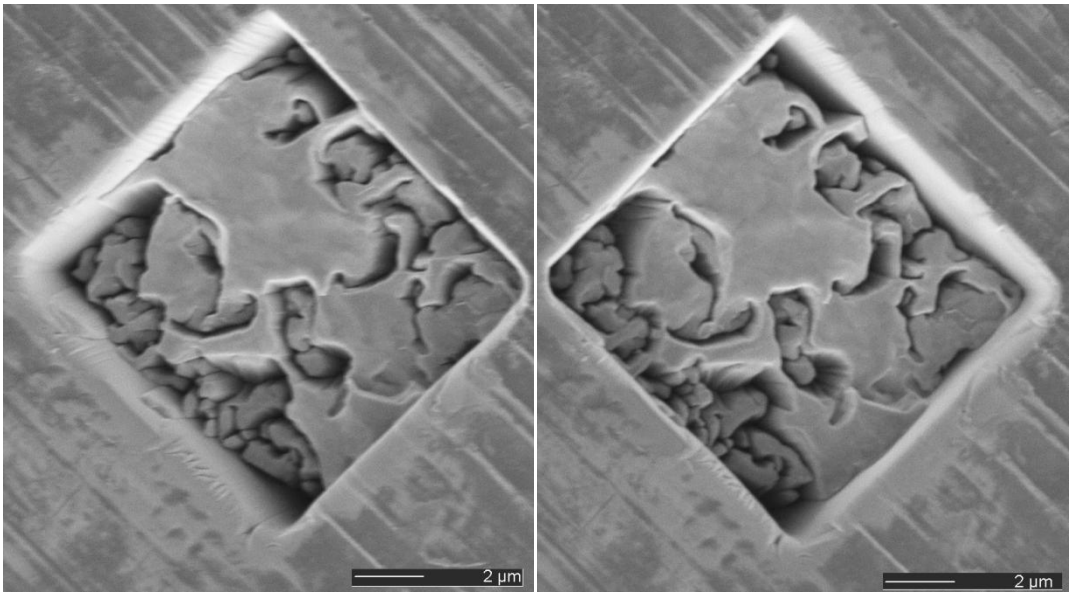

(a) (b)

Figure 5.2. Copper milled area with tilting angle of -10^{o} ; b) Copper milled area with tilting angle of 10^{o}. Although information in the dark areas is not visible, the software can still work with these, because they are still above the minimum gray level of zero.

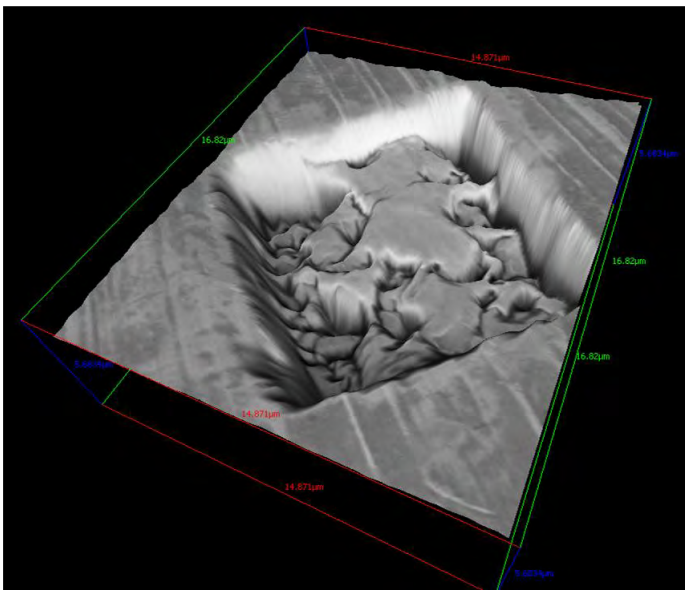

Figure 5.3. 3D reconstructed image of milled area on Copper.

5.4.2 Results

The removed volume underneath the level surface (μm^3) per dose (nC) is calculated for all of the samples and reported as an average value. Polycrystalline materials such as copper and aluminium show fluctuating milled surfaces as within those materials matrices there are many small crystallites with their own orientation. These grains will induce local channelling and will therefore affect the local milling speed. The average is a good indication of the actual yield because the values are taken over several grains in polycrystalline samples. The results of the investigation on various materials are summarized in Table 5.1. Comparison between the experimental results, the theoretical SRIM simulation results and previously reported results are conducted. In [190] the researchers deposited platinum on the milled surface and milled the structure again in order to make a cross section of the first milled square. Due to the high contrast difference between the material and platinum they measure the height of the first milled area by averaging over some 40 selected points. This process has been done several times and has taken several hours.

Table 5.1. Comparison between different methods of average volume per dose for the bulk of metals and silicon.

Material	Average Vol. per dose (μm^3/nC)		
	Stereo Imaging	**Simulation [196]**	**Other works**
Pure Al	0.28	0.44	0.29 [190]
Pure Cu	0.25	0.36	0.25 [185]
Pure Ni	0.11	0.10	0.14 [185]
Steel-316L	0.19	-	-
Ni-Alumina	0.18	0.15	-
Si	0.25	0.35	0.24 [190]

Sputtering yield is not well developed theoretically regarding some non linear effects such as the re-deposition effect. Also experiments done with the FIB are scarce and in the

research works the measurement is time consuming. Using stereo pair images, then it is possible to reconstruct the milled area and calculate directly the removed volume and then the milling yield -without any further platinum deposition and cross section milling- this method is accurate compared with the other methods. The results prove that the new approach is accurate. Therefore the method is applied for FIB milling characterisation of the MPL and CL.

5.5 FIB MILLING CHARACTERISATION OF MPL AND CL

Similar to the experiments explained in section 5.4, the FEI dual beam was used to mill three samples with a low current ion beam. The SEM stereo imaging technique was employed to obtained the volume of the milled area.

Due to the soft nature of the layers, low current ion milling is required. There are only four low current standard settings available with the FIB STRATA 235 dual beam: 1, 10, 30 and 50 pA. The first two options are not practical for these samples as they do not provide clear ion images because the energy of ions is low and focusing on the sample is extremely difficult at low current ion beams [197]. Between 30 and 50 pA, the 30 pA was chosen since that clear focused images were obtained and the re-deposition effect would be lower than 50 pA. Samples of anode CL, cathode CL and MPL were milled with an area of 5×5 μm^2. The Ga^+ 30 kV ion current adopted was 30 pA for all samples. The area was milled for 180 seconds.

Figure 5.6 show pairs of stereo images along with the 3D reconstruction of the milled area on anode CL, cathode CL and MPL. The images were taken with $\pm 10^o$ angles respectively similar to the experiment discussed in section 5.4. The removed volume underneath the level surface (μm^3) per dose (nC) is calculated through reconstructed images for all of the samples and reported as an average value. The yield of materials is 0.92 μm^3/nC, 0.98 μm^3/nC and 1.02 μm^3/nC for anode CL, cathode CL and MPL respectively.

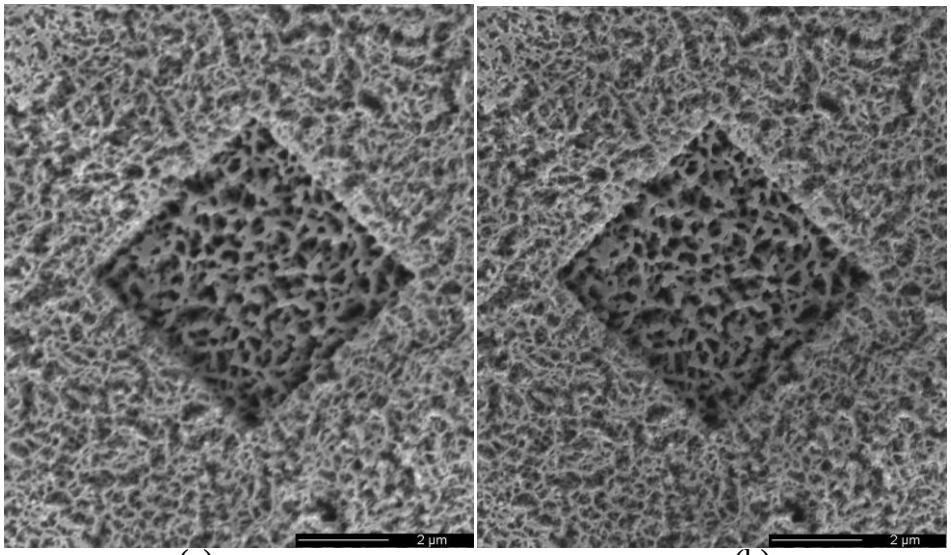

(a) (b)

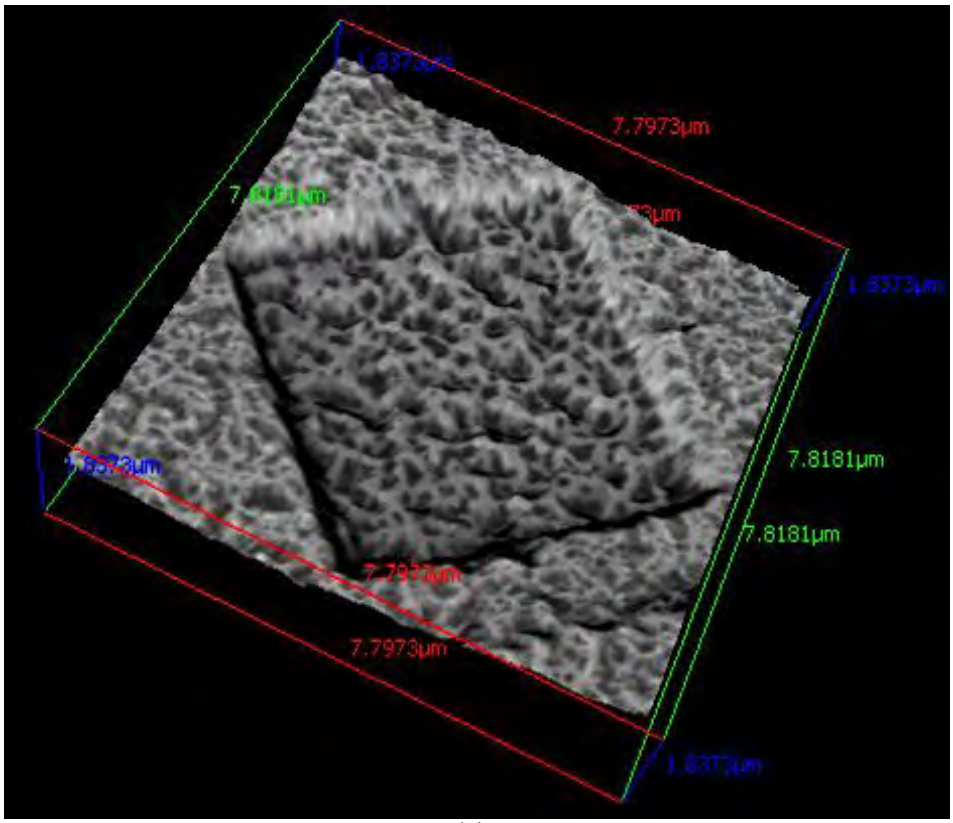

(c)

Figure 5.4. Anode CL milled area with tilting angle of -10^{o}; b) Milled area with tilting angle of 10^{o}; c) 3D reconstructed image of milled area on anode CL.

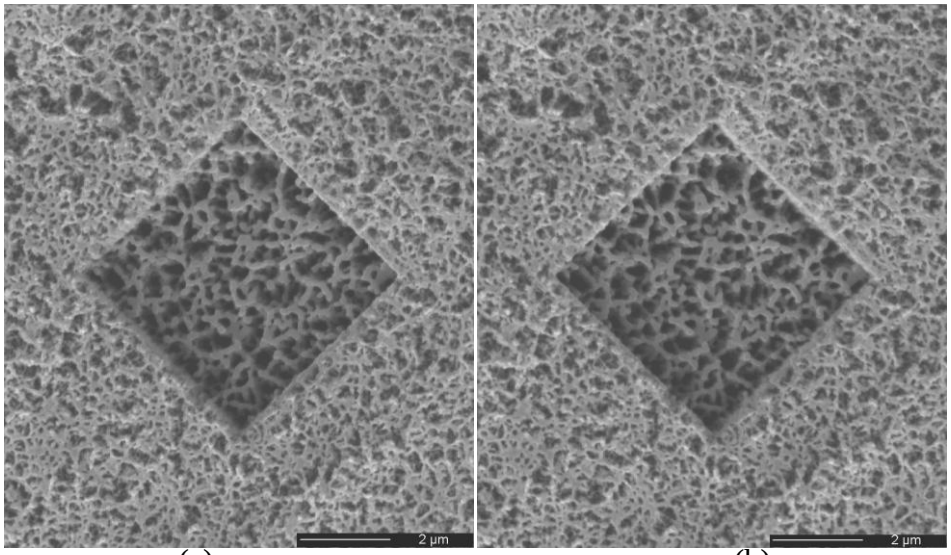

(a) (b)

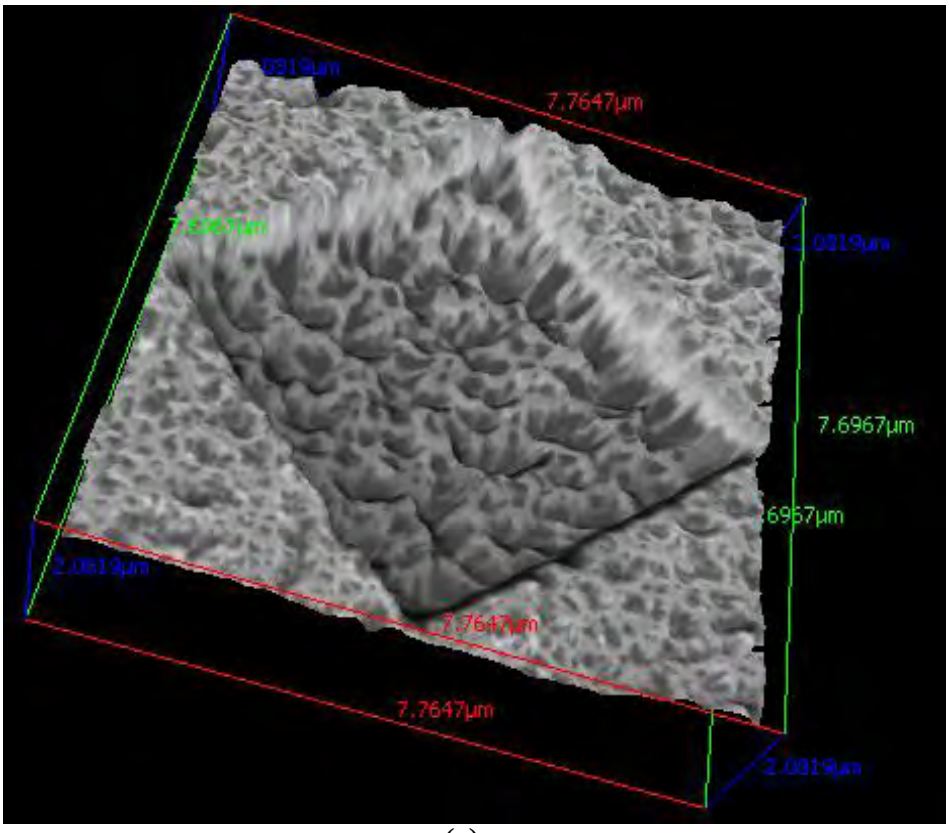

(c)

Figure 5.5. Cathode CL milled area with tilting angle of -10^{o}; b) Milled area with tilting angle of +10^{o}; c) 3D reconstructed image of milled area on cathode CL.

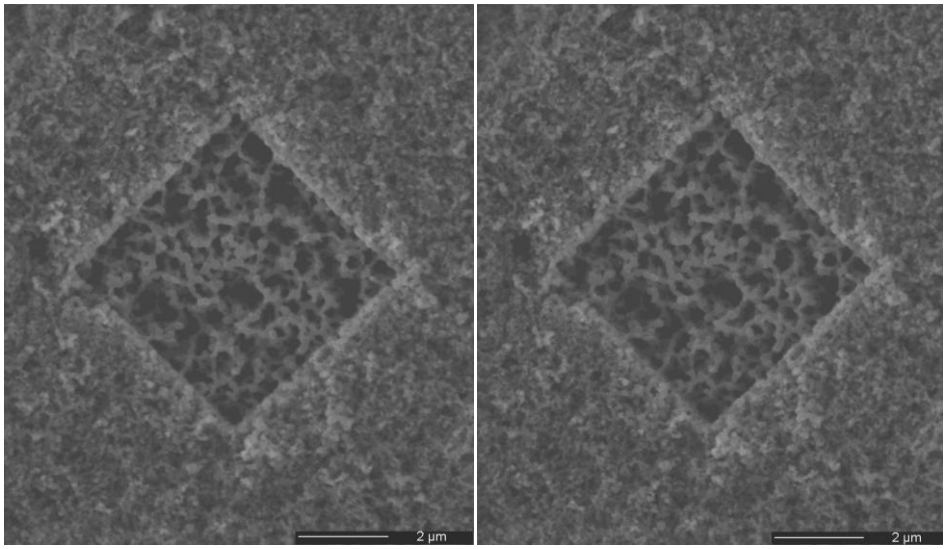

(a) (b)

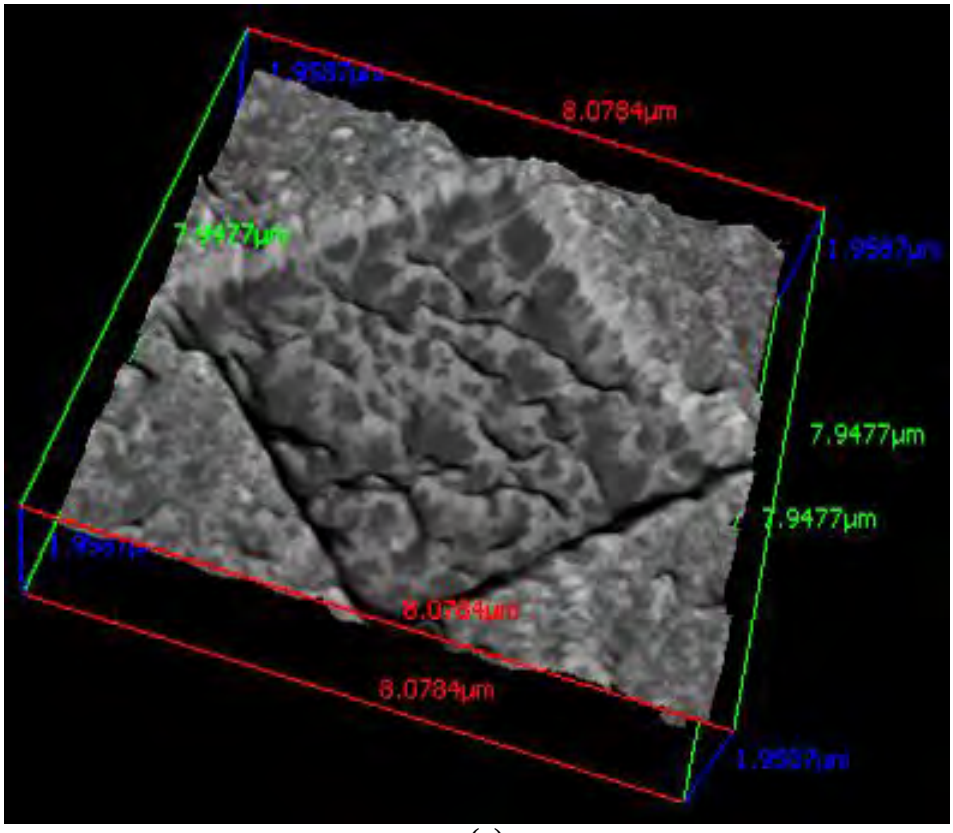

(c)

Figure 5.6. MPL milled area with tilting angle of -10^{o}; b) Milled area with tilting angle of 10^{o}; c) 3D reconstructed image of milled area on MPL.

The SEM stereo imaging method was successfully applied to reconstruct the surface features of various materials including metals, silicon and PEFC MPL/CL. Since the method basically reveals the features of the surface, there is a possibility to measure the surface roughness of the samples.

In the next sections other applications of the SEM stereo imaging technique on the characterisation of urinary catheters, micropipette tip and diatomaceous frustules are discussed.

5.6 OTHER APPLICATIONS

5.6.1 Surface roughness analysis of urinary catheters

Conventional tactile surface roughness measurement accuracy is limited by the stylus tip dimensions since the stylus can only make a good contact in a valley wider than the tip diameter. SEM stereo-imaging is used to reconstruct the surface features of a number of different catheters to validate tactile measurement results.

Catheters are made of relatively soft materials e.g. silicone elastomers, latex and poly(vinyl chloride); latex catheters may be coated with a hydrogel, Teflon or silicone [198]. The Foley catheter is a tube that passes through the urethra to drain urine from the bladder; the proximal end has a domed tip, to aid insertion; below the tip, an eye passes through the wall to allow urine to drain through the tube [199].

There are many reasons why the surface roughness of these catheters, and similar medical devices, may be important. For example, encrusting deposits tend to form on the catheter surface, initially on the outer surface of the proximal end (that is in the bladder), especially around the eye [200]. Imperfections in the catheter surface may then form nucleation sites for crystallization of the minerals that form the deposits [201]. Also, the inner wall of the

bladder may sometimes be sucked into the eye of the catheter [202], [203]; any sharp peaks may then lead to irritation or damage to the bladder.

Measurement of the surface roughness of urinary catheters at two different scales was carried out: by scanning electron microscopy (SEM) stereo-imaging (examining a region of interest of length 100 µm-800 µm) and by conventional tactile methods (scanning lengths of about 5 mm). The former method provides information of the surface features to validate the tactile measurement technique. Figure 5.7 shows a catheter and its eyes with their dimensions.

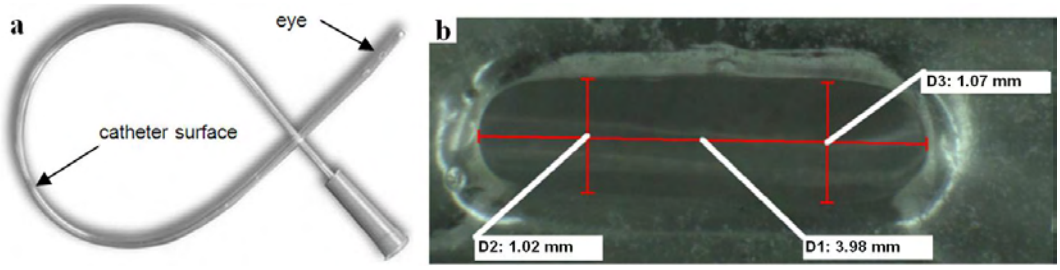

Figure 5.7. A 40 cm urinary catheter showing the eye and (b) an optical micrograph of the eye. The length of the eye (D1) is less than 4 mm.

5.6.1.1 Tactile measurement

In a conventional tactile measurement, a stylus is placed against the surface to be measured and its lateral and vertical movements are recorded while it scans the surface. The stylus has a typical tip radius of a few micrometers and it scans a recommended length of 5 mm. The benefit of this method is that it scans a macroscopic length within a few minutes. The scan length is important because the catheter and the bladder have a contact area of the order of square centimetres.

The resolution of the tactile measurement is limited by the tip diameter of the stylus, as it can only make effective contact, required for a reliable measurement, in a valley wider than its diameter. It is believed that if the average surface roughness (*Ra*) [204] is less than stylus tip radius, the surface features should be verified with a higher resolution device e.g. Atomic Force Microscopy (AFM) or by using a smaller stylus tip for the tactile technique [205]. The disadvantage of using AFM is that the measurement area is very small, typically around 70×70 μm^2, and the corresponding time for each scan is about 1-2 hours. Also AFM measurements could be difficult to apply on the curved surface of catheters since AFM samples are usually flat. Using smaller (less than a micrometer) tips may also cause damage to the surface especially when soft materials are investigated [206].

5.6.1.2 SEM stereo imaging

Here SEM stereo-imaging is used to validate tactile measurements. As discussed in section 5.3, in order to get reliable results from this method, the image noise should be reduced and, to obtain the maximum volume of 3D reconstruction, three further factors should be considered. Firstly, the reconstructed feature should be visible and show sharp edges. Secondly, the images should be "eucentrically" tilted. Moreover, the length of any diagonal line connecting two opposite corners of the images should not be more than 70 times larger than the height of the feature.

5.6.1.3 Experiments and results

As below three series of experiments were performed:

i) Surface roughness measurement of different catheters was carried out using the tactile technique with a stylus radius of 2 µm over a 5 mm sample length with a recommended cut-off length of 800 µm through a Taylor-Hobson machine (Talysurf 120L, Leicester,UK: Taylor Hobson Ltd.). Two different stylus forces (0.5 mN &1 mN) were applied to ensure

that the pressure exerted by the stylus tip was not flattening surface features in the soft catheter material. Results showed that *Ra* changed only 5% when the applied force was doubled. Hence the effect of applied force on the surface is negligible. Table 5.2a shows the values obtained for *Ra*.

ii) For those catheters with an *Ra* less than 1 μm (Nos. 1,2,4,5,7,8,9,12 in Table 5.2) three samples of each catheter surface were examined by SEM stereo-imaging and the surface features investigated for validation (Figure 5.8).

To satisfy the conditions stated in section 5.6.1.2, the samples were coated with a thin layer of gold (~5 nm thick) to make the surface of the catheter conductive in order to facilitate electron imaging and to enhance the image sharpness. The centre point of the image was marked on the SEM screen, and the sample was then tilted until the marked point was positioned on the edge of the image. The position of the specimen was then adjusted so that the marked point was at the centre point of the image again. The process was repeated until the specimen was tilted to the desired angle of 8^o to the horizontal ("eucentric" tilting). Finally, a magnification was chosen such that the length of any diagonal line connecting two opposite corners of the image would be 70 times larger than the height of the feature to be analysed.

Figure 5.8 show a pair of SEM stereo images of the catheter surfaces taken with an SEM (JEOL-7000, Tokyo, Japan: JEOL Ltd.) at an operating voltage of 15 kV. Figure 5.9a shows the reconstructed surface using the commercial MeX software package.

iii) The surfaces of the catheter eyes were also reconstructed using SEM stereo-imaging. Two samples were investigated for each of the twelve types of catheter. The cut-off length was selected as 40 μm over a reconstructed area of 200×200 μm^2 [194]. The average values of *Ra* are reported in Table 5.2b.

Table 5.2. Average roughness of catheters using both methods. a) Catheter surface *Ra* values from tactile measurements; b) Eye surface *Ra* values from SEM stereo-imaging.

Table 5.2a)

Number	*Ra (μm)*	Number	*Ra (μm)*
Cath. 1	0.29	**Cath. 7**	0.07
Cath. 2	0.87	**Cath. 8**	0.16
Cath. 3	5.09	**Cath. 9**	0.08
Cath. 4	0.11	**Cath. 10**	1.12
Cath. 5	0.21	**Cath. 11**	1.34
Cath. 6	1.03	**Cath. 12**	0.16

Table 5.2b)

Number	*Ra (μm)*	Number	*Ra (μm)*
Cath. 1	0.37	**Cath. 7**	0.34
Cath. 2	0.33	**Cath. 8**	0.37
Cath. 3	0.28	**Cath. 9**	0.48
Cath. 4	0.45	**Cath. 10**	0.29
Cath. 5	0.53	**Cath. 11**	0.41
Cath. 6	0.29	**Cath. 12**	0.43

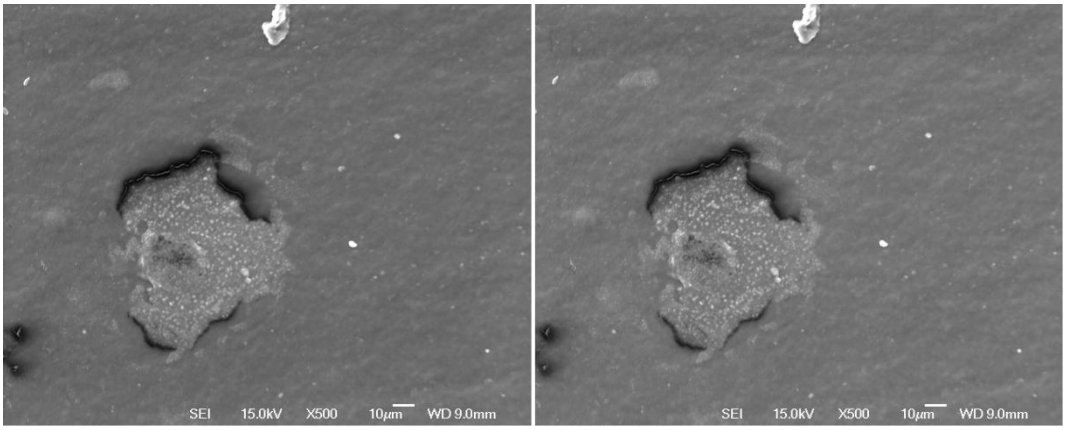

(a) (b)

Figure 5.8. Pair of SEM stereo images of a catheter surface taken with tilt angle of 8^{o}. a) Left image; b) Right image.

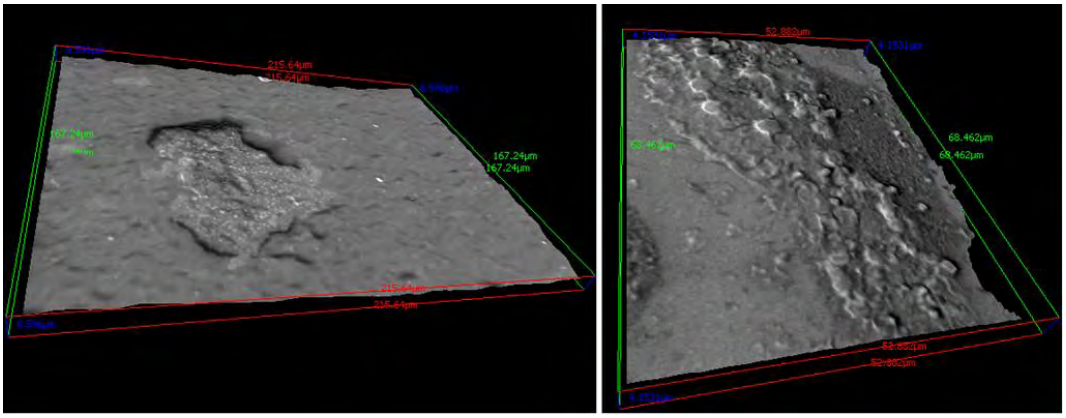

(a) (b)

Figure 5.9. 3D reconstruction of catheter surfaces with Ra less than 1.00 μm. (a) Catheter No. 2 with 0.10 μm < *Ra* < 1.00 μm; features are wider than 5 μm. (b) Catheter No.7 with 0.01 μm < *Ra* < 0.10 μm; features are narrower than 0.50 μm.

5.6.1.4 Discussion

Table 5.2a shows that there are six catheters with 0.10 μm < Ra < 1.00 μm and two catheters (Nos. 7,9) with 0.01 μm < Ra < 0.10 μm, according to tactile measurements. Reconstructed features of the first group of catheters, obtained by SEM stereo-imaging, were similar to those in Figure 5.9a were generally wider than 5 μm and so detectable by the stylus tip in the tactile measurements. In contrast, the width of the valleys of the features of catheter 7, as shown in Figure 5.9b are less than 0.50 μm and consequently the stylus tip is not small enough to reliably characterise them. The *Ra* value of catheter 7 obtained by SEM stereo-imaging over an area of 70×70 μm^2 (with a cut-off length of 8 μm [205]) is 0.14 μm. Reconstructed features of catheter 9 were ~2 μm wide and so may be detectable by the stylus tip.

It should be mentioned that, although SEM stereo-imaging of the catheters can provide useful information of the surface features, the investigated length is around 100 times less than the tactile measurement technique and the cut-off lengths are different. On the other

hand, catheters and the bladder have a contact area of the order of square centimetres and need to be analyzed over a larger area that obtained by SEM images obtain. Therefore, reconstruction of surface features can only be used to ensure whether or not tactile measurement results are reliable. However, for those surfaces with small features which are not detectable by the stylus tip, the Ra results of the SEM stereo-imaging technique with the recommended cut-off length are reported.

For the eyes, only the SEM stereo-imaging results are reported in Table 5.2b. All of the roughness values are less than 1.00 µm using cut-off length of 8 µm.

In this section the fast non-contact method (SEM stereo-imaging) enabled the reconstruction of the features of those surfaces with a roughness of less than 1 µm. The results suggested that if the surface roughness and stylus tip radius differ by an order magnitude, the results of the tactile measurement may not be reliable.

In the next sections other applications of the SEM stereo imaging technique on the characterisation of micropipette tip and diatomaceous frustules are discussed.

5.6.2 Investigation of micropipette tip roughness

The patch clamp technique through a micro pipette was introduced by Neher and Sakmann [207]. The technique has been widely used for the study of cellular ion channels. In patch clamping, suction is applied to one end of the glass micropipette while the other end, the pipette tip, is in contact with the surface of the cell in order to form a very high resistance seal which could reach giga-ohm in resistance. The seal in patch clamping allows recording currents through single ion channels with minimum leakage and high signal-to-noise ratio [208],[209],[210]. The critical factors in giga-seal formation include: cleanliness of both the pipette and the plasma membrane [208],[210],[211], tip geometry,

i.e. roundness, surface roughness of the site in contact with the cells [209],[212],[213], tip size [214],[215] and hydrophilicity of the patch sites [215],[216]. Out of these factors, the roundness and roughness are related to the geometry of the tip and no value has been reported so far to the best knowledge of the author. The roundness measurement through FIB/SEM nanotomography will be discussed in the next Chapter. The surface roughness is measured through SEM stereo imaging.

The glass micropipette was made of borosilicate glass pipes with an outer diameter of 1500 µm and inner diameter of 860 µm (BF150-86-10 Sutter Instrument). The pipe was heated and pulled with a flaming/brown micropipette puller machine (Sutter Instrument Model P-97) to produce micropipette with the tip size of approximately 1.5 µm. The 3D reconstruction was carried out through SEM stereo imaging with the tilting angle of 9^{o} by means of FIB SEM STRATA 235 dual beam. At this angle both images are well focused with sharp edges as shown in Figure 5.10. The 3D surface profile of the pipette as shown in Figure 5.11, was obtained by the processing the SEM images using Mex software.

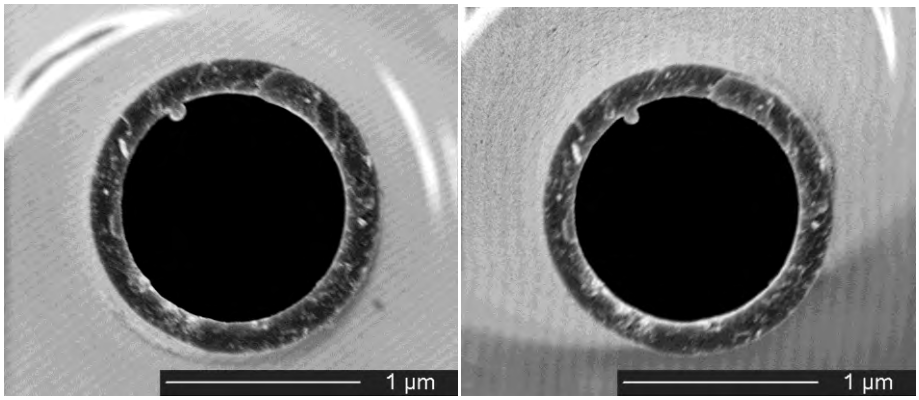

(a) (b)

Figure 5.10. Stereo images of the pipette tip for 3D reconstruction; a) Left image and; b) Right image.

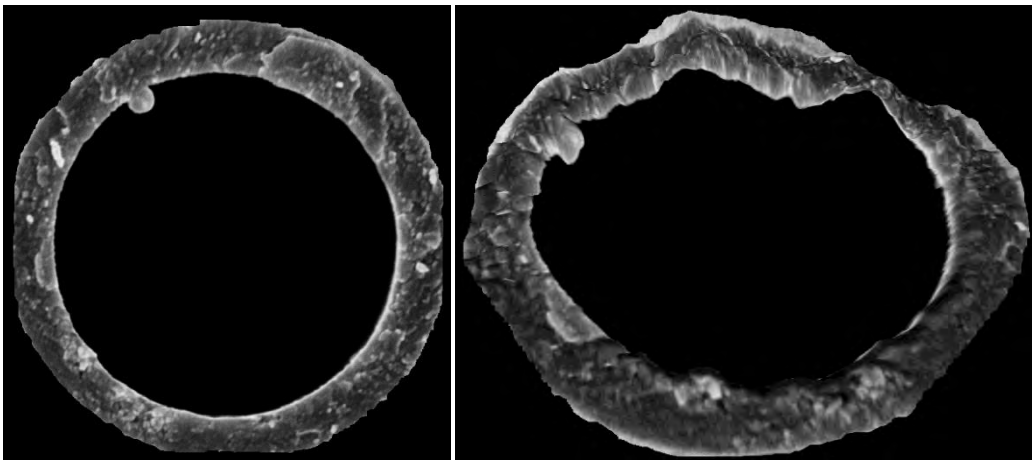

(a) (b)

Figure 5.11. Reconstructed surface of the pipette tip shown with different viewing angles, (a) top view and (b) isometric view [217].

It is revealed that the pipette tip was not only rough, but also wavy and inclined in its form. The surface parameters captured by the SEM stereo imaging are given in Table 5.3.

Table 5.3. Surface parameters of the pipette tip.

Parameter	Value	Description
$\mathbf{S_a}$	27.2 nm	Average height
$\mathbf{S_q}$	34.8 nm	Root Mean Square height
$\mathbf{S_p}$	104.5 nm	Maximum peak
$\mathbf{S_v}$	150.5 nm	Maximum valley depth

The uneven surface of the pipette tip was corrected by cutting the top of the pipette across using a FEI dual beam focused ion beam system. Details of the surface polishing can be found elsewhere [217].

Another application on surface characterisation of diatomaceous is explained in the next section.

5.6.3 Surface reconstruction of diatomaceous frustules

Diatoms are single-celled photosynthetic microorganisms. They can make most effective use of solar energy and convert it into energy-rich compounds [218]. The efficiency in photosynthesis is due to their complicated geometries and the patterns of their silica-based cell walls. It was found that diatomaceous cells devices can collect and control light efficiently [219]. They are created with three dimensional precision of tens of nanometers in a hierarchical manner and with multifunctional properties [220].

There are approximately 105 different diatom species with different architectures which are enlightening for optical, mechanical, transport properties, photonics, molecular separation, chemo- and biosensing, micro- and nanofluidics, and drug delivery [221],[222],[223],[224],[225],[226].

With the growing interest in this field, surface characterisation of diatoms has become key. However, the detailed morphological parameters, which may have profound significance both in theory and in applications are scarce. *Coscinodiscus lineatus*, one of the species of diatoms and a representative of diatoms with central symmetry, is of interest in this study.

For diatomaceous frustules' sample preparation, 2 × 2 cm^2 silicon substrates cut from single side polished silicon wafers were used. The substrates were first cleaned using ultrasonic cleaner in isopropyl alcohol for a period of 10 min to remove dust and rinsed in running deionised water for 1 min. Then, a suspension of diatom frustules was dropped onto the silicon substrate surface by means of a micropipette. The sample was ready for imaging 2 hours later.

To meet the requirements for proper imaging stated in section 5.3, a 5-nm-thick gold film was deposited on the sample surface using a sputtering evaporation system to increase the conductivity of the sample surface and enhance the image sharpness. Two sharp and high-resolution images of the sample were taken at tilt angles of -5^o and 5° by a dual beam system (Strata DB 235, FEI) at "eucentric" height with the beam energy of 30 keV as shown in Figure 5.12. Although higher titling angles may have resulted in a more accurate 3D reconstruction, experiments were associated with out-of-focus images for this particular sample because the height of the diatomaceous frustules is relatively high as illustrated in Figure 5.13. Again, the 3D rendering was performed using the MeX software package.

Volume and area are two key parameters for geometry, which can be obtained based on the 3D structure [227]. Its surface area and volume are 468.86 μm^2 are 483.94 μm^3.

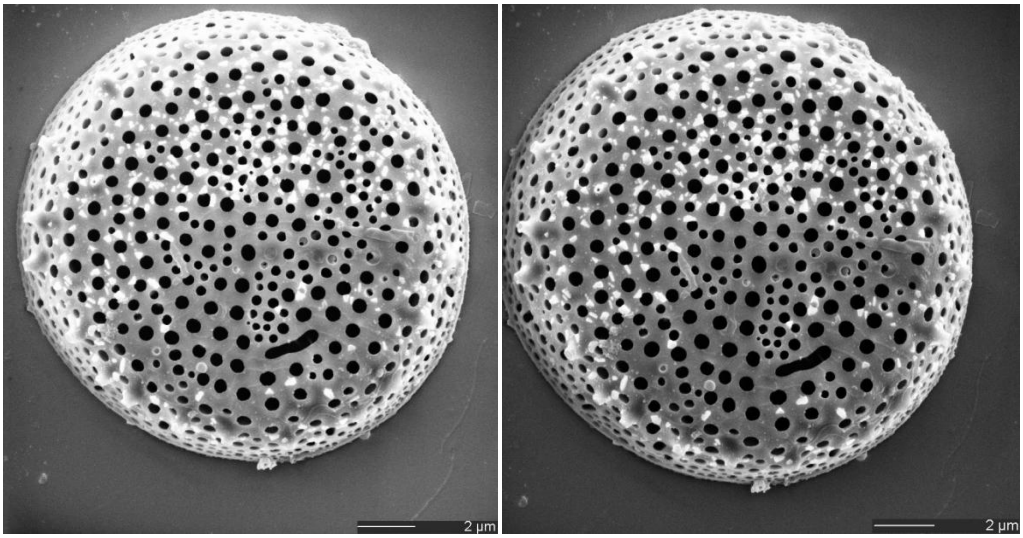

(a) (b)

Figure 5.12. Stereo images of the diatomaceous frustules for 3D reconstruction; (a) left and; (b) right.

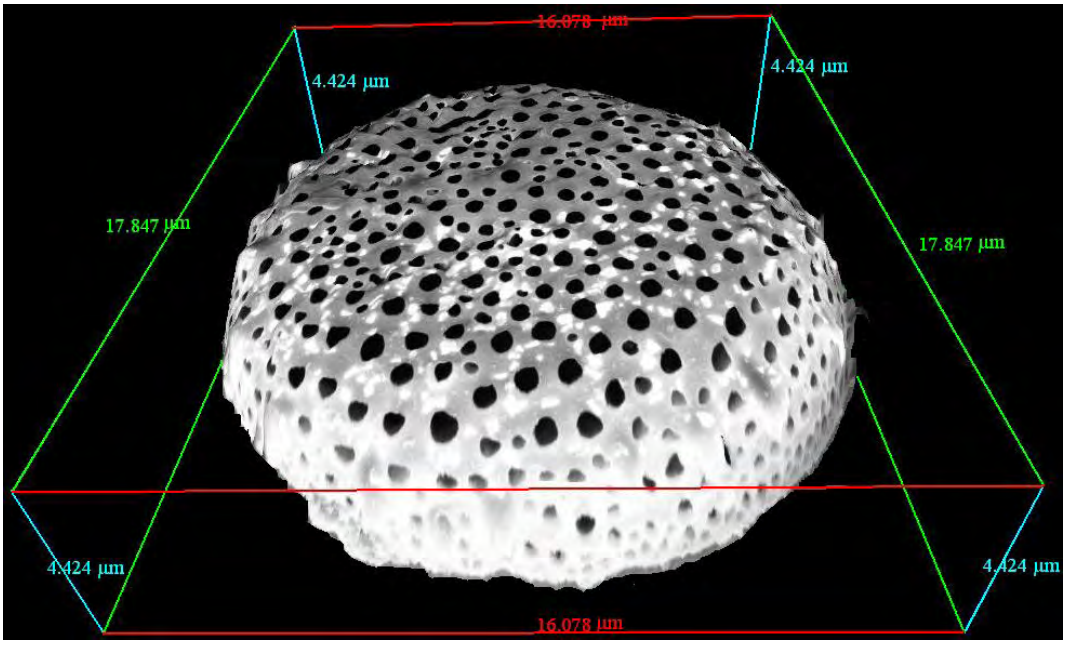

Figure 5.13. A 3D structure of diatomaceous frustules after reconstruction [227].

The proposed approach used for diatoms allows using the SEM imaging technique and commercial software, thus it is a simple way since no complex processes are involved.

The applications of SEM stereo imaging on various materials characterisation were discussed. The next section summarizes this Chapter.

5.7 SUMMARY

In this Chapter the FIB milling yield of the MPL and CL were found through the SEM stereo imaging technique. It was demonstrated that using stereo pair images, it is possible to reconstruct the milled area and calculate directly the removed volume (μm^3). By knowing the dose (nC) -which can be set by the FIB system- the sputtering yield (μm^3/ nC) was worked out. A big challenge in the measurement of the missed volume is the optimization of the tilting angle, which can be easily tuned by comparing a specified feature height and that of reconstruction. This method is accurate and valid since the sputtering yield obtained from this technique was similar to the other researches as shown in Table 5.1. The validated method then was used to characterise the MPL and CL. The removed volume (μm^3) per dose (nC) for MPL and CL samples is similar and is around 1 μm^3/nC.

The SEM stereo imaging technique was then extended to characterise urinary catheters surface, micropipette tip and diatomaceous frustules.

The technique was used to validate the results of conventional tactile measurements applied to twelve urinary catheters. It was used to reconstruct the surface features of different catheters to validate tactile measurement results. It was demonstrated that if the surface roughness and the stylus tip differ by one order of magnitude, the results of the tactile measurement may not be reliable.

The surface roughness of a pipette tip is considered to have a great influence on the seal formation as it complicates the membrane spreading along the glass surface. The surface of a typical pipette tip with the diameter of ~1.5 µm was reconstructed and the surface parameters were obtained.

Similarly the SEM stereo imaging technique was applied to characterise the surface of diatomaceous frustules. Reconstructed 3D images were used to quantitatively evaluate the specimen. Geometrical parameters including volume and area were obtained based on the 3D data. The method has potential application in theory and in experiments.

After FIB milling characterisation of the MPL and CL, it is now possible to reconstruct the 3D structure of the CL and MPL using FIB/SEM nanotomography. In the next Chapter, the MPL and CL are reconstructed and key parameters are calculated.

6 CHAPTER 6: FIB/SEM NANOTOMOGRAPHY OF MPL AND CL

6.1 INTRODUCTION

Visualization and characterisation of nano scale porous MPL and CL are vital in using the materials in the most effective way, but the pore dimensions in nanoscales pose technical challenges to accurately find the key features of the materials. This Chapter presents a FIB/SEM nanotomography approach to tackle the challenges by reconstructing 3D structures of the MPL and CL and characterising them. The resolution of the FIB/SEM nanotomography is required to be less than 20 nm. Such a high resolution imaging requires careful sample preparation. In section 6.2, sample preparation steps including Pt layer deposition, rough milling, fiducial mark milling and polishing-imaging are discussed. Then in section 6.3, the experiment carried out for 3D reconstruction of the MPL with the pixel size of 8×8×16 nm is explained. Key parameters including porosity, pore size distribution, permeability and tortuousity are predicted by analytical approaches and LB numerical modelling. Next, CL characterisation is studied. The CL porous structure characterisation requires sub 10 nm resolution images. The process of 3D reconstruction of a CL with a pixel size of 5×5×10 nm is presented in section 6.4. The LB method was applied to the nanotomography image to anticipate the permeability and flow tortuousity. In addition, FEA analysis is carried out for a throughout 2D cross-section of a CL with a pixel size of 1 nm to reveal the tortuous streamlines and calculation of effective diffusivity. In section 6.5, a number of CL samples are characterised and the porosity and average pore size were compared to that obtained by mercury porosimetry. It is believed that the FIB/SEM nanotomography technique can be applied to a wider range of applications

beyond fuel cell components and porous materials. As an attempt, this technique was used to reconstruct a tip of a micropipette for patch clamping and the roundness of a micropipette tip with a tip diameter of 1.3 µm was investigated as described in section 6.6. Finally, this Chapter is summarized in section 6.7.

6.2 FIB/SEM NANOTOMOGRAPHY PRINCIPLES

The process involved milling away a thin slice (10-20 nm) of the side-wall of a trench using FIB and recording an SEM image of the new surface, then repeatedly milling and imaging to produce a stack of SEM images as schematically shown in Figure 6.1. The process involves 5 steps: (i) deposition of protective Pt layer; (ii) rough milling or pocket milling; (iii) milling or recognizing a fiducial mark; (iv) slice and view; (v) image alignment through fiducial mark; and (vi) image binarisation and 3D reconstruction. Next, each step is described briefly.

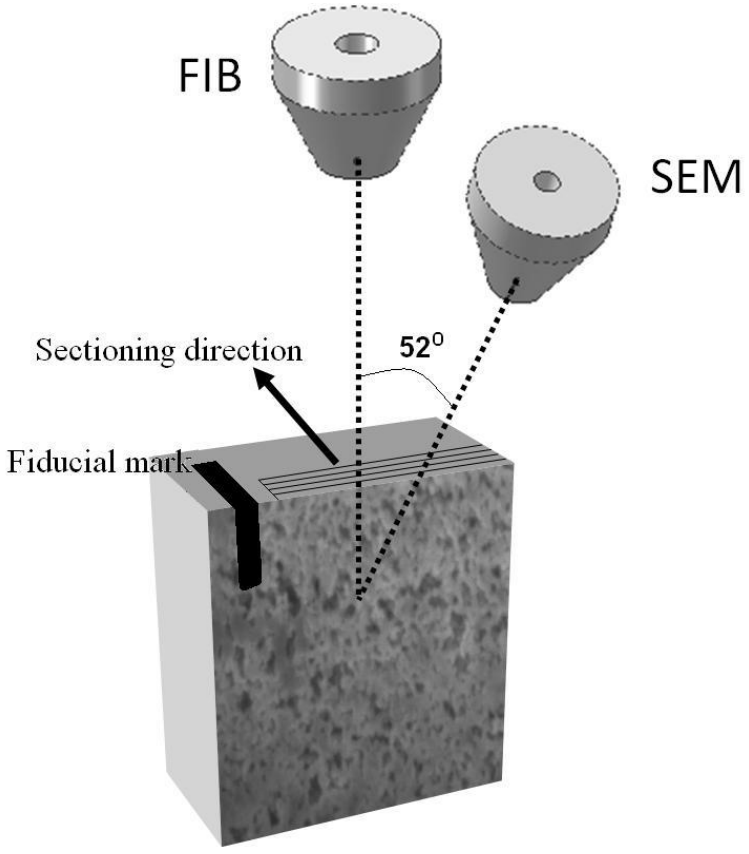

Figure 6.1. FIB/SEM and sample configuration. After milling a cube and deposit a protective layer of Pt, few hundreds of SEM images of the MPL side walls were acquired repetitively after milling thin slices of 10-20 nm thickness each. The sectioning direction is perpendicular to FIB column.

6.2.1 Deposition of protective Pt layer

The surface is usually coated by a few hundred nanometer-thick layer of platinum prior to side-wall milling in order to protect the soft surface from ion bombardment and to reduce the re-deposition effect caused by FIB-induced decomposition of the precursor gases. The Pt layer also serves to suppress the curtain effect and avoid swelling effect [184],[228]. The gas assisted FIB induced deposition process can be summarised as follows: (i) Gaseous compound precursor (methylcyclopentadienyl trimethyl platinum $C_9H_{16}Pt$) is introduced through nozzles inserted close to the surface and adsorbs on the sample surface; (ii) The gas molecules adsorbed on the surface are decomposed into nonvolatile and volatile products by the incident ion beam; (iii) The nonvolatile products remain on the surface, producing deposition layers and the volatile components leave the surface [184].

Important parameters for the Pt deposition are accelerating voltage, current, time and beam overlap parameter.

- The voltage is always set to be the highest voltage, i.e. 30 keV in the FEI DB STRATA 235, since the beam diameter decreases as the beam voltage increases. The optimum resolution is directly related to the beam diameter and the smaller beam diameter would result in a higher resolution [197].

- The beam scans the pattern from point to point. At each point, the ion beam converts the precursor gas to a deposited product then sputters material away until it passes to the next point. If the ion beam remains longer at the point the net deposition is less. Then net deposition is the deposition rate minus the sputter rate. The maximum growth rate occurs when the beam current into the pattern area is in the range of 2-6 pA/μm^2. This results in 1 μm thickness in 1 min. Therefore, the current is recommended to be around 200-5400 pA for areas of 10 × 10 - 30 × 30 μm^2 which are typically used in this work[197].

- Deposition time could be easily worked out via deposition rate of Pt for a specific area. The deposition rate has been reported to be 0.5 μm^3/nC [197].

- At each pixel, the ion beam remains for a certain period of time, namely the dwell time, and produces a deposition. Then the ion beam moves to the next pixel with a step size or beam overlap. Different beam overlap schematically is shown in Figure 6.2. Examples of different beam overlap; (a) 50% overlap; (b) 0% overlap; and; (c) -50% overlap.

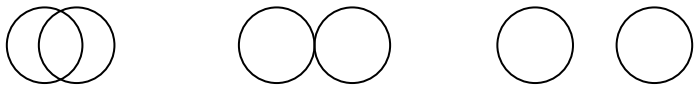

Figure 6.2. Examples of different beam overlap; (a) 50% overlap; (b) 0% overlap; and; (c) -50% overlap.

When the beam overlap is set up, the Gaussian beam profile need to be taken into account. Although the beam is digitally controlled, the Gaussian beam profile of the beam spot contributes an extra ion beam current in the space between beam spots. In general, negative and positive overlaps are used for deposition and milling respectively.

6.2.2 Rough milling of a pocket

Milling a pocket is essential to create a smooth side wall for fine polishing. A cube is milled through high ion-beam energy to create a pocket. Similar to the Pt deposition, important parameters for the rough milling are voltage, current, milling time and beam overlap parameter.

- As mentioned in section 6.2.1, the accelerating voltage should be as high as possible i.e. 30 keV to achieve the optimum resolution.

- The current needs to be high enough to remove a relatively large volume around 10×10×10 μm^3. However, soft materials are very sensitive to ion bombardment, therefore ion beam with currents higher than 500 pA would damage the surface of the sample. Figure 6.3 shows that milling with 100 pA current has less effect compared to milling with 500 pA of the CL surface sample.

- Milling time can be worked out through the milling yield of the material as discussed in section 5.5.

- Finally the beam overlap parameter is set to be a negative number i.e. -50% to achieve smoother surface

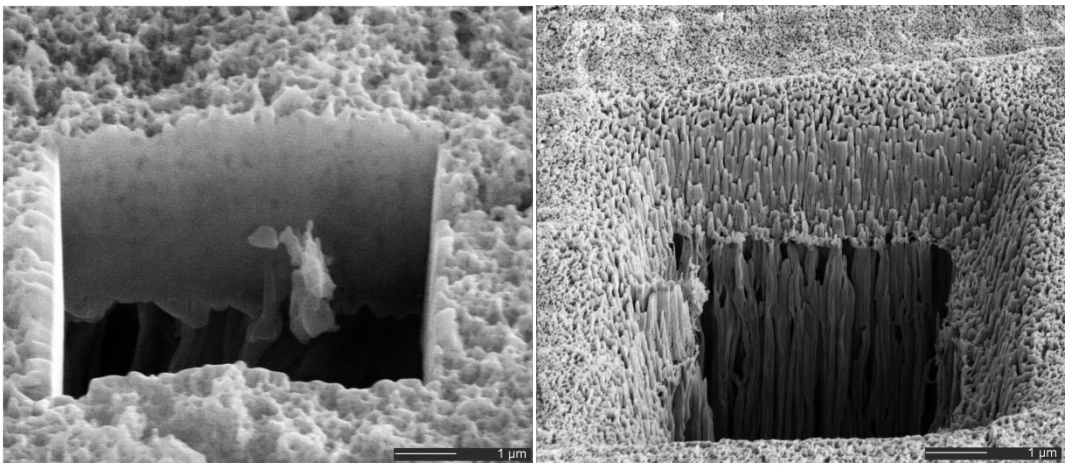

(a) (b)

Figure 6.3. Effect of ion-beam current on milling CL surface; (a) ion beam milling with 100 pA current and; (b) ion beam milling with 500 pA current.

6.2.3 Fiducial mark

The fiducial mark is a reference mark which remains similar in all 2D SEM images. The fiducial mark is necessary for SEM image fine alignment. The fiducial mark can be created through milling a particular shape, as shown in Figure 6.1, on the sample surface or

could be a particular feature of the material which has not been affected by the milling-image recording process. The fiducial mark needs to be clearly visible in all images with sharp edges for fine alignment.

6.2.4 Slice and view

After milling a trench, imaging a polished sidewall of that trench and polishing off a thin layer of material, one can continue in the same fashion, and open up a third, a fourth, etc., surface, and doing so, create a series of slices through a volume. Thin slices for soft materials can be removed from the side wall with low current ion beams of less than 50 pA. In addition to the voltage, current milling time and beam overlap parameters, thickness of slice need to be specifically taken into account. Basically, the slice thickness is the third dimension of the reconstructed volume and therefore is a key to defining the resolution of the 3D image.

Slice thickness and magnification are mainly controlled by the size of the pores/features. Ideally the slice thickness and lateral image resolution are equal and are at least five times smaller than the smallest pore/feature. In practice, lateral resolution and slice thickness of approximately 10 nm and 5 nm can be obtained respectively [13],[184]. Slice thickness is mainly dependent upon the precision of the ion beam positioning and beam drift throughout the entire process.

Although in principle there is no limit to the size of the volume that can be analyzed, practical limitations are enforced directly or indirectly by time constraints. A typical and reasonably sized dataset consists of 100–500 slices the total time that is needed to acquire such a large amount of data is from a couple of hours to tens of hours.

6.2.5 Image alignment

Through the fiducial mark, fine image alignment of the stack of SEM images is possible. One of the powerful alignment algorithms that is used in Adobe Photoshop CS3 (http://www.adobe.com) is the Lucas-Kanade algorithm [229]. It assumes that the optical flow is locally constant close to the pixel under consideration, and solves the optical flow equations for all the pixels nearby. With a matching feature, e.g. fiducial mark, the process becomes relatively easy. Images with a matched object are shifted in both x-y directions until the matched object of all the images is seen exactly in the same position. Figure 6.4 shows two sets of images. Figure 6.4a,b are the first and tenth slices of an MPL sample recorded by SEM after the polishing-recording process. The fiducial mark is the left side of the yellow line which has not been affected by the milling. The length of the yellow arrows in both images is not equal which means that there is a slight movement during SEM imaging. The problem is resolved by applying the alignment algorithm as shown in Figure 6.4c,d. The red arrows length in both figures is equal after alignment.

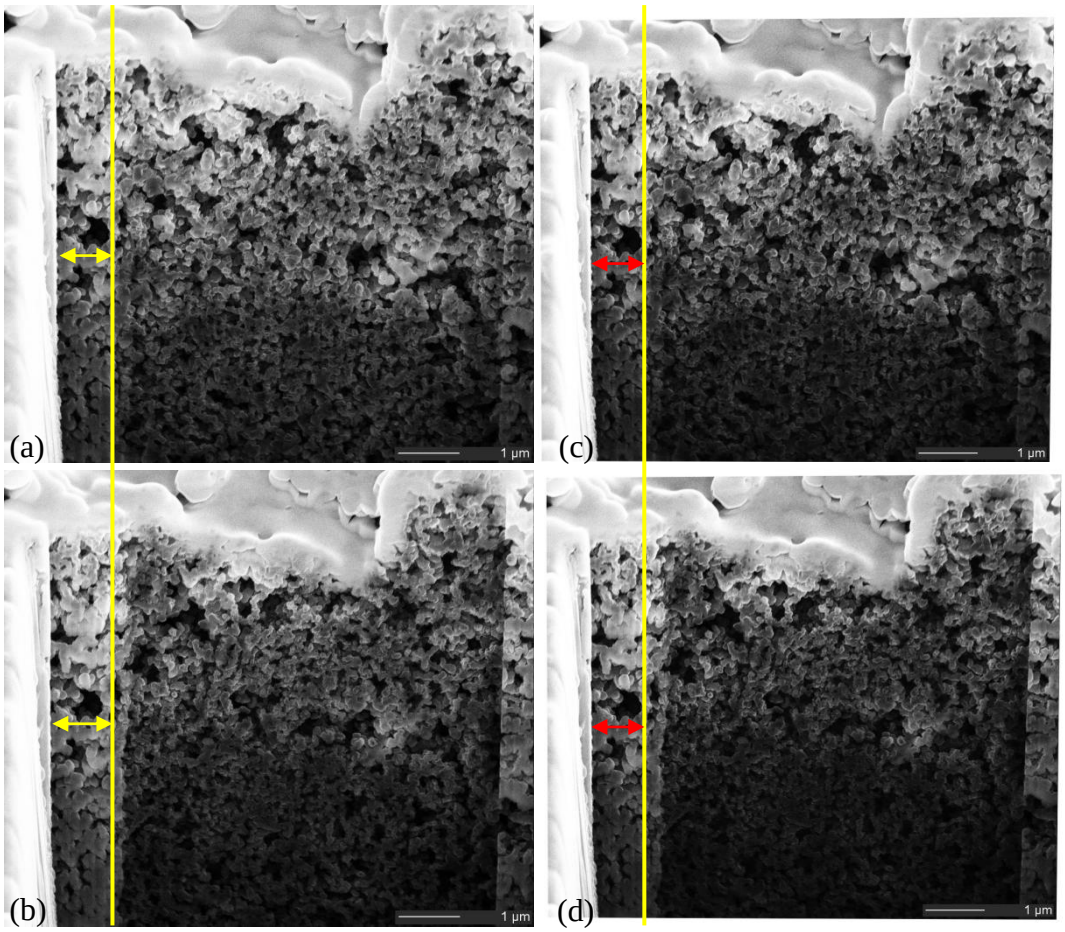

Figure 6.4. Image alignment process through fiducial mark for MPL sample. The fiducial mark is the left side of the yellow line that has not been affected by the milling process; yellow arrows are not equal in length while after the alignment process images are matched through the fiducial mark and red arrows are equal in length (a) SEM image of the first slice; (b) SEM image of the milled surface after ten slices; (c) Processed image of the first slice after alignment; (d) Processed image of the tenth slice after alignment.

The slice images are similar to the slices obtained from X-ray µCT/nCT images described in Chapter 3. Through assembling the binarised 2D slices it is possible to reconstruct the 3D object.

6.2.6 Image stretching, binarisation and 3D reconstruction

As shown in Figure 6.1, the imaging plane has a 52^{o} angle with respect to the SEM column. To compensate this angle, slices need to be vertically stretched by a factor of 1.27

(sin^{-1} *52*). For stretching an image with '*y'* pixels in a vertical direction, a linear interpolation function can be used to generate a new image matrix with '*1.27y'* pixels. A MATLAB code was developed for this purpose. The stretched images are then binarised.

Similar to the X-ray µCT/nCT grey scale slices, SEM images are grey scale. For characterisation and quick reconstruction, images need to be binarised. The Otsu's thresholding method described in section 3.4 is used in this work since the SEM images are of high resolution, sharp and high contrast. The 3D reconstruction can be carried out through the double time cubes algorithm as the same as X-ray µCT/nCT 3D reconstruction described in section 3.2 via the CTAN software package.

It should be mentioned that, if the thickness of slices are not equal to the lateral resolution, the lateral resolution should be an integer factor of slice thickness. For instance, for SEM images with a lateral resolution of 8 nm, the slice thickness should be equal or close to 8 nm, 16 nm, 24 nm and etc. However, as previously discussed, milling slices of less than 10 nm thickness is not practical. Therefore, for lateral resolution of 8 nm then slice thickness of 16 nm is practical. This resulted in a 3D image with a non-cubic voxel size of 8×8×16 nm. This means that an interpolated slice is required to correct the voxel size to 8×8×8 nm. Since there is a small change between two slices therefore, the problem can be resolved by copying one of the slices nearby and adding it into the stack of images.

This is the final step for characterisation. In the next section, 3D reconstruction of an MPL is explained.

6.3 3D RECONSTRUCTION OF MPL

The sub-micron features of the MPL require visualisation with a sub-25 nm pixel size. The FIB/SEM nanotomography experiment, 3D reconstruction and characterisation of an MPL sample are given in the following sections.

6.3.1 Experimental

A 10 µm thick developmental MPL was coated on GDL HP_30_35. The MPL coating was applied by JMFC.

For 3D reconstruction, a dual-beam FIB/SEM system (FEI Dual Beam Strata 235, FEI Company, US) has been used to obtain the 3D structure of a ~10 μm^3 sample. The process involved milling away a 16 nm slice of the side-wall of a trench using FIB and recording an SEM image of the new surface, then repeatedly milling and imaging to produce 100 SEM images. The surface (15 × 15 μm^2) was coated by a 100 nm-thick layer of platinum with the Ga^+ ion beam voltage of 30 kV and current of 500 pA prior to side-wall milling in order to protect the soft surface from ion bombardment. Each slice of the sample is milled-off with FIB Ga^+ ion beam at 30 kV and 50 pA with a dwell time of 1 µsec. A total thickness of ~1.5 µm was removed and SEM images of the slices with ~8 nm resolution were taken. The edge of the milled side wall was used as a fiducial mark to align the images. The 2D aligned images were then vertically stretched by a factor of 1.27, thresholded through Otsu algorithm and used to build a 3D binary image with 0 and 1 representing pore and solid phases respectively. The 3D reconstructions of the layer were carried out and the key properties determined similar to the GDL characterisation presented in Chapter 3 and Chapter 4.

6.3.2 Imaging results

In Figure 6.5a, the pores on the side wall, the deposited platinum on the MPL surface and the fiducial mark are shown. A 3D reconstruction of the MPL with pores (light grey) and solid phase (dark grey) are presented in Figure 6.5b. The white lines show the connectivity and tortuous pore network in the porous media.

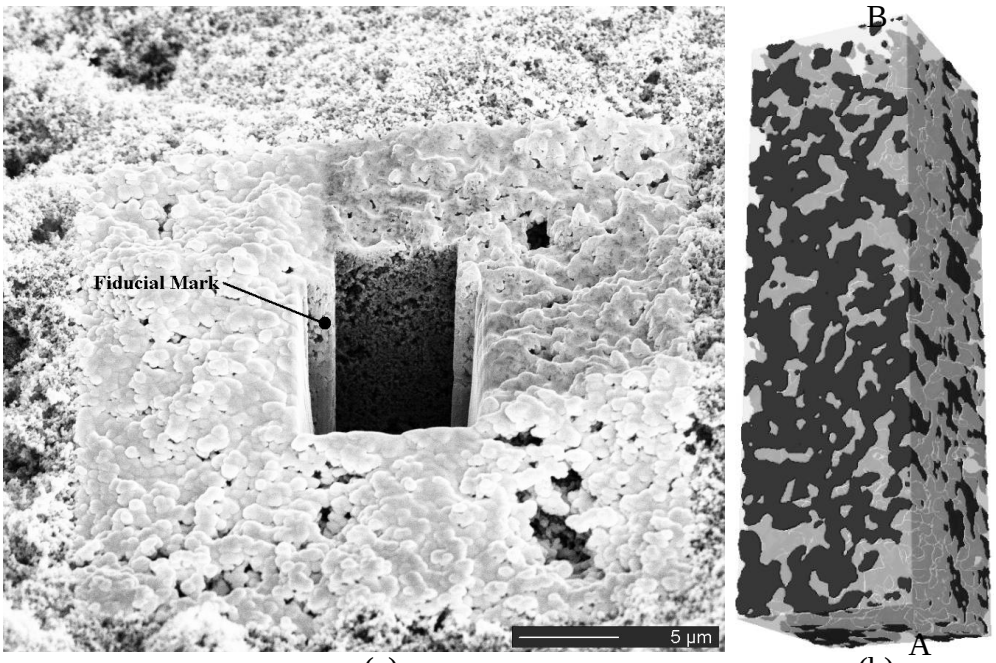

Figure 6.5. a) Low magnification SEM image of the trench side wall polished through low current 50 pA ion beam. A 25 µm× 25 µm area with 100 nm thick of platinum was deposited on the surface. The fiducial mark is used for image alignment; b) a 1.5 µm×1.5 µm× 5 µm 3D reconstructed image of the MPL with 16 nm× 8 nm×8 nm voxel size. Dark and light grey show solid and pore networks respectively. The tortuous white lines show how the pore network is interconnected [13].

6.3.3 Key parameters: structural parameters, analytical approach and LB simulation

With the digital representation of the 3D structure at hand, it is subsequently possible to determine the critical features of the assembly. The local porosity value for the MPL attained from FIB/SEM nano-tomography 3D reconstruction was 39%. The method for calculation of porosity is explained in detail in section 3.3.

Similar to the GDL characterisation method given in section 4.3.2, the local effective diffusivity of a gas D_{eff} is a function of the porosity and level of liquid water saturation in the MPL and can be estimated using the Tomadakis and Sotirchos equation [50]:

$$D_{eff} = 1.09 D_{gas} \varepsilon_B (\varepsilon_B - 0.11)^{0.785} (1-s)^2 \quad (6.1)$$

where the multiple of D_{gas} on the right hand side is referred to as the Tomadakis-Sotirchos effective diffusivity factor, K_{TS} ($K_{TS} = 1.09\ \varepsilon_B\ (\varepsilon_B - 0.11)^{0.785} (1-s)^2$). Figure 6.6 shows the dependence of K_{TS} on liquid saturation using the porosities of 39%. The gas diffusivities [26] of hydrogen, oxygen and water vapour can be determined as 114.0 mm^2/s, 34.5 mm^2/s and 30.3 mm^2/s respectively. With 50% saturation, therefore, the effective diffusivity of the gases reduces to 4.6 mm^2/s, 1.4 mm^2/s and 1.2 mm^2/s in the MPL.

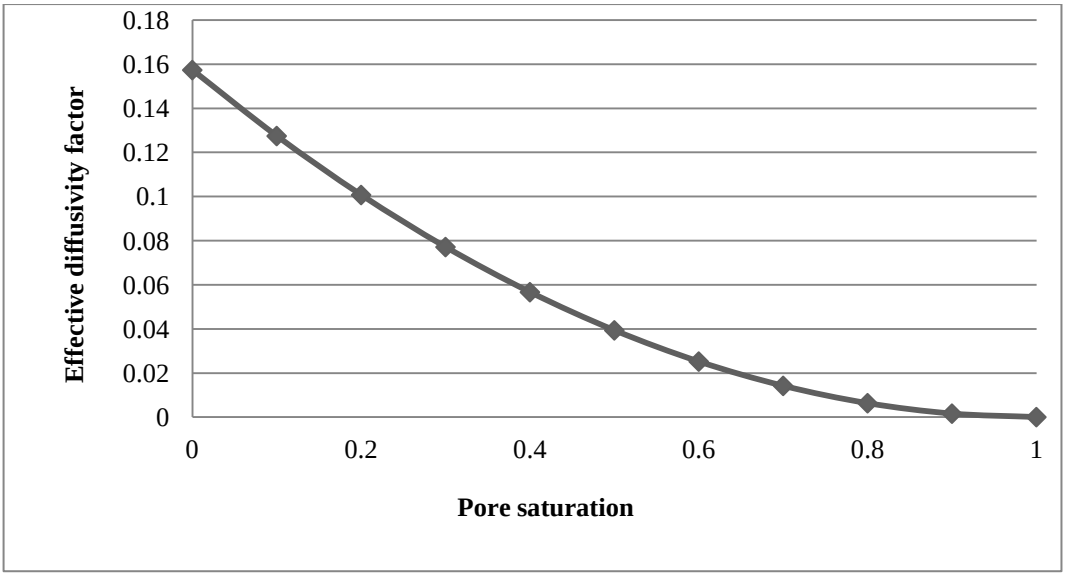

Figure 6.6. Calculated Tomodakis Sotirchos effective diffusivity factor as a function of liquid saturation for the reconstructed models of MPL. MPL porosity is 39%.

For the MPL, the determination of permeability through controlled pressure measurement drop is formidable because of the thinness of the layer (10 µm). The permeability can also be calculated using structural parameters obtained from the binary 3D model of a layer through the empirical Kozeny-Carman relation as expressed by equation (3.5). The FIB/SEM nano-tomography reveals an average agglomerate diameter of ~165 nm for the MPL and assuming that the Kozeny constant k_K is 5, the corresponding value of permeability can be calculated as 5.20×10^{-11} mm^2 which is six order of magnitude lower than that of GDL HP_30_35 given in Table 4.2 (1.86×10^{-5} mm^2).

The capillary radius ,r_C, is expressed by [26]:

$$r_C = 2\sqrt{\frac{k_G}{\varepsilon_G}} \tag{6.2}$$

where k_G and ε_G are the absolute gas permeability and gas phase porosity. The calculated permeability along with the porosity data from FIB/SEM nano-tomography results in

capillary radii of 22 nm. The corresponding value for GDL_HP_30_35 is 7.5 µm. This means that the capillary pressure from equation (2.10) ($P_C \propto 1/r_C$) in the MPL is around 300 times larger than GDL_HP_30_35 layer and may prevent any liquid from entering the MPL.

The in-plane (or off-principle flow direction from A to B in Figure 6.5b) tortuousity of the sample can be calculated through pore centroid tracking as discussed in section 3.3.1.5. Results suggest an in-plane tortuousity of 1.46. The tortuous line is shown in Figure 6.7.

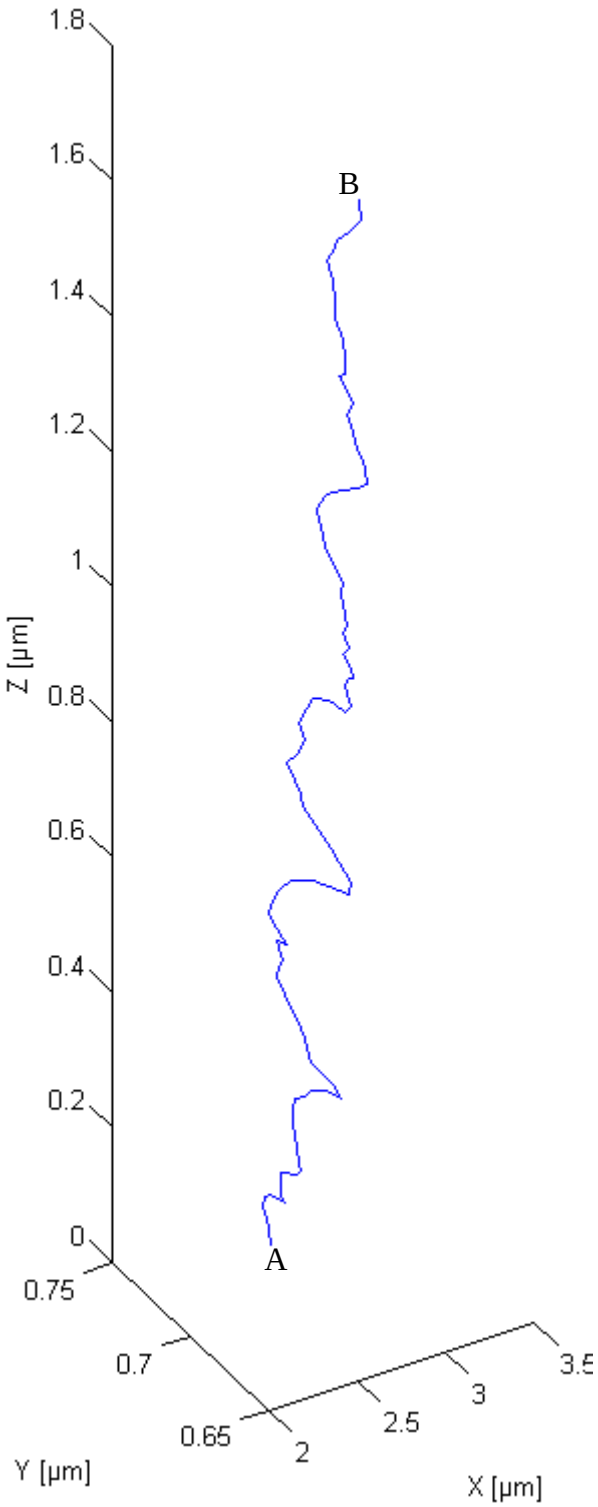

Figure 6.7. Tortuous path of the centroid tracking of MPL samples; A and B correspond to the centroid of the bottom and top surfaces A and B in Figure 6.5b.

The pore size distribution is as follows: 23% of the pores are less than 120 nm in diameter, 52% are between 120 to 220 nm and 25% are more than 220 nm in diameter as shown in Figure 6.8. The average size of the pore diameter was found as 137 nm. It has been recently found [123] that porosity-graded MPL can result in improved electrode process of the fuel cell reaction in comparison with those with conventional homogeneous MPL, particularly at high current densities. This may be caused by facilitating the transportation of water in the large pores and diffusion of gas through small pores.

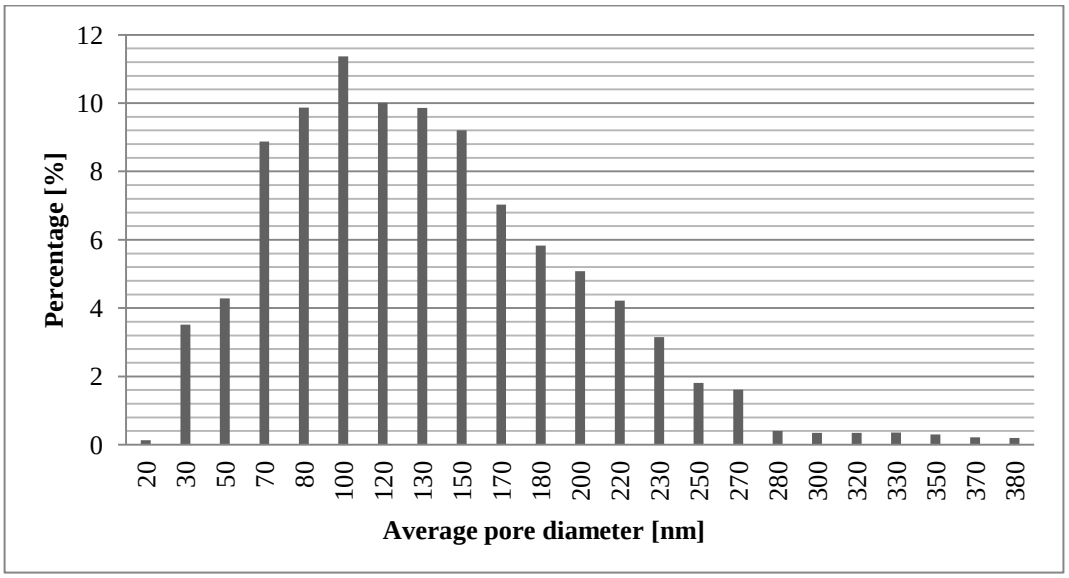

Figure 6.8. Pore size distribution in MPL based on FIB/SEM nanotomography

Since that the average pore size in the MPL is larger than 100 nm, both Stefan-Maxwell diffusion and Knudsen diffusion can occur. Effective diffusion coefficient ε_G/τ_G based on equation (3.3) can be calculated by porosity and tortuousity obtained from tomography images as 0.27. According to equation (3.4), the Knudsen diffusion coefficient in the MPL, is a linear function of the mean pore radius. Hence, the Knudsen diffusion coefficient of the MPL is calculated as 0.5 cm^2/s.

The final part of this section focuses on the application of a numerical technique to further-examine the structural properties of the layer and single-phase fluidic properties. This was conducted through the application of the LB numerical solver, explained in section 3.3.2, to simulate single-phase flow through the porous network of the layer and calculate the permeability and tortuousity of the MPL.

In this study, the lattice is taken directly as the binary 3D image of the MPL sample of 2.7 μm^3 and the simulation is carried out in the D3Q19 scheme which simulates 3D flow by considering 19 velocities originating from each point in the lattice. The simulated permeability in the through-plane direction is determined as 5.44×10^{-10} mm^2. The simulated permeability in the off-principal in plane directions is calculated as 8.99×10^{-12} mm^2 and 2.70×10^{-11} mm^2 resulting in an RMS off-principal value of 2.01×10^{-11} mm^2. The calculated through-plane permeability is one order of magnitude greater than that suggested by the Carman-Kozeny equation when the Kozeny constant is assumed to hold a value of 5. The literature does not explicate an understanding of what value the Kozeny constant should hold for MPL materials. However, the literature suggests that the Kozeny constant can depart from the commonly assigned value of 5 and decrease to less than unity as the interconnectivity and porous structure of the material becomes increasingly complex [228]. As such, the current study suggests that the exact figure of 5.44×10^{-10} mm^2 as obtained from the through-plane LB simulation can be achieved from the Kozeny-Carman equation when the Kozeny constant is set equal to 0.48. On a similar note, the LB calculations suggest that the permeability in the through-plane direction is one order of magnitude greater than the RMS value of the in-plane directions. The results therefore suggest that the MPL is preferentially structured to allow flow to propagate in the through-plane direction. The LB results also show that the through-plane permeability is 5 orders of magnitude lower in the MPL than in the GDL HP_30_35 given in Table 4.2.

The LB simulation suggests that the tortuousity of the MPL in the principal flow direction is 1.36, and 1.53 and 1.60 in the two off-principal directions. The results suggest that the toruousity is 13% less in the principal through-plane direction in comparison to the RMS tortuousity in the off-principal directions. Also the average off-principal tortuousity, 1.56, is only 7% larger than 1.46 obtained from centroid tracking analysis and therefore both are in good agreement.

Figure 6.9 illustrates the flow paths in the principal through plane and the two off-principal directions through the MPL. The difference in tortuousity can be confirmed by closely examining the linearity of the flow paths in Figure 6.9a compared to Figure 6.9b and Figure 6.9c.

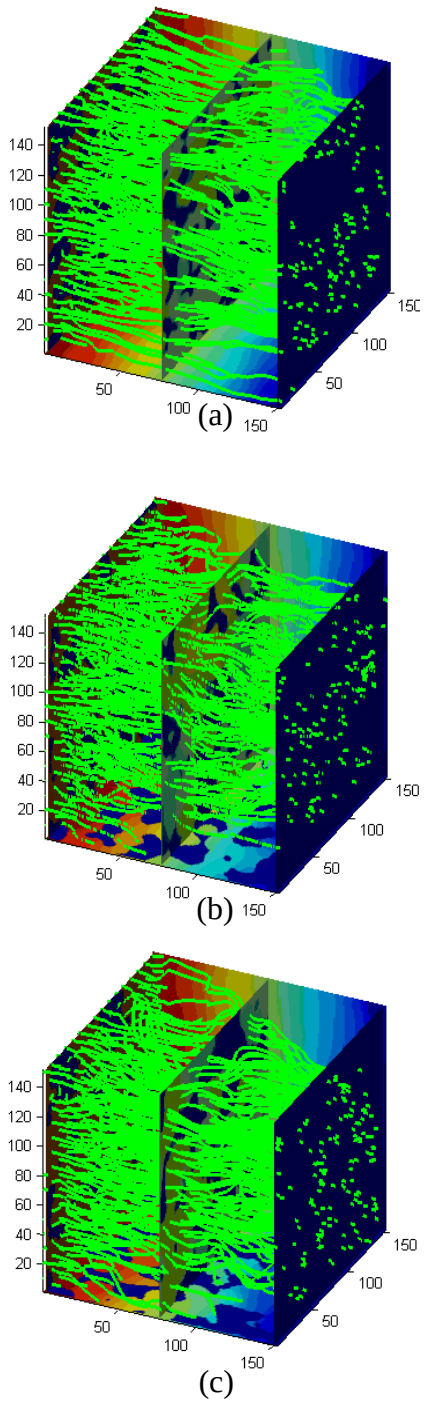

Figure 6.9. Tortuous flow paths simulated by the single-phase D3Q19 LB numerical solver in three planes. Units are in pixel and each pixel is 8 nm. The green lines are the paths along which the gas diffuses. The background colour is the gas concentration which decreases from red to blue. Gas flows from the left to the right in each image and a) shows the principal flow direction; b) shows the first off-principal direction; c) shows the second off-principal direction (This image has been produced by the University of Liverpool and Loughborough University) [13].

The current study demonstrates that the actual 3D structure of the fuel cell MPL can be captured through FIB/SEM nanotomography. It has been successfully demonstrated that key structural data can be generated using the 3D model such as average fibre diameter and pore size distribution. The effective diffusivity, absolute permeability and characteristic capillary radii have also been obtained from directly-measured data from the 3D model. The LB numerical solver is subsequently applied to simulate the permeability of the MPL. The simulated permeability of the MPL suggests that the Kozeny constant for this layer is less than unity. The LB numerical solver is also applied to visualise the tortuousity of the flow paths through the MPL.

Next, characterisation of porous CL is discussed.

6.4 3D RECONSTRUCTION OF CL

This section presents a study to obtain the nanostructural information of the catalyst layer with a sub 10 nm pixel size by using a dual beam focused-ion-beam scanning electron microscopy (FIB/SEM) nanotomography system. FEA and numerical LB flow simulation are combined with the nanotomography images to anticipate the tortuousity and permeability of gases through the porous layer.

6.4.1 Experimental

A typical PEFC catalyst layer supplied by JMFC (Company code: catalyst layer V1 anode) consisting of carbon supported platinum and ionomer was used for this study with a platinum loading of 0.45 mg/cm^2 (0.21 μm^3/μm^2) and a porosity of 40%.

In the current study, the FIB/SEM nanotomography was used to obtain the 3D structure of four samples of PEFC-CL with a pixel size of sub-10 nm. The process involves milling away a thin slice (10 nm) side wall of a trench using a FIB and recording an SEM image of

the new 2D surface. The milling and imaging is then carried out repeatedly to produce a stack of SEM images. The surface is initially coated by a 100 nm thick platinum layer in order to protect the soft surface from the ion bombardment and reduce the re-deposition effect using FIB-induced decomposition of precursor gases. A cubic fiducial mark is then milled for image alignment. Next, each slice of the sample is milled-off using a Ga^+ ion beam at 30 kV and low current (30 pA) with a dwell time of 1 µsecond and overlap parameters of 50% via FEI DB Strata 235 system. One hundred slices with a total thickness of 1 µm are removed and SEM images of the slices with a pixel size of around 5 nm are taken. Images then have been stretched by factor of 1.27 and binarised using Otsu's algorithm method. 3D reconstruction of the layer is carried out in order to study the key nano-structural and mass transport properties.

6.4.2 Imaging results

Figure 6.1 shows the principle of the dual-beam FIB/SEM system and sample configuration. In Figure 6.10, pores on the side wall, the platinum deposited on the catalyst layer surface and the fiducial mark are all clearly identifiable. The image is taken at 45^{o} tilt-angle.

Figure 6.10. Low magnification SEM image of the trench side wall polished through low current 30 pA ion beam, Pt deposited area and milled cubic fiducial mark.

A 3D reconstruction of the cathode CL with pores (blue), solid phase (transparent green) and the platinum deposits greater than 5 nm in diameter (red) is illustrated in Figure 6.11. The dark green lines show the connectivity and tortuous pore network in the porous medium.

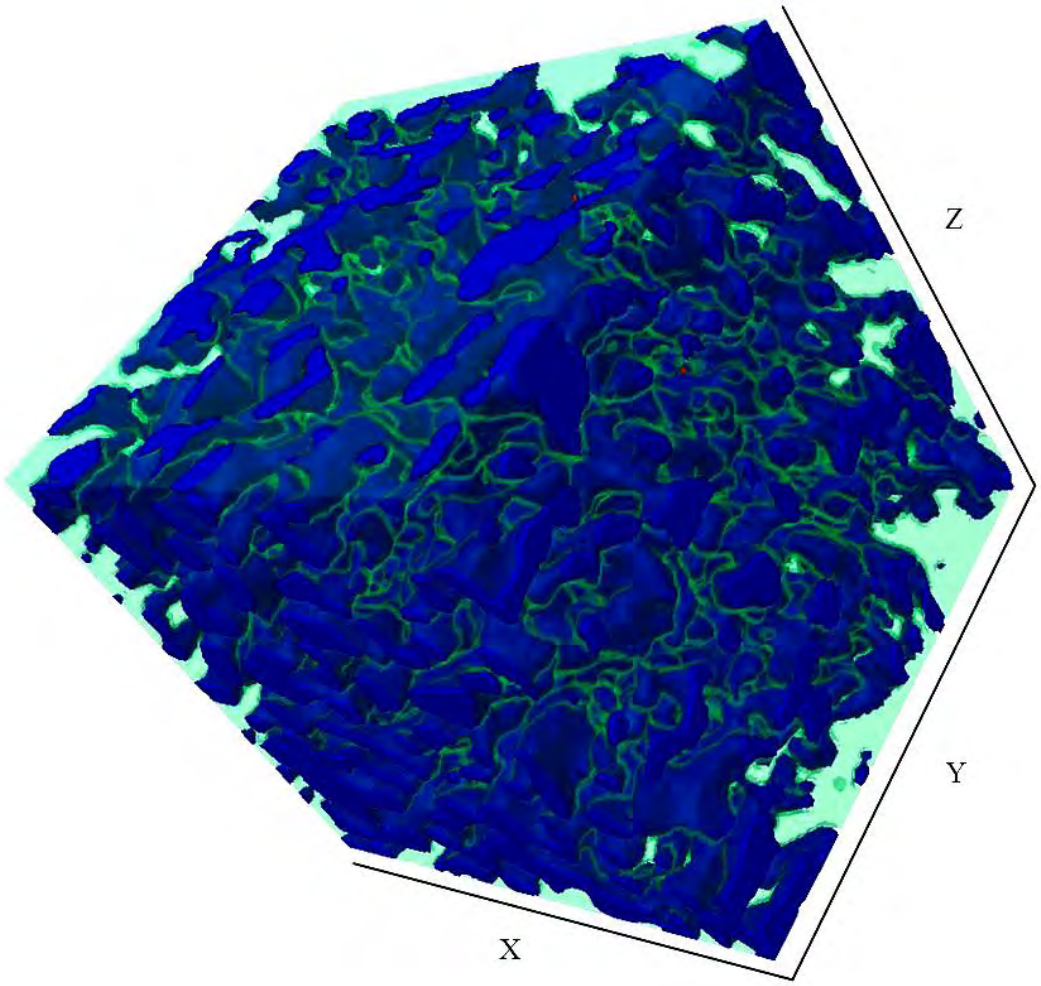

Figure 6.11. A 3D reconstruction of a mesoporous CL. Each side of the cube is 1 µm. This image has a 5×5×10 nm (X,Y,Z) pixel size. The blue colour, transparent green and red represent the pore phase, the solid phase and the platinum particles larger than 5 nm.

6.4.3 Key parameters: structural parameters and analytical approach

The digital images reconstructed in this study show that the porosity of the CL is 36%. The FIB nanotomography confirms a pore size distribution model peaking at 20, 40 and 60 nm as shown in Figure 6.12. In terms of distribution, 39% of the pores are in the range of 20-60 nm and 45% are between 60-150 nm. The reconstructed structure of the CL also reveals that the characteristic mean pore radii and the characteristic mean pore-pore lengths

are 55 nm to 78 nm respectively. The mean aspect ratio (mean pore-pore length/mean pore radius) is found to be 1.41.

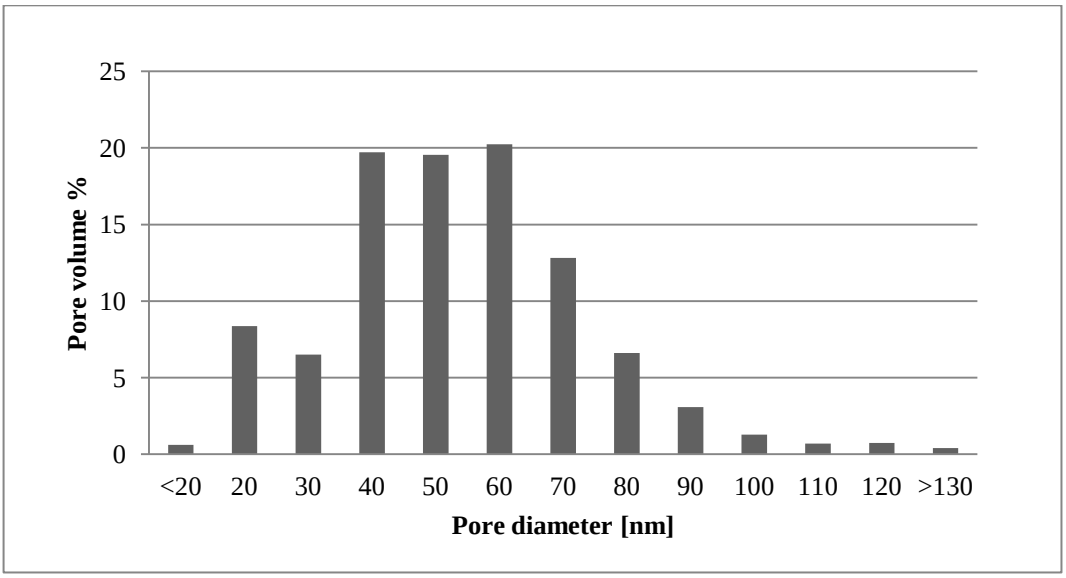

Figure 6.12. Pore size distribution of a CL, acquired from the analysis of the digital model generated using the FIB/SEM nanotomography process.

Using the structural information from the FIB/SEM nanotomography reconstruction, it is possible to elucidate certain transport mechanism and transport properties of the CL. As discussed in Chapter 2, Knudsen diffusion is a mode of transport where the likelihood of molecular-wall interactions exceed that of inter-molecular interactions due to the restrictive diameter of the pore wall and can occur in systems where the mean pore diameter is of the order of 10 nm. The characteristic mean pore diameter of 55 nm confirms that the Knudsen regime is dominant in CL structures. The Knudsen diffusion coefficient can be calculated through equation (3.4). As such, the Knudsen diffusion is calculated as 0.20 cm^2/s.

Similar to the MPL characterisation explained in section 6.3.3, the in-plane tortuousity using centroid tracking has been obtained as 2.02.

6.4.4 Key parameters: LB simulation

Similar to the MPL characterisation, simulation was conducted through the application of the LB numerical solver, explained in section 3.3.2, to simulate single-phase flow through the porous network of the layer and calculate the permeability and tortuousity of the CL.

The numerical results of the lattice Boltzmann numerical flow simulation demonstrates that the absolute permeability of air in the through-plane direction of the CL is 7.26×10^{-12} mm^2. The RMS permeability in the off-principle in-plane directions was calculated as 3.66×10^{-13} mm^2. The respective RMS in-plane permeabilities are one order of magnitude less than the through-plane value, which indicates that the structure of the catalyst layer can enable transverse flow to occur even though the principle pressure gradient is applied in the through-plane direction. Figure 6.13 depicts the dominant stream tubes along which the flow travels through the CL sample.

The lattice Boltzmann simulation also indicates that the tortuousity of the porous network through flow direction would be 3.07. The two off-principle flow direction tortuousity have been calculated as 2.23 and 2.41 and the average is 2.27. The average tortuousity is in good agreement with centroid tracking tortuousity and there is only 9% difference between both methods.

LB simulation was successfully combined with the 3D tomographic image of a CL. Due to the tiny pore sizes of the catalyst layer, the largest volume that could be reconstructed was only around 1 μm^3. This gives only information about the very top surface of the catalyst layer. In the next section a through 2D cross section of a CL is captured, binarised and meshed. Then effective diffusivity and flow streamlines through the cross section are revealed via FEA analysis.

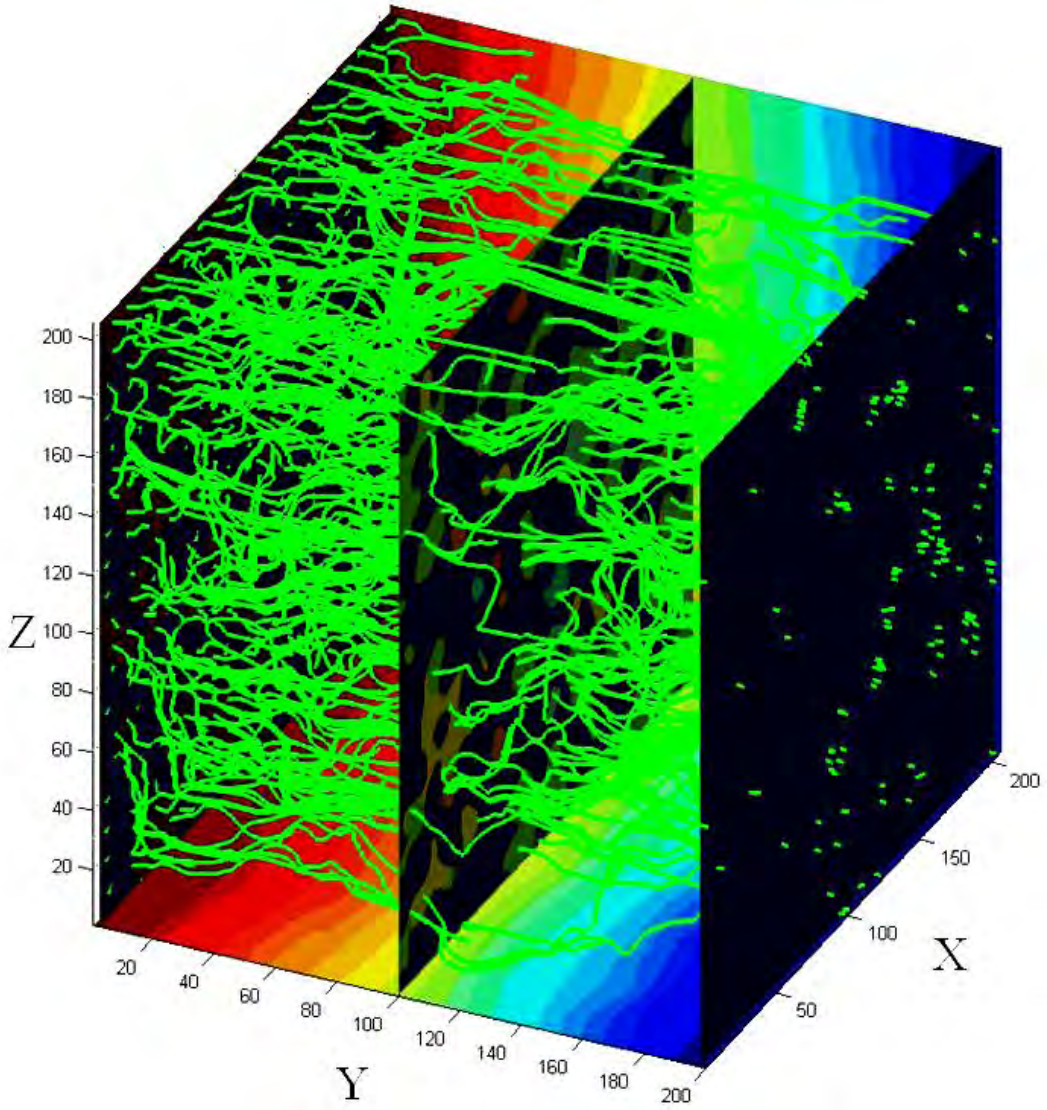

Figure 6.13. 3D representation of simulated stream tubes through the CL sample. Each side of the cube is ~1 μm with 200 pixels. The green lines are the paths along which the gas diffuses. The background colour is the gas concentration which decreases from red to blue. Gas flows from the left to the right (This image has been produced by the University of Liverpool and Loughbrough University).

6.4.5 Key parameters: 2D FE analysis

The first step in the process is to get a through 2D image of a CL cross section. The second step involves image binarisation and import the binarised image into FEA software. The third and final step is to reveal the streamlines within the porous media to calculate the tortuousity and effective diffusivity of the CL through the cross section.

6.4.5.1 Sample preparation and image processing

A thin CL provided by JMFC (Company code: catalyst layer V3 anode) with thickness of less than 3 μm was chosen. Then similar to the sample preparation for FIB/SEM nanotomography presented in the previous section, the surface was coated with a 100 nm protective Pt layer. Then a pocket was milled. The side wall of the pocket was polished with 30 pA at 30 keV through Ga^+ ions with the dwell time of 1 μsec as shown in Figure 6.14.

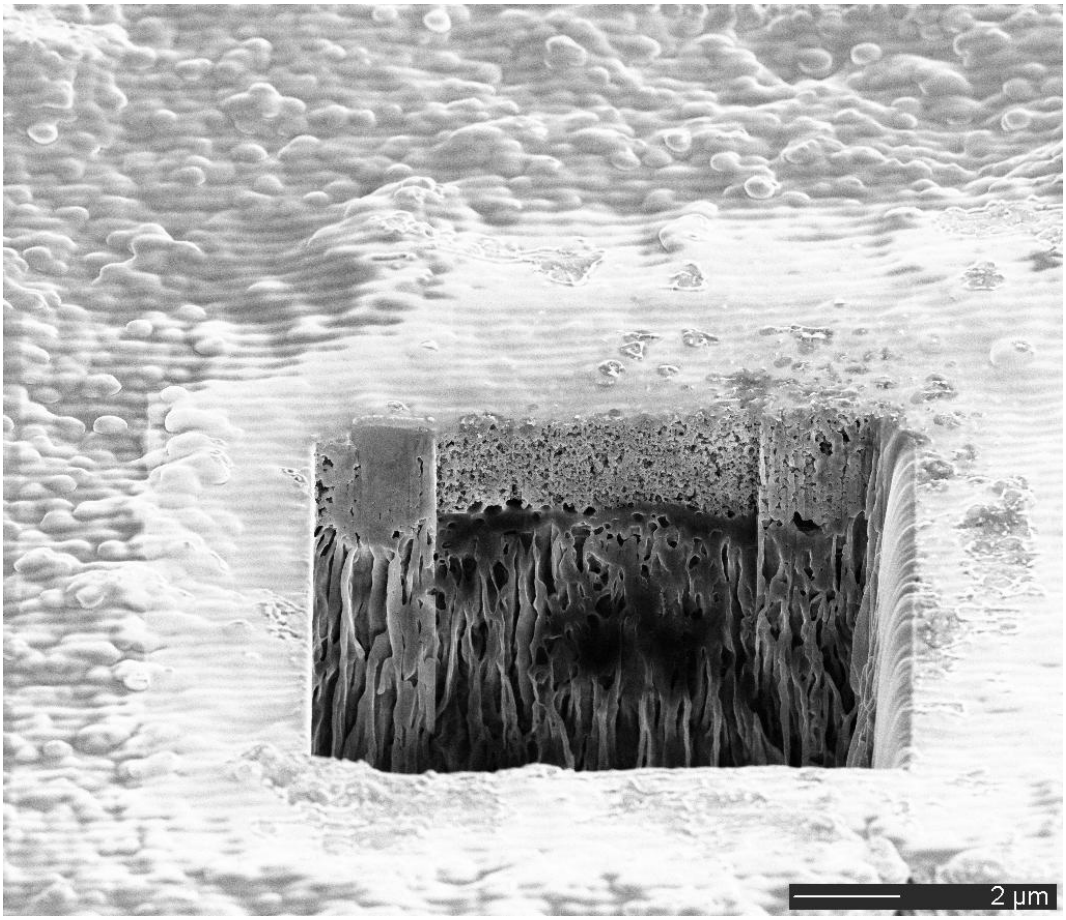

Figure 6.14. Low magnification SEM image of the trench side wall polished through low current 30 pA ion beam, Pt deposited area and milled.

From the top to the bottom of the CL, 3 images each with a 1 µm step, 1 nm pixel size at an imaging angle of 52^{o} were taken and assembled. The image has been stretched by a factor of 1.27 to compensate the projection angle. Results are shown in Figure 6.15 similar to Figure 2.7.

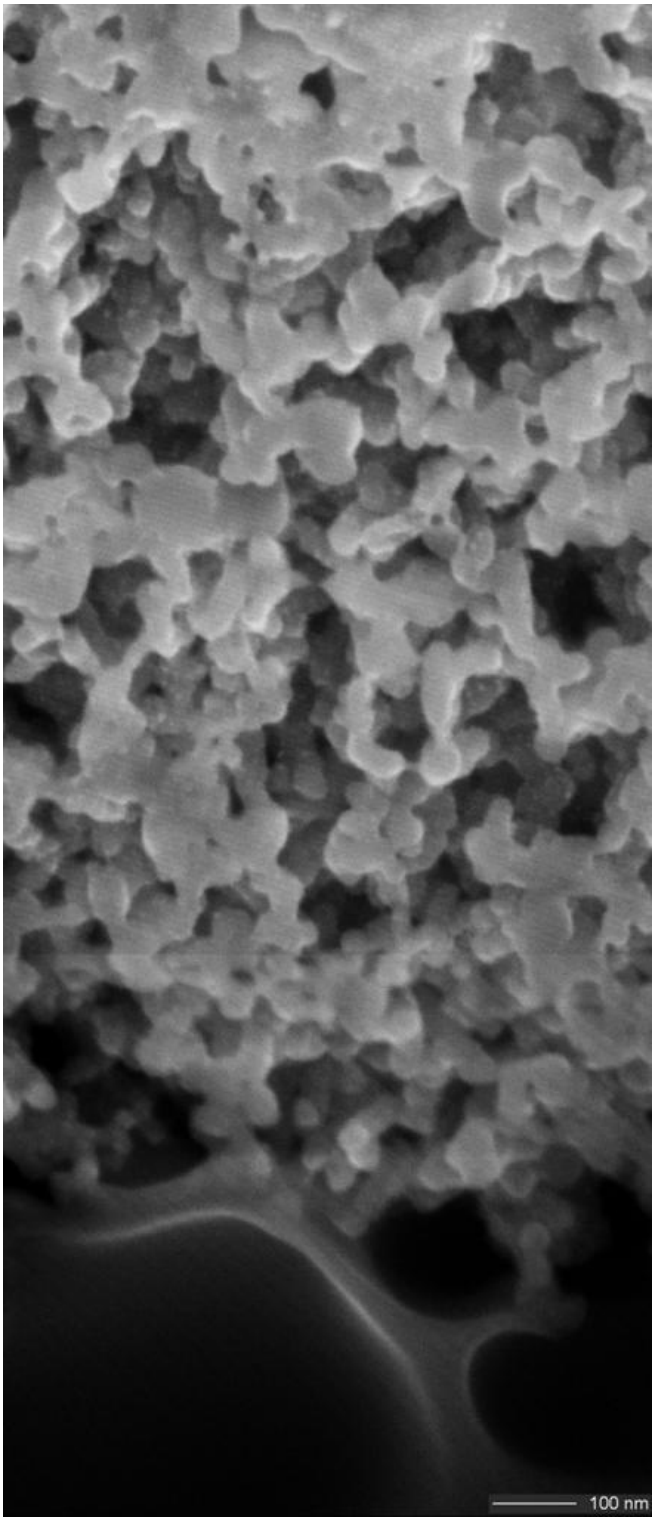

Figure 6.15. Assembled 3 SEM images of the polished side wall of throughout cross section of the CL.

The top surface was then cropped since it was coated by Pt which subsequently blocks surface pores. The PEM at the bottom of the image was also removed. The cropped images was then thresholded through Otsu algorithm, the results of which are shown in Figure 6.16.

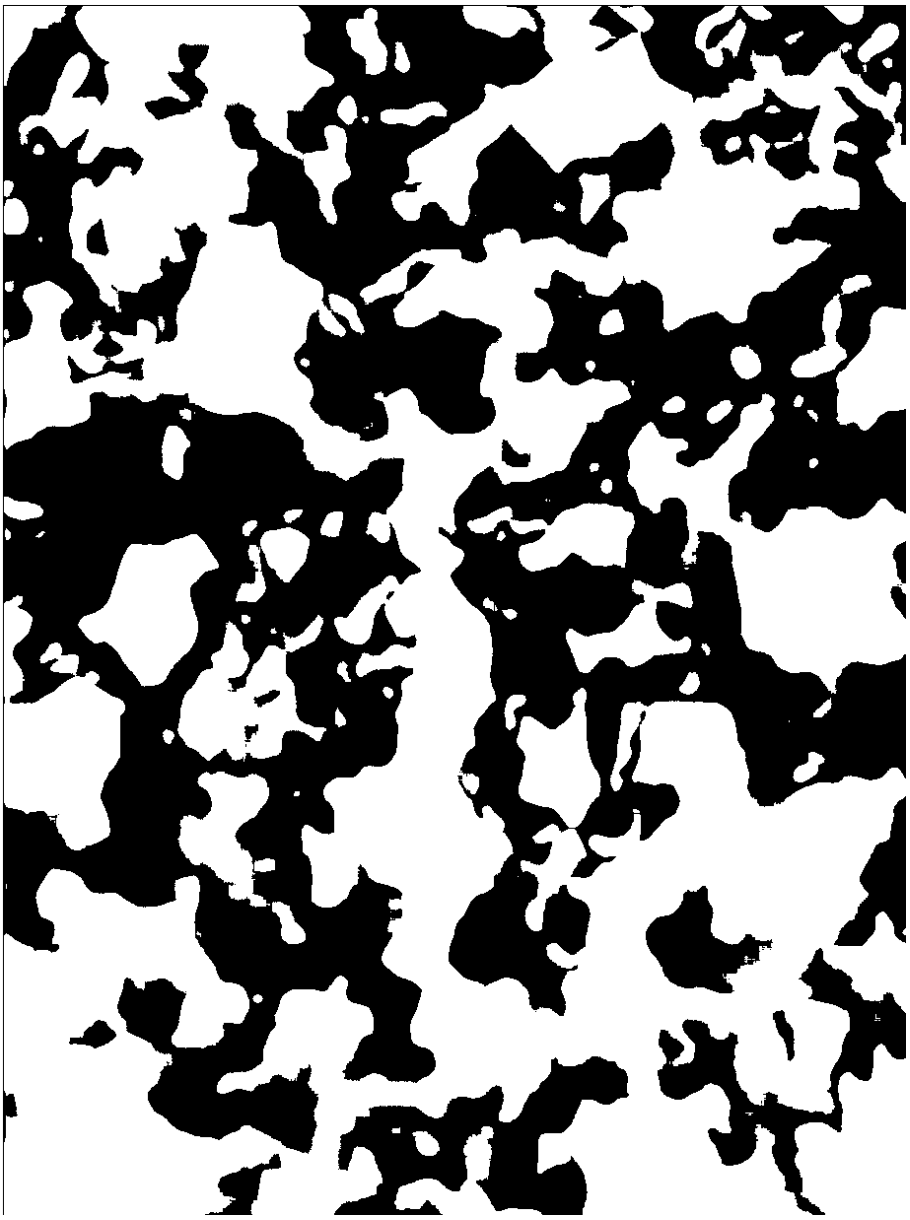

Figure 6.16. Binarised image of the cropped image of Figure 6.15. Pore network is shown in a white colour.

There are many closed pores that do not contribute to fluid flow transport from the top to the bottom of the CL sample. The white pores in Figure 6.17 are closed while the grey region shows the largest interconnected pore allows the fluid to pass through the CL. Therefore, white region can be removed to facilitate FE analysis.

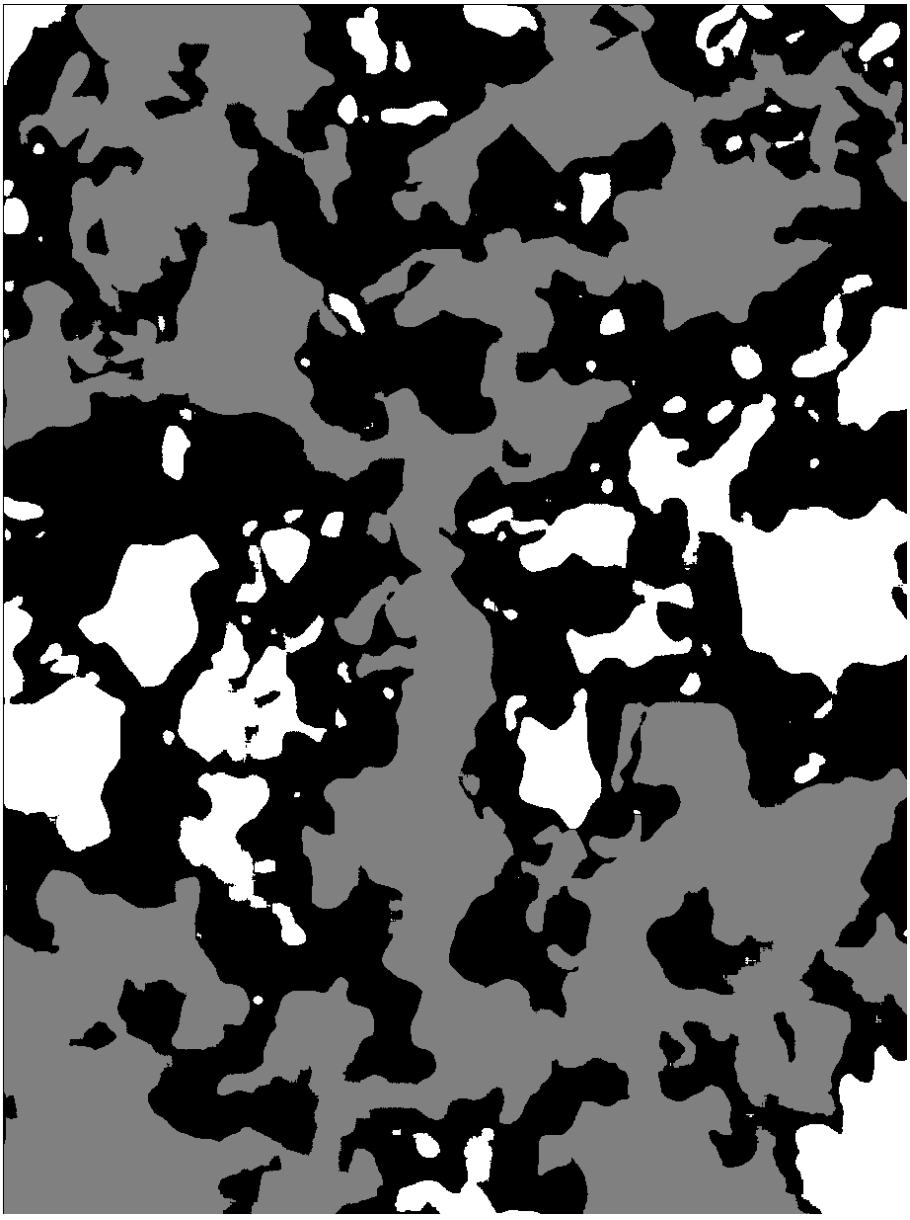

Figure 6.17. Largest interconnected pore of Figure 6.16 is shown in grey. White pores are not connected to this network, therefore they do not participate in fluid flow from top to the bottom of the surface of the CL.

The image, i.e. the grey region, were imported to a CAD file using the image2cad software package (http://www.cadtool.net/image2cad.htm). The CAD file is used for FE analysis.

6.4.5.2 FE analysis

The effective diffusivity D_{eff} is a function of tortuousity τ, porosity ε, and diffusivity D,:

$$D_{eff} = D\varepsilon^{\tau} \tag{6.3}$$

As a first approximation it is assumed that the domain can be described through the diffusion equation (6.4).

$$\frac{\partial c}{\partial t} + \nabla \cdot (-D\nabla c) = 0 \tag{6.4}$$

where ε and c are the medium porosity and concentration.

The equation was solved through COMSOL 3.4 (http://www.comsol.com/) convection and diffusion module with the following boundary conditions.

A constant boundary condition $c=c_o$ is set to the top surface of Figure 6.17 while for the bottom, the concentration can be written as:

$$-D\nabla c = k_m(c - c_1) \tag{6.5}$$

where k_m and c_1 are the mass transfer coefficient and concentration outside of the porous structure. All other boundaries are insulated and defined as follows:

$$-D\nabla c = 0 \tag{6.6}$$

The initial condition is given by an exponential profile as below:

$$c(t_o) = c_o e^{-Ax^2} \tag{6.7}$$

where A is constant.

It is noteworthy that the streamline does not change with variation of c_o, k_m, D, and A. The resultant tortuous streamline with $A=1000$, $D=10^{-5}$ m^2/s, $k_m=1$ m/s, $c_o=1$ mol/m^3 are shown in a red colour in Figure 6.18.

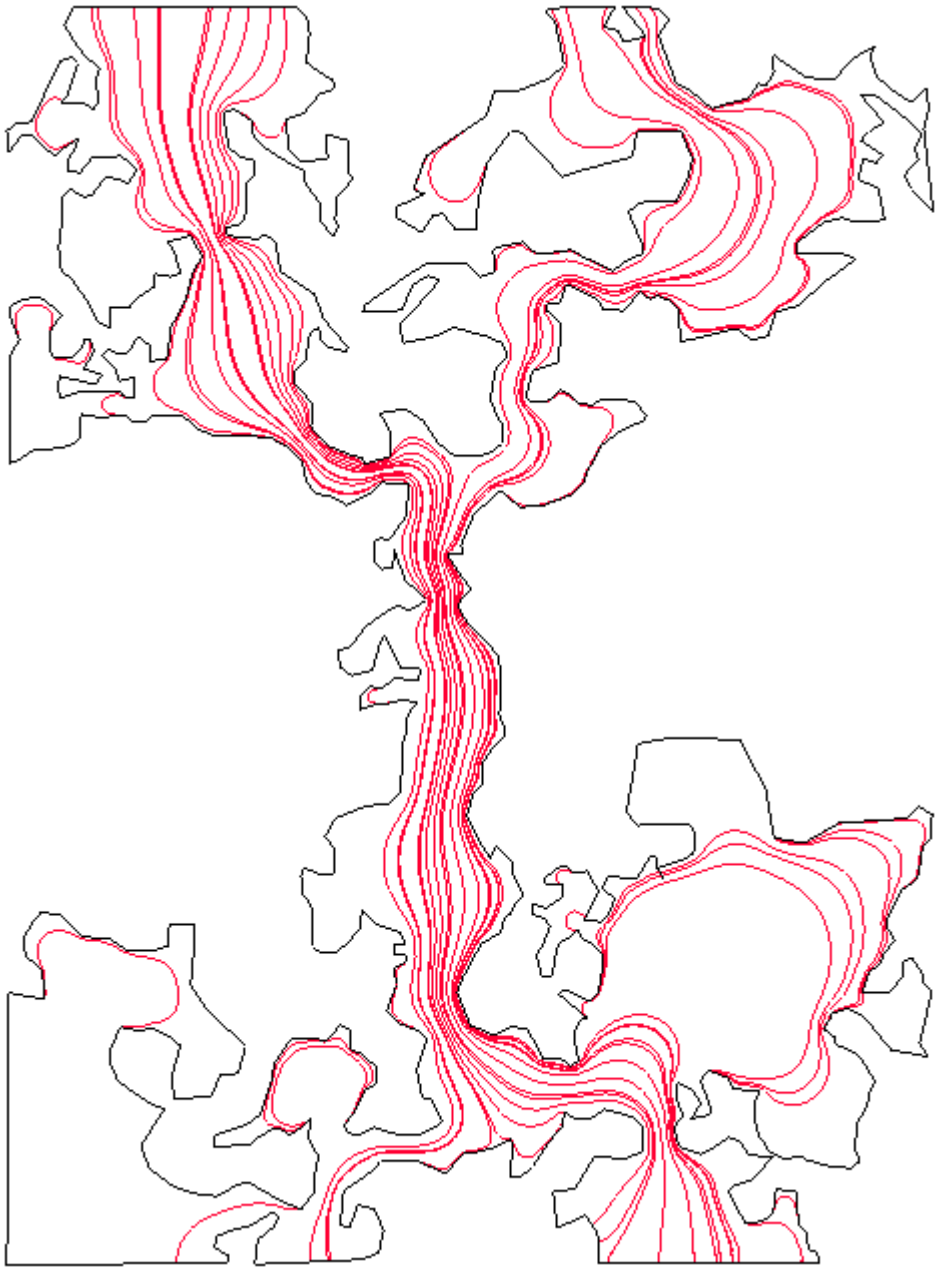

Figure 6.18. Streamline plot from top surface of the catalyst layer to the bottom using COMSOL software package.

The streamline toruousity was then calculated based on the average length of the streamlines divided by the distance between the top and bottom of the CL layer shown in Figure 6.17. In this case the tortuousity was calculated as 1.52. With the porosity of 40% and tortuousity of 1.52 then the ε^{τ} would be 0.25. Using equation (6.3) the D_{eff} is then equal to 2.5×10^{-6} m^2/s.

6.5 MERCURY POROSIMETRY AND 3D RECONSTRUCTION OF A NUMBER OF CL

Four samples provided by JMFC (Company codes: V1 anode, V4 anode, V4 cathode and V5 cathode) were characterised through FIB/SEM nanotomography. 3D reconstructed images and key parameters including porosity and average pore size were obtained. In addition to FIB/SEM analysis, the porosity and average pore size were measured using mercury intrusion porosimetry (Autopore IV, Micromeritics Instruments). Mercury intrusion porosimetry measures the specific pore volume and pore sizes ranging from 3 nm to 300 µm. The sample for measurement was prepared from the membrane with the catalyst layer on it. A 1×1 cm^2 of each sample was characterised through the mercury porosimetry by the JMFC established in-house method.

Similar to the V1 anode 3D reconstruction presented in section 6.4, FIB/SEM nanotomography of V4 anode, V4 cathode and V5 cathode with 5×5×10 nm voxel size was carried out and the porosity and average pore size were obtained. Table 6.1 summarizes the porosity and average pore size attained from both methods. Figure 6.19 shows the 3D reconstruction of CL samples.

Table 6.1. Porosity and average pore size of four CL obtained from FIB/SEM nanotomography and mercury porosimetry

	FIB/SEM Porosity [%]	**FIB/SEM Average pore size [nm]**	**Mercury Porosity [%]**	**Mercury Average pore size [nm]**
V1 anode	40	55	55	35
V5 cathode	31	50	46	34
V4 cathode	33	109	43	31
V4 anode	29	63	31	28

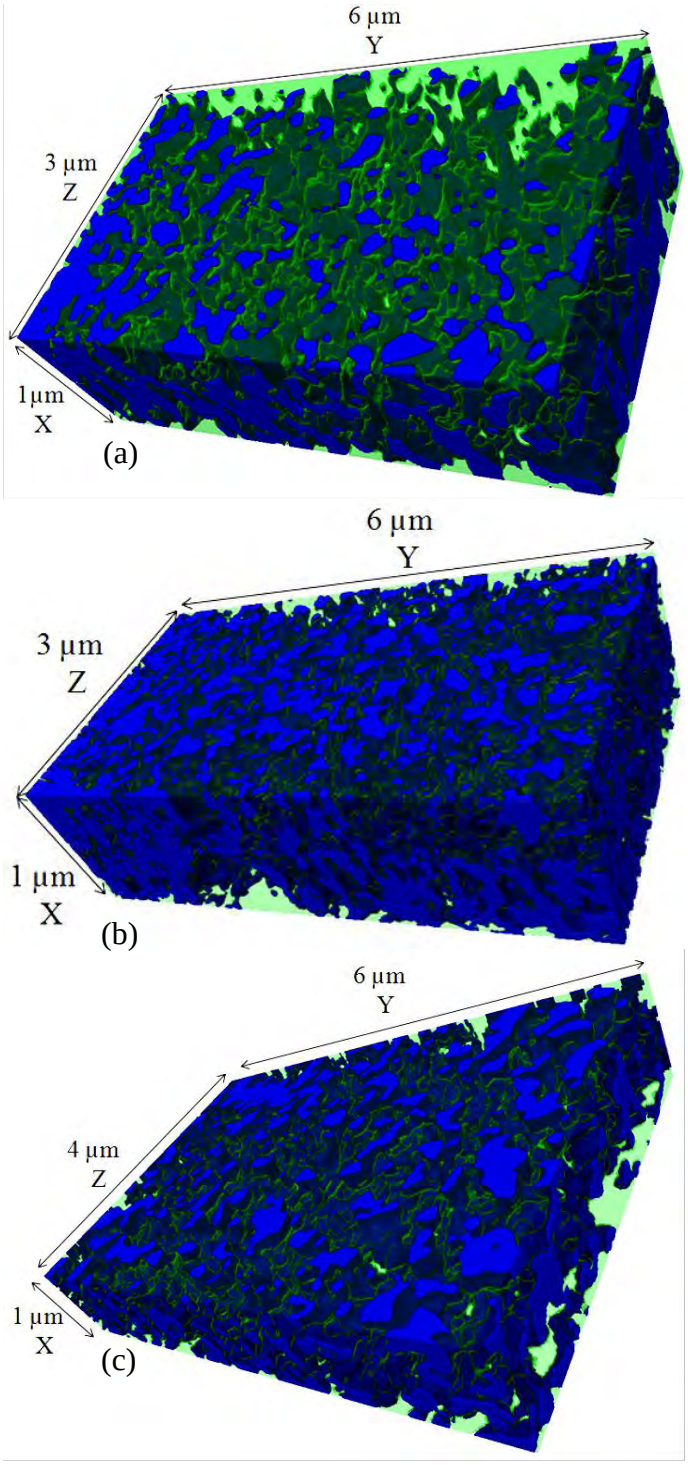

Figure 6.19. A 3D reconstruction of a different CL. Image have 5×5×10 nm (Z,Y,X) pixel size. The blue colour, transparent green represent the pore phase and the solid phase respectively; a) V4 anode; b)V4 cathode and; c)V5 cathode

In Table 6.1, although trends in porosity agree well, there is a poor agreement in the absolute amount. This could be due to the size of samples under investigations. The mercury porosimetry sample length scale is about 4 orders of magnitude larger than the length scale of the FIB/SEM nanotomography sample. Also, the mercury access to open pores and surface pores while the FIB/SEM nanotomography method provide information about all closed, blind and open pores. Since the very top surface of the CL is coated by a Pt protective layer, these pores are closed and subsequently removed from the pore analysis.

The pore sizes are not expected to be similar since mercury measures the pore "neck" while the pore "body" is measured by the FIB/SEM nanotomography. Therefore FIB/SEM nanotomography should always be bigger which is confirmed in Table 6.1.

Five MPL and CL samples were characterised through FIB/SEM nanotomography. In the next section the technique is applied to digitally reconstruct a micropipette tip.

6.6 3D RECONSTRUCTION OF A MICROPIPETTE TIP

Glass micro pipettes have been widely used for patch clamping. Although many researchers agree that the shape and roundness of the pipette tip are important for cell grabbing and gigaseal formation, no numerical values of the geometry have been reported so far. In this section, FIB/SEM nanotomography is used to obtain the 3D shape of a pipette tip.

6.6.1 Patch clamp and giga-seal

Patch clamp recording is an electrophysiology technique allowing study of ion channels of cells. It is a refinement of the voltage clamp method [231]. It has important applications in cell study and is a valuable tool to pharmaceutical research. In patch clamping, a glass pipette with a tip diameter of a few microns is pressed against a cell membrane to form a high resistance seal between the inside and outside of the pipette nozzle, known as gigaseal. It is found that achieving a gigaseal is dependent on the tip geometry of the internal wall of the pipette [232].

6.6.2 Experimental

A micro pipette with a tip diameter of 1.3 µm was coated with ~10 nm of gold and placed facing the electron beam. Figure 6.20 shows the schematic of the pipette, electron beam and ion beam configuration. The angle between I-beam and E-beam is 52^{o} degrees. Therefore, the angle between the imaging plane and the sample is 38^{o}. This information is used later for reconstruction.

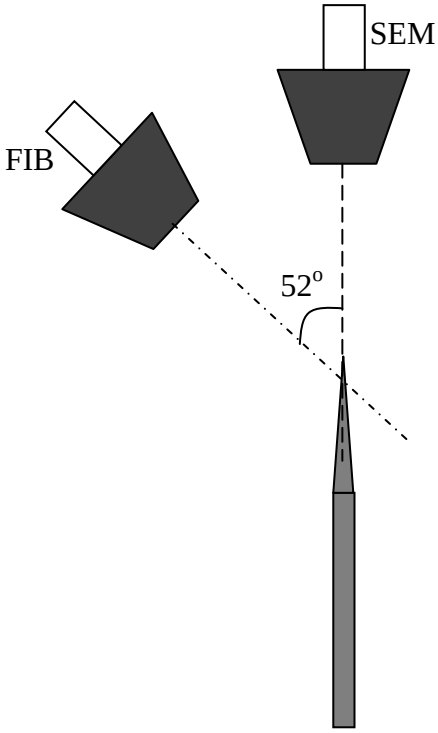

Figure 6.20. A schematic of pipette, SEM and FIB configuration

Each slice of the sample was milled off using Ga^+ ion beam at 30 kV and 100 pA for 90 seconds with an overlap parameter of 50%. 60 slices with a total thickness of 3 µm were removed and SEM images of the slices taken. The pixel size of the SEM images was 4.5 nm. Figure 6.21 shows an image of the 20th slice after milling and its internal edge.

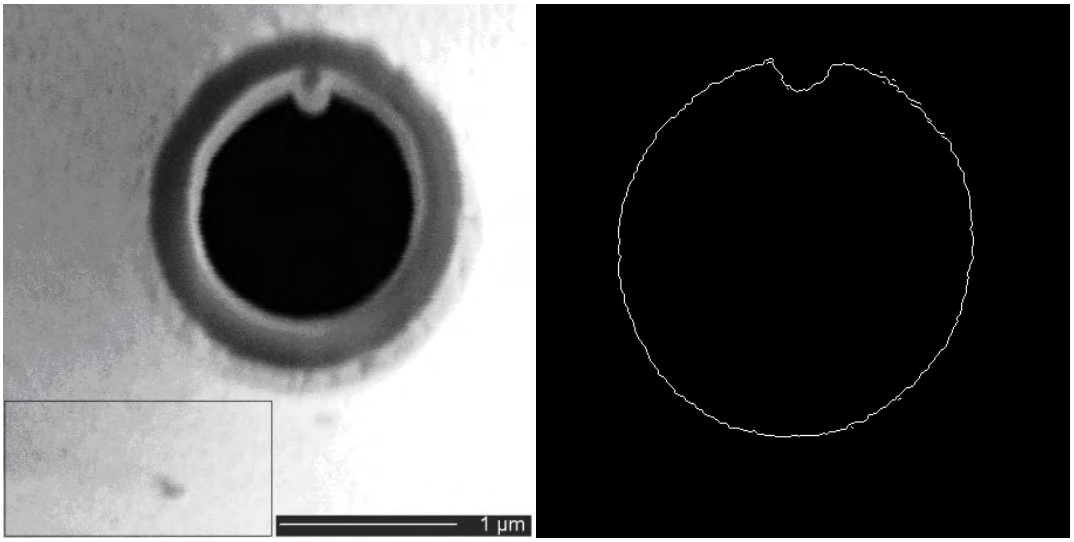

(a) (b)

Figure 6.21. An SEM image of a pipette after milling, the area inside the rectangle was used for image alignment; b) The edge of the internal circle of the pipette detected using Canny algorithm [144].

6.6.3 Image alignment

Feature based alignment method as described in section 6.2 was employed. A fixed feature which has not been milled during slicing and not affected by the ion beam is the bottom side of the pipette in Figure 6.21a which corresponds to the rectangle in Figure 6.21a. This part of the pipette in the images was used to align all of the images.

6.6.4 Edge detection

The edge of the internal circle of the pipette was detected using the Canny algorithm [233]. The basic idea of this algorithm is to detect at the zero-crossing of the second derivative of the smoothed images. It seeks out the zero-crossings of:

$$\frac{\partial^2(M \times I)}{\partial n^2} = \frac{\partial(\frac{\partial M}{\partial n} \times I)}{\partial n} \tag{6.8}$$

Where *M* and *I* are image matrix and unit matrix respectively and *n* is the direction of the gradient of the smoothed image. This is done using MATLAB for all of the slices.

6.6.5 Projection

As far as the image plane has a 38^o angle with respect to the sample slices as shown in Figure 6.20 one can calculate the position of each point of the sample slice. Assuming that *x* (horizontal) and *y* (vertical) axes are in the image plane and *z* is the norm of the surface, then:

$$x_{ssp} = x \tag{6.9}$$
$$y_{ssp} = \frac{y}{\cos(38)}$$

where indices "*ssp*" is the sample slice position. For z_{ssp}, the thickness of the slices are 50 nm so the relative distance between the slices remains 50 nm (equivalent to 11 pixels) and the initial angle of the image plane and projected plane is 38^o.

Figure 6.22a shows the 3D structure of the pipette tip reconstructed using MATLAB. The units of X, Y, Z axes are in pixel and each pixel is 4.5 nm. Figure 6.22b is the Y-Z plane view of the reconstructed image.

In order to examine the shape of pipette the tip, a perfect circle was fitted to each slice based on the least squared fitted circle method [234] and maximum deviation of the pipette shape from the circle was obtained. Figure 6.23 shows the first slice image and fitted circle. The maximum deviation from fitted circle was 43 nm. The average of maximum deviations of all slices was found as 67 nm.

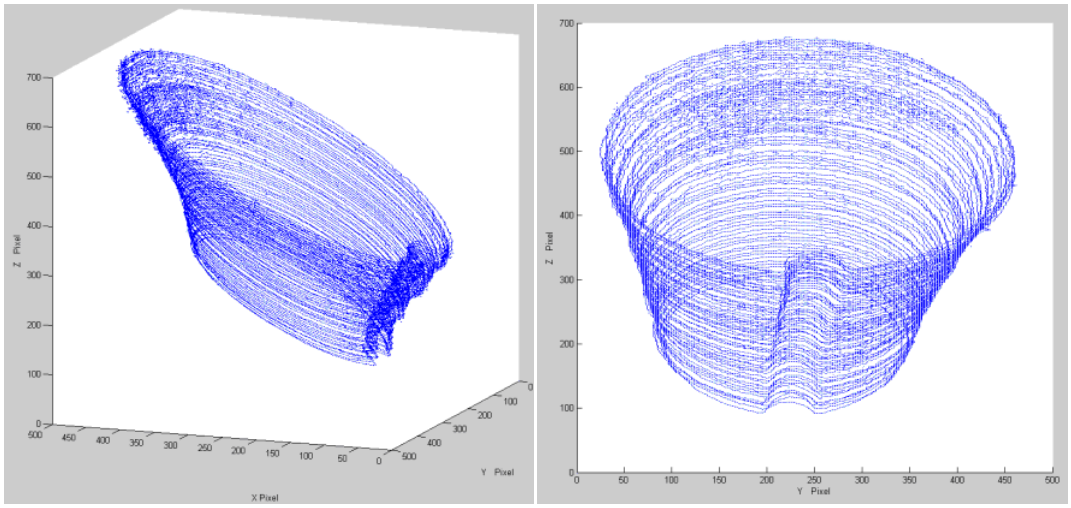

(a) (b)

Figure 6.22. A 3D structure of the pipette tip after reconstruction; b) The reconstructed sample in the Y-Z plane.

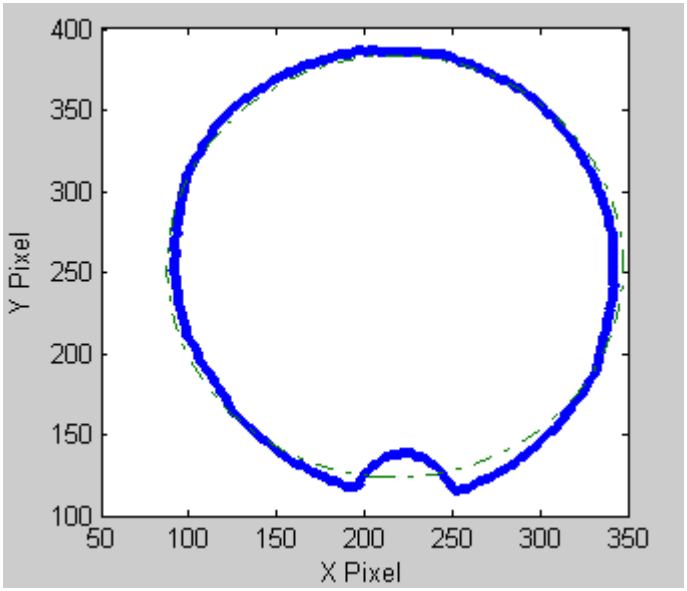

Figure 6.23. An image of the first slice and fitted circle. The fitted circle is shown in a dashed line [144].

6.7 SUMMARY

This chapter presents a FIB/SEM nanotomography approach to characterise the MPL and CL. Sample preparation steps including Pt layer deposition, fiducial mark milling and polishing-imaging were discussed. Key parameters were determined by analytical approaches and LB numerical modelling for both MPL and CL samples. In addition, FEA analysis was carried out for a throughout 2D cross-section of CL for calculation of effective diffusivity. Next, a number of the CL samples were characterised by FIB/SEM nanotomography and the results were compared to those obtained by mercury porosimetry. The technique then was extended to reconstruct a tip of a micropipette to reveal the roundness of the tip.

It has been successfully demonstrated that key structural data of the fuel cell MPL can be generated using the 3D model with 8×8×16 nm voxel size. The effective diffusivity, absolute permeability, tortuousity and characteristic capillary radii have also been obtained from directly-measured data from the 3D model. The LB numerical solver was subsequently applied to simulate the permeability of the MPL. The simulated permeability of the MPL suggested that the Kozeny constant for the MPL is generally one order of magnitude less than that expected for GDL materials. The LB numerical solver was also applied to visualise the tortuousity of the flow paths through the MPL. Also the average off-principal tortuousity was 7% larger than that obtained from centroid tracking analysis and therefore both are in good agreement. The FIB/SEM nanotomography was then applied for CL characterisation.

Similarly, the research demonstrates that FIB/SEM nanotomography can be employed to reveal the internal nanoscale structural features of a CL with 5×5×10 nm voxel size. The 3D LB numerical flow simulator was applied to the tomographic image in order to

determine key material characteristics including tortuousity and permeability. The centroid tracking tortuousity was again in good agreement with that of obtained by LB simulation. 2D FEA was used to reveal the streamline tortuousity for a throughout cross section of a 3 µm thick CL. Results were used to determine the effective diffusivity of the CL sample. Another 3 CL samples were characterised through FIB/SEM nanotomography and mercury porosimetry. The average pore size and porosity were compared. Although trends in porosity agree well, there is a poor agreement in the absolute amount. The pore sizes are not expected to be similar since mercury measures the pore "neck" while the pore "body" is measured by the FIB/SEM nanotomography. Therefore the FIB/SEM nanotomography should always be bigger. This was confirmed by the results.

The current research therefore demonstrates a step change in the ability to understand how porous materials behave as permeable systems, when in-situ measurement and visualisation in 3D is a formidable task. The method was then extended to digitally reconstruct a micropipette tip.

A 3 µm long section of a pipette with the tip diameter of 1.3 µm has been examined and 60 images with 4.5 nm pixel size were taken. The internal walls of the pipette tip, where the contact between the pipette and a cell occurs, were detected using the Canny algorithm. After 3D reconstruction of the micropipette tip in MATLAB, the roundness of each slice with least square fitted circle method was examined. The average of maximum deviation of all slices were found as 67 nm, or 10% in roundness error.

This is the final characterisation Chapter of this work. In the next Chapter, this thesis is summarised.

7 CHAPTER 7: CONCLUSIONS AND FUTURE WORK

7.1 INTRODUCTION

This PhD thesis is aimed at prediction of fluid flow by developing novel micro/nano 3D characterisation of PEFC porous layers and to meet the particular need of PEFC efficiency improvement. The research has involved X-ray μCT/nCT characterisation of the GDL and FIB/SEM nanotomography of the MPL & CL. In addition to the 3D reconstruction of various layers, the key micro/nano transport parameters including effective diffusivity, permeability and tortuousity were obtained through a coupled image-simulation approach. Furthermore methods have been successfully employed to characterise other materials.

The significant contribution of PEFC layer's 3D reconstruction research can be summarised as follows.

A. X-ray μCT/nCT image binarisation for characterisation of GDL

Morphological parameters of a 3D binary image of a woven and non-woven GDL reconstructed using X-ray μCT/nCT, have been obtained, and the influence of small alterations in the threshold value on the simulated flow properties of the reconstructed GDL has been determined. A range of threshold values on the greyscale map have been applied and the gas permeability of the binary images has been calculated using a single-phase LB model. In addition, the porosity, pore size distribution, mean pore radius and degree of anisotropy have been calculated directly from segmented voxel representation. References including fibre diameter, fibrils continuity and porosity greatly assisted in finely tuning the threshold for the 3D binary representative image.

B. X-ray µCT/nCT characterisation of uncompressed and compressed GDL

Detailed characterisation of a number of uncompressed GDL samples was given. For this purpose six nonwoven and woven GDLs were reconstructed through X-ray µCT/nCT with different resolutions. Based on the 3D model the porous material key micro/nanostructural information including, porosity, pore size distribution, average fibre size, average pore size, centroid tracking tortuousity, degree of anisotropy, effective diffusivity and permeability are obtained. Permeability was measured through an air permeability tester for all samples and compared to the permeability obtained from an analytical approach and LB simulation.

Characterisation of compressed woven GDL samples was also presented. It has been demonstrated that the image processing technique developed for the current work can capture the 3D compressed microstructure of a woven GDL over the range of 0 – 100 MPa. The sample is immersed with PDMS and pressed under compression to capture its compressed fibre structure.

C. FIB milling characterisation of materials through SEM stereo imaging

Using stereo pair images made it possible to reconstruct the FIB milled area and calculate directly the removed volume and sputtering yield of materials. A big challenge in the measurement is the optimization of the tilting angle which can be easily tuned by comparing a specified feature height with that of reconstruction.

D. FIB/SEM nanotomography of MPL & CL

It has been demonstrated that key structural data can be generated using the 3D model including porosity, average pore size and pore size distribution. The effective diffusivity, absolute permeability, tortuousity and characteristic capillary radii have also been obtained

from directly-measured data from the 3D model. The LB numerical solver was subsequently applied to simulate the permeability of the MPL and CL samples. The LB numerical solver was also applied to visualise the tortuousity of the flow paths through the MPL and CL. Two dimensional FEA was used to reveal the streamline tortuousity for a full cross section of a 3 µm CL. Results were used to determine the effective diffusivity of the CL sample. Another 3 CL samples were characterised through FIB/SEM nanotomography and Mercury porosimetry. The average pore size and porosity were compared.

E. Extension of SEM stereo imaging and FIB/SEM nanotomography methods to other applications

The SEM stereo imaging was used to validate the results of conventional tactile measurements applied to 12 urinary catheters. A 3D SEM stereo imaging technique was used to reconstruct the surface features of different catheters to validate tactile measurement results.

In another experiment, the surface of a typical pipette tip with the diameter of ~1.5 µm was reconstructed and the surface roughness parameters were obtained.

Similarly the SEM stereo imaging technique was applied to characterise the surface of diatomaceous frustules. Reconstructed 3D images were used to quantitatively evaluate the specimen. Geometrical parameters including volume and area were obtained based on the 3D data.

Finally, a 3 µm long section of a pipette with the tip diameter of 1.3 µm has been examined through FIB/SEM nanotomography and 60 images with 4.5 nm pixel size were taken. The internal walls of the pipette tip, where the contact between the pipette and a cell occurs,

were detected. After 3D reconstruction of the micro pipette tip the roundness of each slice with the least square fitted circle method was examined and the average maximum deviation of all slices was determined.

Through repeated experiments and vigorous characterisation the project objectives have been met. The following conclusions can be drawn from the research.

- For tomography 3D images, parameters including porosity, pore surface area, pore size distribution, characteristic lengths, object size distribution, mean pore radius, degree of anisotropy and centroid of slices were successfully calculated. Effective diffusion coefficient, Knudsen diffusion, tortuousity and permeability were analytically calculated based on the parameters obtained from the 3D images. LB modelling to calculate permeability and tortuousity was explained as well.

- It has been proven that when a study is carried out using X-ray μCT/nCT data, the key structural parameters are affected by small variation in threshold. Having some easily measurable references including porosity, average fibre diameter and continuity in the material will greatly assist to finely tune the threshold for the 3D binary representative image.

- For compressed GDL characterisation, samples can be immersed with PDMS and pressed under compression to capture its compressed fibre structure. The results demonstrate that this has been successfully applied to a batch of carbon cloth GDL for five compression pressures representing the 0 – 100 MPa range.

- Stereo imaging was successfully applied for FIB milling characterisation of the MPL and CL. The results prove that the new approach is accurate for common metals and silicone. The validated method then was used to characterise the MPL and CL. The

removed volume (μm^3) per dose (nC) for MPL and CL samples is similar and is around $1\mu m^3$/nC.

- The principle of the research successfully demonstrates that FIB/SEM nanotomography can be employed to reveal the internal nano-scale structural features of a PEFC MPL & CL with sub-16 nm pixel size. In addition, the method was coupled with numerical simulations including LB and FEA. The current research therefore demonstrates a step-change in the ability to understand how porous materials behave as permeable systems when in-situ measurement and visualisation in 3D is a formidable task.

- Finally, the nanotomography and the stereo imaging techniques were successfully applied to other materials such as glass micropipette, various metals, silicon, urine catheters and diatomaceous frustules.

7.2 SUGGESTIONS FOR FUTURE WORK

This thesis represents comprehensive research efforts performed to explore 3D reconstruction of PEFC porous layers. As such, it should be viewed as a solid foundation for further work. Future research is needed either to expand more applications or to complete works initiated in this PhD project which have not been completed because they are well beyond the project scope.

The following is a list of research topics.

- The above FIB/SEM nanotomography discussion was only concentrated on the MPL and CL before electrical tests. The next step could be to investigate the durability and degradation of the layer during fuel cell operation and to examine how key structural and transportation properties change.

- In terms of CL characterisation, Pt particles are generally around 1-3 nm which means their 3D visualisation requires higher resolution characterisation such as TEM tomography or electron tomography.

- In terms of numerical simulation, the LB method is computationally expensive. This suggests some image simplification is required. For instance one can only use the largest interconnected throughout pore of the sample for LB analysis. This would reduce the computation time.

- The LB analysis was only developed for single phase simulation. However, real case is multiphase multi component transport within various layers of PEFC. This requires extensive characterisation such as hydrophobicity characterisation.

- Determination of hydrophobicity in the samples is needed to determine the water transport. This could be done by X-ray nCT for GDL samples and FIB/SEM nanotomography combined with elemental mapping analysis.

REFERENCES

[1] Mathias, M. F., Roth, J., Fleming, F. & Lehnert, W., Handbook of Fuel Cells-Fundamentals, Technology and Application, Volume 3, Edited by Vielstich, W., Lamm A., and Gasteiger, H. A., John Wiley and Sons, Chichester, England, 2003.

[2] Zhong, C-J., Luo, J., Fang, B., Wanjala, B. N., Njoki, P. N., Loukrakpam R. and Yin, J., Nanostructured catalysts in fuel cells, Nanotechnology, 21, 1-20, 2010.

[3] Barbir, F., PEM Fuel Cells: Theory and Practice, Elsevier Academic Press, 2005.

[4] Mehta, V. & Cooper, J. S., Review and analysis of PEM fuel cell design and manufacturing, Journal of Power Sources, 114, 32-53, 2002.

[5] Tawfik, H., Hung, Y. & Mahajan, D., Metal bipolar plates for PEM fuel cell-A review, Journal of Power Sources, 163, 755-767, 2007.

[6] Davies, D. P., Adcock, P. L., Turpin, M. & Rowen, S. J., Bipolar plate materials for solid polymer fuel cells, Journal of Applied Electrochemistry, 30, 101-105, 2000.

[7] Du, L. & Jana, S. C., Highly conductive epoxy/graphite composites for bipolar plates in proton exchange membrane fuel cells, Journal of Power Sources, 172, 734-741, 2007.

[8] Lia, S. H., Weng, C. C., Yen, C. Y., Hsio, M. C., Ma, C. C. M., Tsai, M. C., Su, A., Yen, M., Y., Lin, Y. F. & Liu, P. L., Preparation and properties of functionalized multiwall carbon nanotubes/polypropylene nanocomposite bipolar plates for polymer electrolyte membrane fuel cells, Journal of Power Sources, 195, 263-270, 2010.

[9] Schulze, M., Schneider, A. & Gulzow, E., Alteration of the distribution of the platinum catalyst in membrane-electrode assemblies during PEFC operation, Journal of Power Sources. 127, 213-221, 2004.

[10] Benziger, J., Nehlsen J., Blackwell D., Brennan T. & Itescu J., Water flow in the gas diffusion layer of PEM fuel cells, Journal of Membrane Science, 261, 95-106, 2005.

[11] Ji, C. & Fly G. W., Increasing the hydrophilicity of carbon fibre paper by electropolymerization. US Patent No - 7250189.

[12] Weber, A. Z. & Newman, J., Effects of micro porous layers in polymer electrolyte fuel cells, Journal of the Electrochemical Society, 152, 677-688, 2005.

[13] Ostadi, H., Rama, P., Liu, Y., Chen, R., Zhang, X. X. & Jiang, K. J., 3D reconstruction of a gas diffusion layer and a micro porous layer, Journal of Membrane Science, 351, 69-74, 2010.

[14] Xie, J., More, K. L., Zawodzinski, T. A. & Smith, W. H., Porosimetry of MEAs made by ‘‘Thin Film Decal’’ Method and its Effect on Performance of PEFCs, Journal of the Electrochemical Society, 151, 1841-1846, 2004.

[15] Uchida, M., Aoyama, Y., Eda, N., & Ohta, A., Investigation of the microstructure in the catalyst layer and effects of both perfluorosulfonate ionomer and PTFE-loaded carbon on the catalyst layer of polymer electrolyte fuel cells, Journal of the Electrochemical Society, 142, 4143-4149, 1995.

[16] Paganin, V. A., Ticianelli E. A. & Gonzales E. R., Development and electrochemical studies of gas diffusion electrodes or polymer electrolyte fuel cells, Journal of Applied Electrochemistry, 26, 297-304, 1996.

[17] Ralph, T. R. & Hogarth, M. P., Catalysis for low temperature fuel cells, Part I: the cathode challenges, Platinum Metals Review, 46, 3-14, 2002.

[18] Uribe, F., Zawodzinski, T., Valerio, J., Bender, G., Garzon, F., Saab, A., Rockward, T., Adcock, P., Xie, J. & Smith,W., Fuel cell electrode optimization for operation on reformate and air, in Proc. 2002 Fuel Cells Lab R&D Meeting, DOE Fuel Cells for Transportation Program, 2002.

[19] Qi, Z. & Kaufman, A., Low Pt loading high performance cathodes for PEM fuel cells, Journal of Power Sources, 113, 37-43, 2003.

[20] Sasikumar, G., Ihm, J. W. & Ryu, H., Dependence of optimum Nafion content in catalyst layer on platinum loading, Journal of Power Sources, 132, 11-17, 2004.

[21] Kerres, J. A., Development of ionomer membranes for fuel cells, Journal of Membrane Science, 15, 3-27, 2001.

[22] Dupuis, A. N., Proton exchange membranes for fuel cells operated at medium temperatures: Materials and Experimental Techniques, 58, 289-327, 2011.

[23] Reichman, S., Duvdevani, T., Aharon, A., Philosoph, M., Golodnitsky, D. & Peled, E., A novel PTFE-based proton-conductive membrane, Journal of Power Source, 153, 228-233, 2006.

[24] Pereira, F., Valle, K., Belleville, P., Morin, A., Lambert, S. & Sanchez, C., Advanced mesostructure hybrid silica-nafion membranes for high-performance PEM fuel cell, Chemistry of Materials, 20, 1710-1718, 2008.

[25] Weber, A. Z. & Newman, J., Modelling transport in polymer electrolyte fuel cell, Chemical Review, 104, 4679-4726, 2004.

[26] Wang, C. Y., Fundamental models for fuel cell engineering, Chemical Review, 104, 4727-4766, 2004.

[27] Young, J., B., Thermofluid modelling of fuel cells, Annual Review of Fluid Mechanics, 39, 193-215, 2007.

[28] De la Rue, R. E. & Tobias, C. W., On the conductivity of dispersions, 106, 827-833, 1959.

[29] Li, G., Pickup, P. G., Ionic conductivity of PEMFC electrodes, 150, C745-C-752, 2003.

[30] Welty, J. R., Wicks, C. E., Wilson & R. E., Rorrer, G. L., Fundamentals of momentum, heat, and mass transfer, John Wiley & Sons, 5th edition, USA, 398-432, 2007.

[31] Chi, P. H., Chan, S. H., Weng, F. B., Su, A., Sui, P. C. & Djilali, N., On the effects of non-uniform property distribution due to compression in the gas diffusion layer of PEMFC, 35, 2936-2948, 2010.

[32] Tomadakis, M. & Robertson, T., Viscous permeability of random fibre structures: comparison of electrical and diffusional estimates with experimental and analytical results , Journal of Composite Materials, 39, 163-188, 2005.

[33] Gostick, J., Fowler, M., Pritzker, M., Ioannidis, M. & Behra, L., In-plane and through-plane gas permeability of carbon fibre electrode backing layers Journal of Power Sources, 162, 228-238, 2006.

[34] Nam, J. H. & Kaviany, M., Effective diffusivity and water-saturation distribution in single and two-layer PEMFC diffusion medium, International Journal of Heat and Mass Transfer, 46, 4595-4611, 2003.

[35] Shi, Y., Wu, H., Quan S., Xia, J., & Pan, M., Fractal model for predicting the effective binary oxygen f the gas diffusion layer in proton exchange membrane fuel cells, 195, 4865-4870, 2010.

[36] Thiedmann, R., Hartnig, C., Manke, I., Schmidt, V., & Lehnert, W., Local structural characteristics of pore space in GDL of PEM fuel cells based on geometric 3D graphs, Journal of the Electrochemical Society, B1339-B1347, 2009.

[37] Bird. R. B., Stewart, W. E., & Lightfoot, E. N., Transport phenomena, 2nd edition, John Wiley & sons, USA, 2002.

[38] Kong, C. S., Kim, D. Y., Lee, H. K., Shul, Y. G. & Lee, T. H. Influence of pore-size distribution of diffusion layer on mass-transport problems of proton exchange membrane fuel cells, 108,185-191, 2002.

[39] Berning, T., Djilali, N. , A 3D, multiphase, multi component model of the mathode and mnode of a PEM Fuel Cell, Journal of the Electrochemical Society, 150, A1589-A1598, 2003.

[40] Lee, W. K., Shimpalee, S. & Van Zee, J. W., Verifying predictions of water and current distributions in a serpentine flow field polymer electrolyte membrane fuel cell, Journal of the Electrochemical Society, 150, A341-A348, 2003.

[41] Chu, H. S., Yeh, C., Chen, F., Effects of porosity change of gas diffusion on performance of proton exchange membrane fuel cell, 123, 1-9, 2003.

[42] Gurau, V., Barbir, F. & Liu, H., An analytical solution of half-cell model for PEM fuel cell, Journal of the Electrochemical Society, 147, 2468-2477, 2000.

[43] Costamagna, P., Transport phenomena in polymeric membrane fuel cells, Chemical Engineering Science, 56, 323-332, 2001.

[44] He, W. S., Yi, J. S. & Van Nguyen, T., Two phase flow model of the cathode of PEM fuel cells using interdigitated flow fields, AICHE Journal, 46, 2053-2064, 2000.

[45] Rowe, A. & Li, X. G., Mathematical modelling of proton exchange membrane fuel cells, 102, 82-96, 2001.

[46] Pisani, L., Murgia, G., Valentini M. & D'Aguanno, B., A new semi-empirical approach to performance curve of polymer electrolyte fuel cells, 108, 192-203, 2002.

[47] Dutta, S., Shimpalee, S. & Van Zee, J. W. Numerical prediction of mass-exchange between cathode and anode channels in a PEM fuel cell, International Journal of Heat and Mass Transfer, 44, 2029-2042, 2007

[48] Lee, W. K., Shimpalee, S. & Van Zee, J. W., Verifying predictions of water and current distribution in a serpentine flow field polymer electrolyte membrane fuel cell, Journal of the Electrochemical Society, 150, A341-A348, 2003.

[49] Bear, J., Dynamics of fluids in porous media, Dover publications, USA, 1988.

[50] Tomadakis, M. M. & Sotirchos, S. V., Ordinary and transition regime diffusion in random fibre structures, AICHE Journal, 39, 397-412, 1993.

[51] Weber, A. Z., Darling, R. M., & Newman, J., Modelling two-phase behaviour in PEFCs, Journal of the Electrochemical Society, 151, A1715-A1727, 2004.

[52] Natarajan, D. & Van Nguyen, T., A two-dimensional, two phase, multi component, transient model for the cathode of a proton exchange membrane fuel cell using conventional gas distributors, 148, A1324-A1335, 2001.

[53] Pisani, L, Murgia, G. & Valentini, M., A working model of polymer electrolyte fuel cells- comparisons between theory and experiments, 149, A898-A904, 2002.

[54] Mukherjee, P. P., Kang, Q. & Wang, C. Y., Pore-scale modelling of two-phase transport in polymer electrolyte fuel cells-progress and perspective, Energy & Environmental Science, 4, 346-369, 2011.

[55] Tryggvason, G., Bunner, B., Esmaeeli, A., Juric. D., Al-Rawahi, N., Tauber, W., Han. J., Nas, S. & Jan, Y. J., Journal of Computational Physics, 162, 708-759, 2001.

[56] Hirt, C. W. & Nichols, B. D., Volume of fluid method for the dynamics of free boundaries, 39, 201-225, 1981.

[57] Fatt, I., The network model of porous media .1. capillary pressure characteristics, Transaction of the American institute of mining and metallurgical engineers, 207, 144-159, 1956.

[58] Fatt, I., The network model of porous media .2. dynamic properties of a single size tube network, 207, 160-163, 1956.

[59] Fatt, I., The network model of porous media .3. dynamic properties of networks with tube radius distribution, 207, 164-181, 1956.

[60] Sahimi, M., Comment on fractal and superdiffusive transport and hydrodynamic dispersion in heterogeneous porous-media-reply, Transport in Porous Media, 21, 189-194, 1995.

[61] Blunt, M. J., Flow in porous media-pore-network models and multiphase flow, Current Opinion in Colloid & Interface Science, 197-207, 2001.

[62] Gostick, J. T., Ioannidis, M. A., Fowler, M. W. & Pritzker J., Pore network modelling of fibrous gas diffusion layers for polymer electrolyte membrane fuel cells, Journal of Power Sources, 173, 277-290, 2007.

[63] Sinha, P. K. & Wang, C. Y., Pore-network modelling of liquid water transport in gas diffusion layer of a polymer electrolyte fuel cell, Electrochimica Acta, 52, 7936-7945, 2007.

[64] Sinha, P. K. & Wang, C. Y., Liquid water transport in a mixed wet gas diffusion layer of a polymer electrolyte fuel cell, Chemical Engineering Science, 63, 1081-1091, 2008.

[65] Koido, T., Furusawa, T. & Moriyama, K., An approach to modelling two phase transport in the gas diffusion layer of a proton exchange membrane fuel cell, Journal of Power sources, 175, 127-136, 2008.

[66] Bazylak, A., Berenjnov, V., Markicevic, B., Sinton, D., Djilali, N., Numerical and microfluidic pore networks: towards design for directed water transport in GDL, Electrochimica Acta, 53, 7630-7637, 2008.

[67] Lee, K. J., Nam, J. H. & Kim, C. J., Steady saturation distribution in hydrophobic gas diffusion layers of polymer electrolyte membrane fuel cells: a pore-network study, Journal of Power Sources, 195, 130-141, 2010.

[68] Hilpert, M. & Miller, C. T., Pore-morphology-based simulation of drainage in totally wetting porous media, Advances in Water Resources, 24, 243-255, 2001.

[69] Schulz, V. P., Becker, J., Wiegmann, A., Mukherjee, P. & Wang, C. Y., Modelling of two-phase behaviour in the gas diffusion medium of PEFCs via full morphology approach, Journal of the Electrochemical Society, 154, B419-B426, 2007.

[70] Becker, J., Schulz, V., P., Wiegmann, A., Numerical determination of two phase material parameters of a gas diffusion layer using tomography images, Journal of Fuel Science and Technology, 5, 021006, 2008.

[71] Chen, H., Chen, S. & Matthaeus W. H., Recovery of the Navier-Stokes equations using a lattice-gas Boltzmann method. Physical Review A, 45, R533-R5342, 1992.

[72] He, X. & Luo, L., A priori derivation of the lattice Boltzmann equation. Physical Review E, 55, 6333-6336, 1997.

[73] McNamara, G. R. & Zanetti, G., Use of the Boltzmann Equation to Simulate Lattice-Gas Automata. Physical Review Letters, 61, 2332-2335, 1988.

[74] Frisch, U., Hasslacher, B. & Pomeau, Y., Lattice-gas automata for the Navier – Stokes equation, Physical Review Letters,56, 1505-1508, 1986.

[75] Zhang, X., Crawford, J. W., Bengough A. G. & Young, I. M. On boundary conditions in the lattice Boltzmann model for advection and anisotropic dispersion equation. Advances in Water Resources, 25,601-609, 2002.

[76] Hao, L. & Cheng, P., Lattice Boltzmann simulation of anisotropic permeabilities in carbon paper gas diffusion layers, Journal of Power Sources, 186, 104-114, 2009.

[77] Van Doorrnaal, M. A., Pharoah, J. G., Determination of permeability in fibrous media using the Lattice Boltzmann method with application to PEM fuel cells, 59, 75-89, 2009.

[78] Kim, S. H. & Pitsch, H., Reconstruction and effective transport properties of the catalyst layer in PEM fuel cells, Journal of the Electrochemistry Society, 156, B673-B681, 2009.

[79] Mukherjee, P. P., Wang, C. Y. & Kang, Q. J., Mesoscopic modelling of two-phase and flooding phenomena in polymer electrolyte fuel cells, Electrochimica Acta, 54, 6861-6875, 2009.

[80] Mekherjee, P. P., Cold start of polymer electrolyte fuel cells: three-stage startup characterization, Electrochimica Acta, 55, 2636-2644, 2010.

[81] Ostadi, H., Rama, P., Liu, Y., Chen, R.., Zhang, X. and Jiang, K., Nanotomography based study of gas diffusion layers, Microelectronic Engineering, 87 (5-8), 1640-1642, 2010.

[82] P. Rama, Y. Liu, R. Chen, H. Ostadi, K. Jiang, Gao Y, XX. Zhang, Determination of anisotropic permeability of a carbon cloth GDL, International Journal for Numerical Methods in Fluids (In press).

[83] P. Rama, Y. Liu, R. Chen, H. Ostadi, K. Jiang, Gao Y, XX. Zhang, R. Fisher, M. Jeschke, Simulation of liquid water breakthrough in a nano-tomography reconstruction of a carbon paper gas diffusion layer, AIChE Journal (In press).

[84] P. Rama, Y. Liu, R. Chen, H. Ostadi, K. Jiang, Gao Y, XX. Zhang, D. Bivio, P. Grassini, A numerical study of structural change and anisotropic permeability in compressed carbon cloth polymer electrolyte fuel cell gas diffusion layers, Fuel Cells (In press).

[85] P. Rama, Y. Liu, R. Chen, H. Ostadi, K. Jiang, X. X. Zhang, Multi-Scale Modelling of Single-Phase Multi-Component Transport in the Cathode Gas Diffusion Layer of a Polymer Electrolyte Fuel Cell, ACS Energy & Fuels 24, 3130-3143, 2010.

[86] P. Rama, Y. Liu, R. Chen, H. Ostadi, K. Jiang, X. Zhang, R. Fisher, M. Jeschke, An X-ray tomography based Lattice Boltzmann simulation study on gas diffusion layers of

polymer electrolyte fuel cells, ASME Journal of Fuel Cell Science and Technology, 7(3), 031015, 1-12, 2010.

[87] Mukherjee, P. P. & Wang, C. Y., Stochastic microstructure reconstruction and direct numerical simulation of PEFC catalyst layer, Journal of the Electrochemical Society, 153, A840-A849, 2006.

[88] He, W., Ma, Z. W., Young, T., Teo, W. E. & Ramakrishna, S., Fabrication of collagen-coated biodegradable polymer nanofibre mesh and its potential for endothelial cells growth, Biomaterials, 26, 7606-7615, 2005.

[89] Boland, E. D., Telemeco, T. A., Simpson, D. G., Wnek, G. E. & Bowlin, G. L., Utilizing acid pretreatment and electrospinning to improve biocompatibility of poly (glycolic acid) for tissue engineering, Journal of Biomedical Materials Research Part B: Applied Biomaterials, 71B, 144-152, 2004.

[90] H. Ostadi, P. Rama, Y. Liu, R. Chen, X. Zhang, K. Jiang, Threshold fine-tuning and 3D characterisation of porous media using X-ray nanotomography, Current Nanosciences, 6, 226-231, 2010.

[91] Jena, A. K. & Gupta, K. M., Characterization of pore structure of fuel cell components containing hydrophobic and hydrophilic pores, 41st Power Sources Conference, 2004.

[92] Jena, A. K. & Gupta, K. M., In-plane compression porometry of battery separators, Journal of Power Sources, 80, 46-52, 1999.

[93] Volfkovich, Y. M., Sosenkin, V. E. & Bagotsky, V. S., Structural and wetting properties of fuel cell components, Journal of Power Sources, 195, 5429-5441, 2010.

[94] Volfkovich, Y. M., Sosenkin, V. E. & Nikolskaya, N. F., Porous structure of the catalyst layers of electrodes in a proton-exchange membrane fuel cell: a stage-by-stage study, Russian Journal of Electrochemistry, 46, 336-344, 2010.

[95] Divisek, J., Eikerling, M., Mazin, V., Schmitz, H., Stimming, U. and Volfkovich, Y. M., A study of capillary porous structure and sorption properties of Nafion proton-exchange membranes swollen in water, Journal of the Electrochemical Society, 145, 2677-2683, 2010.

[96] Volfkovich, Y. M. & Bagotzky, V. S., the method of standard porosimetry 1. principles and possibilities, Journal of Power Sources, 48, 327-338, 1994.

[97] Xie, Z., Zhao, X. S., Adachi, M., Shi, Z. Q., Mashio, T., Ohma, A., Shinohara, K., Holdcroft, S. & Navessin, T., Fuel cell cathode catalyst layer from "gree" catalyst links, Energy & Environmental Science, 35, 184-193, 2008.

[98] Park, H. S., Cho Y. H., Cho, Y. H., Jung, C. R., Jang, J. H. & Sung, Y. E., Performance enhancement of PEFC through temperature control in catalyst layer fabrication, Electrochimica Acta, 53, 763-767, 2007.

[99] Park, H. S., Cho, Y. H., Cho Y., H., Park, I. S., Jung, N., Ahn, M. & Sung, Y., Modified decal method and its related study of microporous layer in PEM fuel cells, Journal of the Electrochemical Society, 155, B455-B460, 2008.

[100] Park, S. & Popov, B. N., Effect of cathode GDL characteristics on mass transport in PEM fuel cells, Fuel, 88, 2068-2073, 2009.

[101] Park, S, Lee, J. W. & Popov, B. N., Effects of carbon loading in microporous layer of PEM fuel cell performance, Journal of Power Sources, 163, 357-363, 2006.

[102] Dubinin, M. M. & Plavnik,G. M., Microporous structure of carbonaceous adsorbents, Carbon, 6, 183-192,1968.

[103] Gregg, S. J., & Sing, K. S. W., Adsorption, Surface Area and Porosity, Academic Press, USA, 1967.

[104] Sharma, S. & Siginer, D. A, Permeability measurement methods in porous media of fibre reinforced composites, Applied Mechanics Reviews, 63,020802,2010.

[105] Ranade, A., D'Souza, N. A., Wallace, R. M. & Gnade, B. E., High sensitivity gas permeability measurement system for thin plastic films, Review of Scientific Instruments, 76, 013902, 2005.

[106] Hamamoto, S., Moldrup, P., Kawamoto, K., Komatsu & T., Rolston, D. E., Unified measurement system for gas diffusion coefficient, air permeability, and gas diffusion coefficient in variably saturated soil, Soil Science Society of America, 73, 1921-1930, 2009.

[107] Toyoshima K., Hino, T., Hirohata, Y., Yamauchi, Y. & Hinoki, T., Crack propagation analysis of SiC_f/SiC composites by gas permeability measurement, Journal of European Ceramic Society, 31, 1141-1144, 2011.

[108] Caston, T. B., Murphy A. R. & Harris, T. A. L., Effect of tightness and structure on the in-plane and through-plane permeability of woven carbon fibres for gas diffusion layers, 196, 709-716, 2011.

[109] Pozio, A., Cemmi, A., Carewska, M., Paoletti, C. & Zaza, F., Characterisation of gas diffusion electrodes for polymer electrolyte fuel cells, Journal of Fuel Cell Science and Technology, 7, 041003, 2010.

[110] Chun, J. H., Park, K. T., Lee, J. Y., Kim, S. G., Lee, E. S., Jyoung, J. Y. & Kim, S. H., Determination of pore size distribution of microporous layer in PEMFC using pore forming agents under various drying conditions, International Journal of Hydrogen Energy, 35, 11148-11153, 2009.

[111] Le Page, J. F., Applied heterogeneous catalysis: design, manufacture, use of solid catalysts, Editions Technip, Paris, France, 1987.

[112] Brunauer, S., Emmett, P. H., Teller, E., Adsorption of gases in multimolecular layers, Journal of the American Chemical Society, 60, 309-319, 1938.

[113] Cindrella L., Kannan, A. M., Lin, J. F., Saminathan, K., Ho, Y., Lin, C. W., Wertz, J., Gas diffusion layer for proton exchange membrane fuel cells - A review, Journal of Power Sources, 194, 146-160, 2009.

[114] Tang, J. M., Itkis, M. E., Wang, C., Yan, Y. & Haddon, R. C., Carbon nanotube free-standing membrane as gas diffusion layer in hydrogen fuel cells, Micro & Nano letters, 1, 62-65, 2006.

[115] Uchida, M., Fukuoka, Y., Sugawara, Y., Eda, N. & Ohta, A., Effects of microstructure of carbon in the catalyst layer on the performance of polymer-electrolyte fuel cells, Journal of the Electrochemical Society, 143, 2245-2252, 1996.

[116] Soboleva, T., Zhao, X. S., Mallek, K., Xie, Z., Navessin, T. & Holdcroft, S., On micro-, meso- and macroporous structures of polymer electrolyte membrane fuel cell catalyst layer, ACS Applied Materials & Interfaces, 2, 375-384, 2010.

[117] Adcock, P. A., Pacheco, S. V., Norman, K. M. & Uribe, F. A., Transition metal oxides as reconfigured fuel cell catalysts for improved CO tolerance: Polarization data, Journal of the electrochemical Society, 152, A459-A466, 2005.

[118] Reimer, L., Scanning electron microscopy physics of image formation and microanalysis, Springer-Verlag, Berlin, 1984.

[119] Erni, R., M. D., Rossel, Kisielowski, C. & Dahmen, U., Atomic-resolution imaging with a sub-50-pm electron probe, Physical Review Letters, 102, 096101, 2009.

[120] Fuller, T., Fuller, C., Harting, C., Ramani, V., Uchida, H., Gasteiger, H. A., Cleghom S., Strasser, P., Zawodzinski, T., Jones, D., Shirvanian, P., Jarvi, T., Zelenay, P., Lamy, C., Bele, P. & Harting, C.,Proton exchange membrane fuel cells 9, ECS transactions 25, 2009.

[121] Cheng, X., Chen, L., Peng, C., Zhiwu, C., Zhang, Y. and Fan, Q., Catalyst microstructure examination of PEMFC membrane electrode assemblies vs. time, Journal of the Electrochemical Society, 151, A48-A52, 2004.

[122] Thiedmann, R., Fleischer, F., Harting, C., Lehnert, W., Schmidt, V., Stochastic 3D modelling of the GDL structure in PEMFCs based on thin section detection, Journal of the Electrochemical Society, 155, B391-B399, 2008.

[123] Tang, H., Wang, S., Pan, M. & Yuan, R., Porosity-graded micro-porous layers for polymer electrolyte membrane fuel cells, Journal of Power Sources, 166, 41-46, 2007.

[124] Kong, C. S., Kim, D. Y., Lee, H. K., Shul, Y. G. and Lee, T. H., Influence of pore size distribution of diffusion layer on mass-transport problems of proton exchange membrane fuel cells, Journal of Power Sources, 108, 185-191, 2002.

[125] Pasaogullari U., Mukherjee, P. P., Wang, C. Y. and Chen, K. S., Anisotropic heat and water transport in PEFC cathode gas diffusion layer, Journal of the Electrochemical Society, 154, B823-B834, 2007.

[126] H. Ostadi, K. Jiang, P. D. Prewett, Micro/Nano X-ray tomography reconstruction fine-tuning using scanning electron microscope images, Micro & Nano Letters, V3, No.4, pp.106-109,2008.

[127] Herman, G. T., Image reconstruction from projections, the fundamentals of computerised tomography, Academic press, New York, 1980.

[128] Midgley, P. A., Ward, E. P. W., Hungria, A. B. & Thomas, J. M., Nanotomography in chemical, biological and material sciences, Chemical Society Reviews, 36, 1477-1494, 2007.

[129] Acton, P., D. & Kung, H., F., Small animal imaging with high resolution single photon emission tomography, Nuclear Medicine and Biology, 30, 889-895, 2003.

[130] Mamin, H., J., Poggio, M., Degen, C., L. & Rugar, D., Nuclear magnetic resonance imaging with 90-nm resolution, Nature Nanotechnology, 2, 301-306, 2007.

[131] Kuznetsova, Y., Neumann, A. & Brueck, S. R., Imaging interferometric microscopy-approaching the linear systems limits of optical resolution, Optics Express, 15, 6651-6663, 2007.

[132] Izzo, J., R., Joshi, A., S., Grew, K. N., Chiu, W., K., S., Tkachuk, A., Wang, S., H. & Yun, W. Nondestructive reconstruction and analysis of SOFC anodes using X-ray computed tomography at sub-50 nm resolution, Journal of the Electrochemical Society,155, 504-508, 2008.

[133] Shearing, P., R., Gelb, J., Yi, J., Lee, W., K., Drakopolous., M. & Brandon., N., P. Analysis of triple phase contact in Ni-YSZ microstructures using non-destructive X-ray tomography with synchrotron radiation, Electrochemistry Communications, 12, 1021-1024, 2010.

[134] Uchida, H., Song, J., M., Suzuki, S., Nakazawa, E., Baba, N. & Watanabe, M. Electron tomography of nafion ionomer coated on Pt/Carbon black in high utilization electrode for PEFCs, The journal of Physical Chemistry B, 110, 13319-13321, 2006.

[135] Zhang, J., Physical Characterization of Electrocatalysts, PEM Fuel Cell Electrocatalysts and Catalyst Fundamentals and Applications, Springer-Verlag, London, 2008.

[136] Kubis, A. J., Shiflet, G. J., Dunn, D. N. & Hull R. Focused Ion-Beam tomography, Metallurgical and Materials Transactions A, 35A, 1935-1943, 2004.

[137] Mangan, M. A., Lauren, P.D. & Shiflet, G. J., Three-dimensional reconstruction of Widmanstatten plates in Fe-12.3Mn-0.8C, Journal of Microscopy, 188, 36-41, 1997.

[138] Wilson, J. R., Kobsiriphat, W., Mendoza, R., Chen, H. Y., Hiller, J. M., Miller, D. J., Thornton, K., Voorhees, P. W. & Adler, S. B., Three-dimensional reconstruction of a solid-oxide fuel-cell anode, Nature Materials, 5, 541-544, 2006

[139] Gostovic, D., Smith, J. R., Kundinger, D. P., Jones, K. S. & Wachsman, E. D., three-dimensional reconstruction of porous LSCF cathodes, Electrochemical and Solid-State Letters, 10, B214-B217, 2007.

[140] Zils, S., Timpel, M., Arlt, T., Wolz, A., Manke, I. & Roth, C., 3D visualisation of PEMFC electrode structures using FIB nanotomography, Fuel Cells, 10, 966-972, 2010.

[141] Ziegler, C., Thiele, S. & Zengerle, R., Direct three-dimensional reconstruction of a nanoporous catalyst layer for a polymer electrolyte fuel cell, Journal of Power Sources, 196, 2094-2097,2011.

[142] Sinha, P. K., Halleck, P. & Wang, C. Y., Quantification of liquid water saturation in PEM fuel cell diffusion medium using X-ray micro tomography, Electrochemical and Solid-State Letters, 9, A344-A348, 2006.

[143] Garzon, F. H., Lau, S. H., Davey, J. R. & Borup, R. L., Micro and nano X-ray tomography of PEM fuel cell membranes after transient operation ECS Transactions, Proton Exchange Membrane Fuel Cells 11, 1139-1150, 2007.

[144] H. Ostadi, M. Malboubi, K. Jiang, P.D. Prewett, 3D reconstruction of a micro pipette tip, Microelectronic Engineering, N86,868-870, 2009.

[145] Parkinson, C. R. & Sasov, A., High-resolution non-destructive 3D interrogation of dentin using X-ray nanotomography Dental Materials, 24, 773-777, 2008.

[146] Haddad W. S., McNulty, I., Trebes J. E., Anderson E. H., Levesque R. A. & Yang L., Ultrahigh-Resolution X-ray Tomography, Science, 266, 1213-1215,1994.

[147] SkyScan 1072 desktop X-ray microtomography user manual, 2008.

[148] SkyScan 2011 desktop X-ray nanotomography user manual, 2009.

[149] Leonard, A., Blacher, S., Marchot, P., Pirard, J. P. & Crine, M., Image analysis of X-ray microtomograms of soft materials during convective drying, Journal of Microscopy, 212, 197-204, 2003.

[150] Sasov, A., X-ray microtomography of plastics and composite materials, Developments in X-ray tomography III, proceedings of the Society of Photo Optical Instrumentation engineers (SPIE),4503,274-281,2002.

[151] Masschaele, B. C., Cnudde, V., Dierick, M., Jacobs, P., Van Hoorebeke, L. & Vlassenbroeck, J., UGCT, new X-ray radiography and tomography facility, Nuclear instruments & methods in physics research section A-accelerators spectrometers detectors and associated equipments, 580, 266-269, 2007.

[152] SkyScan 1172 desktop X-ray microtomography, 2005.

[153] Lorensen, W. E., Cline, H. E., Marching cubes: a high resolution 3D surface construction algorithm. Computer Graphics, 21, 163-169, 1987.

[154] Bouvier, D. J., Double time cubes: a fast surface construction algorithm for volume visualization, unpublished report, University of Arkansas, 313 Engineering Hall, Fayetteville, AR 72701, USA, 2000.

[155] SkyScan CT-Analyser, CTAN user manual, version 1.6.1, 2006.

[156] Manke, I., Hartnig, C., Grunerbel, M., Lehnert, W., Kardjilov, N., Haibel, A., Hilger A. & Banahrt, J. Investigation of water evolution and transport in fuel cells with high resolution synchrotron x-ray radiography, Applied Physics Letters, 90, 4501-4505, 2007.

[157] Feser, J. P., Prasad, A. K. & Advani, S. G., Experimental characterization of in-plane permeability of gas diffusion layers, Journal of Power Sources. 162, 1226-1231, 2006.

[158] Hung, T. F., Huang, J., Chuang, H. J., Bai, S. H., Lai, Y. J. & Chen-Yang, Y. W., Highly efficient single-layer gas diffusion layers for the proton exchange membrane fuel cell, Journal of Power Sources,184,165-171, 2008.

[159] Otsu, N., A threshold selection method from grey-level histograms, IEEE transaction on systems, man, and cybernetics, 9, 62-66,1979.

[160] Sezgin, M. & Sankur, B., Survey over image thresholding techniques and quantitative performance evaluation, Journal of Electronic Imaging, 132, 146-165,2004.

[161] Ulrich, D. & Van Rietbergen, B., Laib A., Rüegsegger P.,The ability of three-dimensional structural indices to reflect mechanical aspects of trabecular bone, Bone, 25, 55-60, 1999.

[162] Hildebrand T. & Ruegsegger P., A new method for the model independent assessment of thickness in three dimensional images, Journal of Microscopy,185,67-75,1997.

[163] Pisani, L., Valentini, M., Murgia, G., Analytical pore scale modelling of the reactive regions of polymer electrolyte fuel cells, Journal of the Electrochemical Society, 150, A1549-A1559, 2003.

[164] Odgaard A., Three-dimensional methods for quantification of cancellous bone architecture, Bone, 1997, 20(6), 315-328.

[165] Wang, C. T. & Smith, J. M. Tortuousity factors for diffusion in catalyst pellets. AICHE journal. 29, 132-136, 1983).

[166] Holzer, L., Indutnyi, F., Gasser, P. H., Munch, B. & Wegmann, M., Three-dimensional analysis of porous BaTiO3 ceramics using FIB nanotomography, Journal of Microscopy-Oxford, 216, 84-95, 2004.

[167] Holzer, L., Muench, B., Wegmann, M., Gasser, P. & Flatt, R. J., FIB-nanotomography of particulate system - Part I: Particle shape and topology of interfaces, Journal of the American Ceramic Society, 89, 2577-2585, 2006.

[168] M. Kaviany, Principles of heat transfer in porous media, second ed., Springer, New York, USA,1999.

[169] Fishman, Z. & Bazylak, A., Heterogeneous through-planbe distribution of tortuousity, effective diffusivity and permeability for PEMFC GDL, Journal of the Electrochemical Society, 158, B247-B252, 2011.

[170] Gostick, J. T., Fowler, M. W., Pritzker, M. D., Ioannidis M. A. & Behra, L. M., In-plane and through-plane gas permeability of carbon fibre electrode backing layers, Journal of Power Sources, 162,228-238, 2006.

[171] Rama, P., Liu, Y., Chen, R., Ostadi, H., Jiang, K., Zhang, X., Fisher, R. & Jeschke, M.,An X-ray tomography based Lattice Boltzmann simulation study on gas diffusion layers of polymer electrolyte fuel cells, ASME Journal of Fuel Cell Science and Technology, 7, 031015, 1-12, 2010.

[172] Ding, M., Odgaard, A. & Hvid, I., Accuracy of cancellous bone volume fraction measured by micro-CT scanning, Journal of Biomechanics,32, 323-326, 1999.

[173] Hara, T., Tanck, E., Homminga, J. & Huiskes, R., The influence of microcomputed tomography threshold variations on the assessment of structural and mechanical trabecular bone properties, Bone. 23, 163-169, 2002.

[174] Pfrang, A., Veyret, D., Sieker, F. & Tsodridis, G., X-ray computed tomography of gas diffusion layers of PEM fuel cells: Calculation of thermal conductivity, International Journal of Hydrogen Energy, 35, 3751-3757, 2010.

[175] Lee, W. K., Ho, C. H., Van Zee J. W. & Murthy, M. The effects of compression and gas diffusion layers on the performance of a PEM fuel cell. Journal of Power Sources, 84,45-51,1999.

[176] Ge, J., Higier, A. & Liu, H. Effect of gas diffusion layer compression on PEM fuel cell performance. Journal of Power Sources,159,922-927,2006.

[177] Lin, J. H., Chen, W. H., Su, Y. J. & Ko, T. H. Effect of gas diffusion layer compression on the performance in a proton exchange membrane fuel cell. Fuel, 87, 2420-2424, 2008.

[178] Lee, S. J., Hsu, C. D. & Huang, C. H, Analyses of the fuel cell stack assembly pressure, Journal of Power Sources,145,353-361,2005.

[179] Chi, P. H., Chan S. H., Weng, F. B., Su, A., Sui, P. C. & Djilali, N. On the effects of non-uniform property distribution due to compression in the gas diffusion layer of a PEMFC, International Journal of Hydrogen Energy, 2009, article in press, doi:10.1016/j.ijhydene.2009.05.066

[180] Zhou, P., Wu & C. W. Numerical study on the compression effect of gas diffusion layer on PEMFC performance. Journal of Power Sources,170, 93-100, 2007.

[181] Bazylak, A., Sinton, D., Liu, Z. S. & Djilali, N., Effect of compression on liquid water transport and microstructure of PEMFC gas diffusion layers. Journal of Power Sources,163,784-792,2007.

[182] Lotters, J. C., Olthuis, W., Veltink, P. H. & Bergveld, P., The mechanical properties of the rubber elastic polymer polydymethylsiloxane for sensor applications. Journal of Micromechanics and Microengineering, 7, 145-147 1997.

[183] Rama, P., Liu, Y., Chen, R., Ostadi, H., Jiang, K., Gao., Y., Zhang, XX., Bivio, D. & Grassini, P., A numerical study of structural change and anisotropic permeability in

compressed carbon cloth polymer electrolyte fuel cell gas diffusion layers, Fuel Cells, 11, 274-285, 2011.

[184] Yao, N., Focused Ion Beam Systems Basics and Applications, Cambridge University Press, Cambridge,2007, Chapters 2,4,5,10.

[185] Orloff, J., Swanson L. W., Utlaut, M., Fundamental limits to imaging resolution for focused ion beams, Journal of Vacuum Science and Technology B, 14, 3759-3763, 1996.

[186] Sigmund, P., Theory of sputtering. I. sputtering yield of amorphous and polycrystalline targets Phys. Rev. 184, 383-416, 1969.

[187] Nuver, T. T., Karssen, L. C., Rudolph, H., Zeijlmans van Emmichoven, P. A. & Niehaus, A., Preferential ejection of sputtered and reflected atoms in the keV bombardment of Cu(1 1 0) with noble gas ions, Nuclear instruments and methods in physics research section B: Beam interactions with materials and atoms, 179, 503-514, 2001.

[188] Miyagawa, Y., Nakadate, H., Djurabekova F., & Miyagawa, S., Dynamic-sasamal: simulation software for high-dose ion implantation, surface and coatings technology, 158, 87-93, 2002.

[189] Kempshall, B. W., Schwarz, S. M., Prenitzer, B. I., Giannuzzi, L. A., Irwin, R. B. & Stevie, F. A., Ion channelling effects on the focused ion beam milling of copper Journal of Vacuum Science and Technology B, 19, 749-754, 2001.

[190] Mulders, J. J. L., De Winter, D. A. M & Duinkerken, W. J. H. C. P., Measurement and calculations of FIB milling yield of bulk metals, Microelectronic Engineering, 84, 1540-1543, 2007.

[191] Bariani P., De Chiffre L., Hansen H. N. & Horsewell A., Investigation on the traceability of three dimensional scanning electron microscope measurements based on the stereo-pair technique, Precision Engineering, 29, 219-228, 2005.

[192] Samak D., Fischer A. & Rittel D., 3D Reconstruction and Visualization of Microstructure Surfaces from 2D Images, Journal of Manufacturing Technology, 56(1), 149-152, 2007.

[193] Ostadi H., Jiang K. & Prewett P.D., Characterization of FIB milling yield of metals by SEM stereo imaging technique, Microelectronic Engineering, 86, 1021-1024, 2009.

[194] MeX^{TM} software manual, Graz, Austria: Alicona Imaging GmbH, Version 5.0.1 EN 01, 2008.

[195] Marinello, F., Bariani, P., Savio, E., Horsewell, A. & De Chiffre, L., Critical factors in SEM 3D stereo microscopy, Measurement Science and Technology, 19, 1-12, 2008.

[196] See: www.srim.org

[197] xP dual beam^{TM} workstation online documentation, PN25421-A, 2000.

[198] Hukins, D.W.L., Preventing encrustation in indwelling urethral catheters. Medical Device Technology, 16, 25-27,2005.

[199] Feneley, R.C.L., Parkin, J., Scanlan, J. & Wooley, M., Developing alternative devices to the long-term urinary catheter for draining urine from the bladder. Proceedings of the Institution of Mechanical Engineers Part H: Journal of Engineering in Medicine 217, 297-303,2003

[200] Getliffe, K.A. & Mulhall A.B., The encrustation of indwelling urinary catheters. British Journal of Urology 67, 1991, 337-341.

[201] Cox A.J. & Hukins D.W.L., Morphology of mineral deposits on encrusted urinary catheters investigated by scanning electron microscopy. Journal of Urology 142, 1989, 1347-1350.

[202] Glahn B.E., Influence of drainage conditions on mucosal bladder damage by indwelling catheters. I Pressure study. Scandinavian Journal of Urology and Nephrology, 22, 1988, 87-92.

[203] Glahn B.E. , Braendstrup O., & Olesen H.P., Influence of drainage conditions on mucosal bladder damage by indwelling catheters. I Histological study. Scandinavian Journal of Urology and Nephrology, 22, 1988, 93-99.

[204] Thomas, T. R., Recent advances in the measurement and analysis of surface microgeometry, Wear, 33, 205-233, 1975.

[205] Poon C.Y. & Bhushan B., Comparison of surface roughness measurements by stylus profiler, AFM and non-contact optical profiler, Wear, 190,76-88, 1995.

[206] McGenough J. A., Micromachining of engineering materials, chapter 2, Measurement Techniques in Micromachining,15-50, 2002.

[207] Neher, E. & Sakmann, B., Single-channel currents recorded from membrane of denervated frog muscle-fibres, Nature, 260, 799-802,1976.

[208] Hamill, O. P., Marty, A., Neher, E., Sakmann, B., & Sigworth, F. J., Improved patch-clamp techniques for high-resolution current recording from cells and cell-free membrane patches, European Journal of Physiology, 391, 85-100, 1981.

[209] Li, S., Lin & L., A single cell electrophysiological analysis device with embedded electrode, Sensors and Actuators A, 134, 20-26, 2007.

[210] Kornreich, B. G., The patch clamp technique principles and technical considerations, Journal of Veterinary Cardiology, 9, 25-37, 2007.

[211] Stett, A., Burkhardt, C., Weber, U., Stiphout, P. & Knott, T., CYTOCENTERING: A novel technique enabling automated cell-by-cell patch clamping with the CYTOPATCHTM chip, Receptors and Channels, 9, 59-66, 2003.

[212] Lau, A. Y., Hung, P. J., Wu, A. R., & Lee, L. P., Open-access microfluidic patch-clamp array with raised lateral cell trapping sites, Lab on a chip, 6, 1510-1515, 2006.

[213] Ong, W. & Yobas, L., A missing factor in chip-based patch clamp assay: gigaseal, Journal of Physics: Conference Series,34, 187-191, 2006.

[214] Klemic, K. G., Klemic, J. F. & Sigworth, F. J., An air-moulding technique for fabricating PDMS planar patch-clamp Electrodes, European Journal of Physiology, 449, 564-572, 2005.

[215] Kusterer, J., Alekov, A., Pasquarelli, A., Müller, R., Ebert, W., Lehmann-Horn, F. & Kohn, E., A diamond-on-silicon patch-clamp-system, Diamond & Related Materials, 14, 2139-2142, 2005.

[216] Picollet-D'hahan, N., Sauter, F., Ricoul, F., Pudda, C., Marcel, F., Sordel, T., Chatelain, F. & Chartier, I., Multi-Patch: A chip-based ion-channel assay system for drug screening, The 2003 International Conference on MEMS, NANO and Smart Systems, IEEE.

[217] Malboubi, M., Ostadi, H., Wang, S., Gu, Y. & Jiang, K., Effects of pipette tip roughness on giga-seal formation, Engineering Letters, 17, 2009.

[218] Vrieling, E.G., Beelen, T.P.M., van Santen R. A., & Gieskes, W. W. C., Diatom silicon biomineralization as an inspirational source of new approaches to silica production, Journal of Biotechnology. 70, 39-51, 1999.

[219] Parker, A. R. & Townley, H. E., Biomimetics of photonic nanostructures, Nature Nanotechnology, 2, 347-353, 2007.

[220] Losic, D., Mitchell, J. G. & Voelcker, N. H., Diatomaceous lessons in nanotechnology and advanced materials, Advanced Materials, 21, 2947-2958, 2009.

[221] Butcher, K. S. A., Ferris, J. M., Phillips, M. R., Wintrebert-Fouquet, M., Wah, J. W. J., Jovanovic, N., Vyverman, W. & Chepurnov, V., A luminescence study of porous diatoms, Material Science and Engineering C, 25, 658-663, 2005.

[222] Hamm, C. E., Merkel, R., Springer, O., Jurkojc, P., Maier, C., Prechtel, K. & Smetacek, V., Architecture and material properties of diatom shells provide effective mechanical protection, Nature 421, 841-843, 2003.

[223] Losic, D., Rosengarten, G., Mitchell, J. G. & Voelcker, N. H., Pore architecture of diatom frustules: potential nanostructured membranes for molecular and particle separations, Journal of Nanoscience and Nanotechnology, 6, 982-989, 2005.

[224] Fuhrmann, T., Landwehr, S., Rharbi-Kucki, M. E. & Sumper, M., Diatoms as living photonic crystals, Applied Physics B, 78, 257-260, 2004.

[225] Rosi, N. L., Thaxton C. S. & Mirkin, C. A., Control of nanoparticle assembly by using DNA-modified diatom templates, Angewandte Chemie International Edition, 116, 5616-5619, 2004.

[226] Coradin, T. & Livage, J., Synthesis, characterization, and diffusion properties of biomimetic silica-coated gelatine beads, Material Science and Engineering C, 25, 201-205, 2005.

[227] X. Chen, H. Ostadi, K. Jiang, 3D surface reconstruction of diatomaceous frustules, Analytical Biochemistry, 403, 63-66, 2010.

[228] Ishitani, T. & Yaguchi, T., Cross-sectional sample preparation by focused ion beam: a review of ion-sample preparation, Microscopy Research and Technique, 35, 320-333, 1996.

[229] Lucas, B. D., Generalized image matching by the method of differences, PhD thesis, Department of Computer Science, Carnegie-Mellon University, 1984.

[230] Heijs, A. W. J. & Lowe, C. P., Numerical evaluation of the permeability and the kozeny constant for 2 types of porous-media, Physical Review, 51, 4346-4352, 1995.

[231] Kandel, E. R., Schwartz J., H. & Jessell T. M., Principles of Neural Science, 4th ed pp.152-155. McGraw-Hill, New York, 2000.

[232] Ongi, W. L., Yobas L., & Ong, W. Y., A Missing factor in chip-based patch clamp assay: gigaseal, Journal of Physics, 34, 187–191, 2006.

[233] Canny, J., A computational approach to edge detection, IEEE transaction on pattern analysis and machine intelligence, 8,679-714, 1986.

[234] Gander, W., Golub, G. H. & Strebel, R., Least-squares fitting of circles and ellipses, BIT Numerical Mathematics, 34 ,558-578 ,1994.